ELECTRON TRANSPORT IN MAGNETIC TUNNEL JUNCTIONS

A Dissertation
Presented to
The Academic Faculty

By

Jason F. Dark

In Partial Fulfillment
of the Requirements for the Degree
Doctor of Philosophy in the
School of Physics

Georgia Institute of Technology

May 2021

ELECTRON TRANSPORT IN MAGNETIC TUNNEL JUNCTIONS

Approved by:

Professor Dragomir Davidović, Advisor
School of Physics
Georgia Institute of Technology

Professor Martin Mourigal
School of Physics
Georgia Institute of Technology

Professor Zhigang Jiang
School of Physics
Georgia Institute of Technology

Professor John D. Cressler
School of Electrical and Computer Engineering
Georgia Institute of Technology

Dr. Thomas Zac Ward
Quantum Heterostructures Group
Oak Ridge National Laboratory

Date Approved: April 09, 2021

Thoroughly conscious ignorance is the prelude to every real advance in science.

James Clerk Maxwell

To my wife:

you are my best friend,

my love,

my partner in life;

I could not have made it this far without you.

- - - - - - - - - -

To my advisor:

the training I have received under your guidance

is and always will be

invaluable.

- - - - - - - - - -

Thank you both so very much!

ACKNOWLEDGMENTS

I would like to thank my advisor, Professor Dragomir Davidović, for his guidance and patience with me throughout this long journey. I would like to thank my committee members: Professor Davidović, Professor Mourigal, Professor Jiang Professor Cressler, and Dr. Thomas Zac Ward for agreeing to supervise my defense. I would additionally like to thank Prof. Mourigal, Prof. Cressler, and Dr. Thomas Zac Ward and their respective research groups for their help and collaboration in different aspects of this work. I am grateful for the funding support provided to me by the School of Physics (GTA support), U.S Department of Energy (under contract number DE-FG02-06ER46281 and contract number DE-SC0014664), ORNL Core Liaisons Partnership (GATech-ORNL SEED Grant) and Georgia Tech (graduate student support).

I am grateful for the lab training I received from Dr. Patrick Gartland, and the many discussions with Grant Nunn as we navigated through the use and care of the lab equipment that first year in the lab. I also learned a great deal from Drs. Dogukan Deniz, Jean-Phillipe Turmaud, and Yiran Hu. I would like to thank Hanbin(Victor) Ying for the many (enjoyable?) hours we worked together and the many discussions over the years regarding both research and life. I would like to thank Drs. Thomas Zac Ward, Yunyi Pai, Jason Lapano, Matthew Brahlek, Benjamin Lawrie, Jie Zhang, Amanda Huon, and Alessandro Mazza for their help, guidance and training while I was at Oak Ridge National Laboratory (ORNL). Also, thanks to the multiple scientists who helped train me in the ORNL Center for Nanophase Materials Science clean room. I would like to thank the past and current undergraduate students who have spent time in our lab for their work and helpful discussions: Sri Krishna(Chetan) Velivela, Daniel Monaghan, Robert(Drew) Welser, Piero Chiappina, Shobhan Kulshreshtha, and Donghyun(Kevin) Jin.

I am grateful for the support of many of my fellow cohorts who entered into the School of Physics with me those many years ago, especially in that first year gauntlet of classes.

That list could get pretty long and I am bound to forget someone, so I will shorten it to Conner Herndon, Mary-Rose Barrios, Marcus Daum, and Logan Kageorge. I would like to thank Drs. Edwin Greco, Martin Jarrio, Emily Alicea-Muños, and Prof. Schatz for their infectious excitement for teaching undergraduate students. Although TA work was many times an extra (necessary) burden, remembering the joy for teaching young minds physics really helped make the extra hours worth it. I would also like to thank Prof. Ballantyne for our career and graduate school status discussions and Prof. Jiang for our career discussion as well. I am thankful for the continual support of the School of Physics staff, many people ranging from IT support to purchasing and finance who all work to make our lives easier in the department. Also, the Georgia Tech EHS department for keeping us safe and healthy in the lab environment.

I would like to thank my family: my wife, Danielle Dark, for your endless support, my parents and siblings for your support and comic-relief in our outrageously large group text (7 people total, big families are fun), and M28 Church. I also would like to thank Prof. Rafael de la Madird for encouraging me to study physics and attend graduate school. I am sure there are many others I have forgotten, so if you are reading this, thank you as well.

TABLE OF CONTENTS

LIST OF TABLES

LIST OF FIGURES

SUMMARY

In this thesis, I lay the groundwork for studying low temperature magnetization dynamics of ferromagnetic nanoparticles using cryogenic preamplification. The motivation for this work comes from previous measurements by Jiang *et al.* where spin noise was used for real-time measurement of the magnetization dynamics of a ferromagnetic nanoparticle. I use a high resistance magnetic tunnel junction to model the nanoparticle double junctions and a silicon-germanium heterojunction bipolar transistor as a cryogenic preamplifier. Results of the experiment show an increase in the signal-to-noise ratio and bandwidth of the tunnel magnetoresistance signal produced by the magnetic tunnel junction. I will also discuss preliminary measurements of a double magnetic tunnel junction incorporating a permalloy nanomagnet with and without terbium-doping. Adding small amounts of terbium to permalloy thin films has been shown to increase the dynamical magnetic damping of the thin film. My results show a decrease in the zero bias anomaly in samples with terbium-doping compared to those without terbium-doping.

CHAPTER 1
INTRODUCTION

Through various forms of technological innovations, over the years, digital systems have increased in speed and decreased in size and power consumption. This provides a unique challenge for any magnetic-based memory associated with nearly all digital electronics today. Improved fabrication techniques have led to size reductions in individual magnetic elements[28], and the field of spin transfer torque has led to lower power consumption for the writing of information to magnetic elements[2]. The overall speed, on the other hand, is directly related to how quickly the particles, or nanomagnets, undergo magnetic reversal and stabilize in a different orientation[123]. Consequently, understanding the magnetization dynamics of a single nanomagnet is paramount for the future development of faster magnetic memory.

To begin studying the magnetization dynamics of nanomagnets, we need a way to monitor and record the magnetization direction of the nanomagnet under observation. Some directions taken in the past have used ferromagnetic thin films as the nanomagnet studied by microscopy [52], the magneto-optic kerr effect [8, 125], ferromagnetic resonance [98, 99] or tunnel magnetoresistance (TMR) in magnetic tunnel junctions (MTJs) [1, 25, 41, 55, 56, 120, 122] to measure the magnetization dynamics of the thin films. Other directions use nanoparticles as the nanomagnet and microSQUIDs [116, 117] to measure dynamics or spin-to-charge conversion in double junctions [48, 49] to measure the spin-noise and translate this noise to motion of the nanomagnet. Finally, in single molecule magnets, known as molecular magnets, SQUIDs have been used for magnetometry [34, 35, 93, 106].

In this thesis, I lay the ground work for studying low temperature magnetization dynamics of ferromagnetic nanoparticles using TMR. The motivation for this study comes from previous measurements by Jiang *et al.* where spin noise was used for real-time measure-

ment of the magnetization dynamics of a ferromagnetic nanoparticle [48, 49]. I use a high resistance MTJ to model the nanoparticle double junctions and cryogenic preamplification to increase the signal-to-noise ratio (SNR) and bandwidth of the TMR measurement. I will also discuss preliminary measurements of a double magnetic tunnel junction (DMTJ) incorporating a permalloy nanomagnet with and without terbium-doping to study the effects of increased dynamical magnetic coupling to the environment using electron transport.

Most solid state physics and/or condensed matter courses only include a brief overview of semiconductor physics. With that in mind, I use the next section (Section 1.1) in this chapter to explain the necessary concepts in electronic band theory and semiconductor physics to understand the operation of bipolar junction transistors (the type I use for cryogenic preamplification). In Section 1.2, I give a brief over view of micromagnetics theory. Section 1.3 describes a basic tunnel junction which naturally leads to the MTJ and double MTJ. Finally, Section 1.4 explains the need for cryogenic preamplification.

Chapter 2 covers the general fabrication process used in our lab including the necessary changes needed to produce the samples used in this thesis. Chapter 3 focuses on a cryogenic study of silicon-germanium heterojunction bipolar transistors, the type of tranistor technology I use for cryogenic preamplification. Chapter 4 shows the improvements gained using cryogenic preamplification to measure a TMR signal from a high resistance MTJ at low temperatures. Chapter 5 gives preliminary results from low temperature electron transport measurements of a DMTJ incorporating a permalloy nanomagnet with and without terbium-doping. Chapter 6 gives a conclusion of the work and possible future directions of research.

1.1 Overview of Semiconductor Physics

This section is intended to give the reader the necessary conceptual understanding of bipolar junction transistors starting from electronic band theory.

1.1.1 Formation of Electronic Energy Bands

To understand the applicable physics of semiconductors, we must first discuss the formation of electronic bands. Electronic bands are inherently caused by overlapping of electron wave functions [102]. Solving the Schrödinger Equation for a hydrogen atom gives a discrete spectrum of energy values, or levels, for an electron bound to a positively charge nucleus (ie. a single proton for the most common isotope of hydrogen). The same model applies to other elements although exact calculations become more and more computationally intensive as the number of particles within the atom increases.

Within an atom, only a set number of electrons have each specific value of energy, or occupy each energy level. The Pauli exclusion principle describes this effect and more generally states that no two fermions within a system can occupy the same quantum state. Electrons, being fermions, follow this rule, so each energy level will only contain a set number of different quantum states described by the solution to the Schrödinger Equation. Electrons with lower energies occupy lower energy shells that are closer, spatially, to the nucleus. Increasing the energy of a bound electron moves it to a further reaching shell with larger energy, more weakly bound to the nucleus, and, spatially, further from the nucleus. Due to the Pauli exclusion principle and the discrete energy levels in an atom, elements with many electrons contain a subset of electrons that exist further from the nucleus.

If we bring two atoms near each other, as the distance of separation decreases, the furthest bound electrons (highest energy) of each atom begin to interact with each other. This process leads to overlapping of the electron wave functions, or quantum states, of each atom. The interacting quantum states of each atom form a set of new, complex states with different energies than their original energy levels. If we add more and more atoms closely spaced, the originally discrete, allowable energy levels form into a continuous band of allowable energies.[1] Given the proper circumstances (ie. temperature and atomic con-

[1] Actually, until the number of atoms reaches infinity, the energy spectrum is not truly continuous; however, with a large number of atoms, the energy gaps within the energy band become so small we can treat the spectrum as continuous.

figuration), the new energy states formed from the overlapping electrons may lead to a reduction in the total energy of the system, making the bonding of atoms more favorable than the atoms existing separately.

The bonding of many atoms together leads to stable solid structures. These structures can be classified as amorphous, crystalline, or polycrystalline [86]. The classifications correspond to the physical distribution of the constituent atoms within the solid. Specifically, atoms in crystalline solids arrange into periodic arrays in three dimensions. Polycrystalline structures have similar periodic arrays of atoms but a single array cannot describe the entire material. Instead, the arrays are disjointed throughout space forming multiple connected crystalline pieces. Amorphous solids do not have any consistent long range periodic ordering, so the atoms are still bound together, but they do not form into nice, three dimensional arrays.

Continuous bands of electron energies are not the only important part in the electron energy spectrum of solids. The band gaps that separate each continuous group of electron energies play a vital role in the physics of semiconductors and solids in general. Band gaps are regions in the electron energy spectrum in which no electron states exist. These gaps in the allowable electron energies are a result of electron interactions with ionic cores throughout the solid [53]. The Kronig-Penney model [58] brilliantly shows the formation of electron energy bands and band gaps by simulating an electron moving through a one-dimensional periodic potential. Making use of Bloch's theorem, specfically, that periodic potentials in the Schrödinger Equation will have the same periodicity in the solution [10], Kronig and Penney paved the way for deriving the physics of crystalline solids from a quantum mechanical point of view. The "Bloch wave" solutions to the Schrödinger Equation introduced a new way to view electrons moving through a crystal, where the electron could be modeled by a free electron with an effective mass dependent on the dispersion of the energy bands (electron energy versus the wave number) instead of accounting for the large number of separate ionic cores throughout the crystal. In reality, the informa-

tion about the ionic cores remains encoded in the energy band diagram, and, as a result, in the effective mass of the electrons, but the model greatly simplifies further analysis. For real systems, especially those in three dimensions, calculating the band structure quickly becomes computationally intensive.

The discrete energy spectrum of each atom and the periodic spacing of the crystal both play vital roles in the formation of the electronic band structure of a solid; however, there does exist a caveat for amorphous solids. Although there is no long range periodic ordering in amorphous solids, they still have band structures. This goes beyond the scope of this thesis. (Reference [17] gives a review for the interested reader.)

1.1.2 Metals, Semiconductors, and Insulators

After developing the concept of electronic band structures in solids, we must know how electrons actually fill these bands. Due to the Pauli exclusion principle, at 0 K, the electrons fill the available energy levels, starting from the lowest, with one electron per allowable energy state. When no magnetic field is present, the spin degeneracy of the electrons allows for two electrons to occupy each apparent energy level. The factor of two accounts for the up and down spin-states of each electron that, in the presence of a magnetic field, leads to an additional splitting of each energy level. Without a magnetic field, both quantum states will have the same energy filling with two electrons.

Depending on the structure of the material, the highest energy electrons at 0 K, after filling all available lower energy states, exist either inside a band or at the very top of a band. This energy is known as the Fermi energy of the material (not to be confused with the Fermi level [3]). In simple cases where there is no band overlap, meaning there is a measurable band gap between the lowest energy and highest energy of each consecutive upper and lower band, respectively, we categorize materials in the following way. When the Fermi energy lies within a band, but not at the top, this band is only partially filled with electrons. We call this band the conduction band, and this material a metal. When the

Fermi energy lies at the top of a band, the band is completely filled. We call this filled band the valence band, and the next higher energy band, above the band gap, the conduction band. If the band gap of the material is larger than 4 eV, we, generally, call the material an insulator, or specifically, a band insulator. If the band gap is smaller than 4 eV, we, generally, call the material a semiconductor [100].

At temperatures above absolute zero, the energies of electrons in a solid follow the Fermi-Dirac distribution [83]. Simply put, the distribution describes the ratio of filled to total available states at some energy [85], or the probability that an electron exists at some energy level. The Fermi function is the probability density function of the distribution:

$$f(E) = \frac{1}{e^{(E-\mu)/kT} + 1}, \tag{1.1}$$

where E is the energy of the state, μ is the chemical potential, or Fermi level, of the material, k is the Boltzmann constant, and T is the temperature. The Fermi level is the energy at which the probability for an electron to occupy a state at that energy is 50%. For metals, this energy is approximately equal to the Fermi energy, but for intrinsic semiconductors (not doped with impurities) and insulators, this energy is usually close to the mid-gap region. Because of this distribution, and more specifically its dependence on temperature, thermal energy excites electrons in a material to energy levels higher than its Fermi energy when $T > 0\ K$. This means that at room temperature (and lower/higher temperatures) both semiconductors and insulators may have electrons excited across the band gap to the conduction band. Due to the difference in the size of the band gap, thermal excitation causes semiconductors to have more electrons in the conduction band than an insulator at a given temperature, but both types of materials will have less electrons in the conduction band than that of a metal.

Conductivity, σ, describes the amount of electrical current generated in a material with

respect to an applied electric field, $\vec{E}$, such that

$$\vec{J} = \sigma \vec{E}, \tag{1.2}$$

where $\vec{J}$ is the current density per unit area in the direction of the current flow. If we apply an electric field to a metal, electrons within the conduction band easily move to higher energy states in the conduction band. This increase in energy of the electrons causes them to have a net momentum in the opposite direction of the applied electric field, producing a net flow of charge, electrical current, in the direction of the electric field. Consequently, metals will have a large conductivity. The same is true for semiconductors and insulators above absolute zero; however, due to the smaller number of electrons in the conduction band, and, the same small number of empty states left behind in the valence band, semiconductors will have a lower conductivity than metals, and insulators will have a lower conductivity than semiconductors.

When electrons are thermally excited across the band gap, they leave behind empty states in the valence band. For simplification, since there are far more filled states in the valence band than empty states, we treat the empty states as positively charged quasi-particles called holes. An applied electric field also causes a hole current to flow in the semiconductor valence band (similar to electrons in the conduction band), where positively charged holes move down into the valence band gaining momentum in the direction of the applied field. We account for this extra charge transport by defining the conductivity as:

$$\sigma = q(\mu_p p + \mu_n n), \tag{1.3}$$

where q is the elementary charge, $\mu_p(\mu_e)$ is the hole(electron) mobility, and $p(n)$ is the hole(electron) carrier concentration. The carrier concentration is the number of charge carriers (holes in the valence band or electrons in the conduction band) per unit volume in

a material, and the mobilities describe how easily[2] each type of charge carrier moves (or drifts) through the material with an applied electric field.

1.1.3 Doping Semiconductors

We can add either electrons or holes to semiconductors by strategically inputting specific impurities into a semiconductor. Donor atoms add additional electrons to the material while acceptor atoms add holes. The impurities are chosen so that the number of valence electrons per atom are more (donors) or less (acceptors) than that of the semiconductor being doped. The impurities replace semiconductor atoms in the crystal lattice without significantly modifying the lattice itself (ie. the number of impurities in relation to total atoms is kept low and impurity atoms are generally chosen to be of similar size to those being replaced). Donor atoms create impurity states within the band gap near the conduction band filled with electrons at 0 K. As temperature increases, thermal energy ionizes more and more donor atoms exciting their electrons into the conduction band. The excited electrons increase the electron carrier concentration of the now doped semiconductor. A similar process occurs with acceptor atoms, but these create empty states within the band gap near the valence band edge. Additionally, when acceptor atoms are ionized by thermal energy, the empty states become filled with electrons from the valence band increasing the number of holes in the valence band, and, subsequently, the hole carrier concentration of the material. The binding energy of the electrons(holes) to the dopant ion is much lower than the band gap of the material. For reference, in silicon the band gap is 1.12 eV, but the ionization energy of a common donor dopant, phosphorus, is only 44 meV, and for a common acceptor dopant, boron, only 46 meV, so at room temperature most of the dopants will be ionized [94].

After adding and ionizing dopants, the overall material remains electrically neutral. The

[2]The "ease" of motion manifests as carriers moving with some average drift velocity when applying an electric field. The higher the mobility of a specific charge carrier in a material, the higher the average drift velocity for that carrier in the material at the same applied electric field.

act of replacing a lattice atom with one that has more(less) valence electrons leads to an extra electron(hole) in the vicinity of the dopant ion. The charge of the electron(hole) is thus canceled by that of the dopant ion leading to an overall electrically neutral material. Written as a mathematical formula, charge neutrality becomes

$$p - n + N_D^+ - N_A^- = 0, \tag{1.4}$$

where $p(n)$ is the hole(electron) carrier density, N_D^+ is the ionized donor concentration, and N_A^- is the ionized acceptor concentration.

The intrinsic carrier concentration of a material takes the value of the electron and hole carrier concentrations when these two values are equal during equilibrium conditions:

$$\begin{aligned} if \quad & n_0 = p_0, \\ then \quad & n_i = n_0 = p_0, \end{aligned}$$

where $n_0(p_0)$ are the electron(hole) carrier concentrations at equilibrium conditions, and n_i is the intrinsic carrier concentration. The intrinsic carrier concentration depends on the effective masses of the charge carriers in a material, the shape of its conduction and valence bands, and temperature as well. The law of mass action governs the total number of charge carriers in a material [15] leading to:

$$n_i^2 = np, \tag{1.5}$$

so increasing either carrier concentration by doping leads to a decrease in the other carrier concentration. Semiconductors with more holes than electrons are considered p-type, while those with more electrons than holes are n-type. Doping a semiconductor also shifts the Fermi level of the material towards the impurity states of the semiconductor. (See references [85, 86] for more information.)

The temperature range where ionized dopants exceed that of the intrinsic carrier density defines the extrinsic region of the semiconductor, while the temperature regions both above and below this temperature range define the intrinsic region. The intrinsic region at temperatures below the extrinsic region exists due to charge carrier freeze-out. With decreasing temperature, less thermal energy means less electrons(holes) excite into the conduction(valence) and less impurities become ionized. Conversely, increasing the temperature increases the intrinsic carrier concentration, while the total ionized dopant concentration remains constant (once all of the dopants have been ionized).

In situations where doping is very large (about $> 10^{18}$ cm^{-3} in silicon [94]), the semiconductor begins to act more like an impure metal as opposed to a semiconductor [70]. Additionally, the large number of impurities begin interacting with each other forming an impurity band of states leading to a reduction in the band gap of the material as well [32]. In short, the physics of degenerately doped semiconductors (as they are called) can have significant differences from their non-degenerately doped counterparts including different temperature dependence. Refer to the cited references above as well as [69, 85, 86] for more information.

The following equations describe the charge carrier transport in semiconductor materials [85, 86]. The current equations,

$$\vec{J_n} = q\left(\mu_n n\vec{E} + D_n\vec{\nabla}\left(n\right)\right) \tag{1.6}$$

$$\vec{J_p} = q\left(\mu_p p\vec{E} - D_p\vec{\nabla}\left(p\right)\right), \tag{1.7}$$

where $J_{n,p}$ are the electron and hole current densities and $D_{n,p}$ are the electron and hole diffusion coefficients, give the contributions to current caused by both drift (motion caused by an electric field) and diffusion (motion caused by thermal energy that equalizes particle concentrations throughout the material). The change in sign for the hole diffusion term accounts for the positive holes diffusing in the direction of a negative gradient (ie. to

regions of less holes) which still causes a positive current. Gauss's Law from electricity and magnetism,

$$\epsilon\vec{\nabla}\cdot\vec{E} = p - n + N_D^+ - N_A^-, \tag{1.8}$$

where ϵ is the electrical permittivity of the material, describes the electric field produced from a net charge density existing in a material (ie. in the depletion region of a PN junction in Section 1.1.4). The continuity equations,

$$\frac{dn}{dt} = \frac{1}{q}\vec{\nabla}\cdot\vec{J_n} - r_n + g_n \tag{1.9}$$

$$\frac{dp}{dt} = -\frac{1}{q}\vec{\nabla}\cdot\vec{J_p} - r_p + g_p, \tag{1.10}$$

where the left side of each equation is the time derivative of each charge carrier concentration, $r_{n,p}$ are the pair recombination/generation rates of electrons and holes from capturing centers in the material ($r_{n,p} < 0$ for generation), and $g_{n,p}$ are the generation rates of electrons and holes from other process (such as electromagnetic radiation), show the change in carrier concentration with respect to carriers moving (current flow), appearing (generation), or disappearing (recombination) within the material. In equilibrium, recombination and generation processes ($r_{n,p}$) cancel each other out, but these processes also serve to return carrier densities back to their equilibrium values when necessary. (See reference [85] for more information)

1.1.4 Semiconductor Junctions

A junction of a p-type and n-type semiconductor forms the most basic semiconductor junction, the PN junction, or a diode. The Fermi level of the entire device (in equilibrium) remains constant forcing the valence and conduction bands to bend up from the n-type region and down from the p-type region near the junction. Physically, the p-type material contains many more holes than the n-type material, and the n-type material contains many more electrons than the p-type material. Forming a junction between the two materials

causes holes to diffuse from the p-type region to the n-type region and electrons to diffuse from the n-type region to the p-type region. This process tries to make an equal number of holes and electrons exist throughout the entire device. The movement of these charge carriers in the device creates an electric current going from the p-type to the n-type material. The movement of these charge carriers also leaves behind the ionized dopants in each region breaking charge neutrality near the junction, and ultimately, creating an electric field in the junction directed from the n-type region to the p-type region. The electric field causes charge carriers to drift in the opposite direction of the diffusion process. In equilibrium, the two processes create a region near the junction where no free charge carriers (or very little) exist known as the depletion region, and the drift current completely cancels the diffusion current in the device.

If we apply an electric potential across the device such that the higher potential is connected to the p-type material, the applied potential reduces the band bending at the junction. Since the thermal excitation of the electrons, governed by the Fermi function, is exponential in energy (see Equation (1.1)), the reduced barrier leads to an exponential increase in the number of electrons(holes) in the conduction(valence) band available for diffusion at the junction. As a result, the diffusion current through the depletion region depends exponentially on the applied voltage. The drift current that, at equilibrium, served to counteract the diffusion current remains small leading to a net current through the depletion region. After diffusing through the depletion region electrons(holes) from the n-type(p-type) region increase the minority carrier concentration in the p-type(n-type) region. To maintain the proper carrier concentration within the bulk region, the extra minority carriers recombine with majority carriers. The source connected to the device serves to maintain the proper majority carrier concentration in each bulk region matching the diffusion current through the depletion region. We call this a forward biased diode.

Reversing the electric potential instead increases the band bending which exponentially decreases the number of charge carriers available for diffusion. The equilibrium drift cur-

rent remains about the same leading to a small current across the depletion region. The equilibrium value of diffusion current is very small, so with increased reverse biasing the current remains small.

For real diodes, continually increasing the reverse bias leads to a large increase in current caused by various breakdown mechanisms. Other effects such as recombination and generation of carriers in the depletion region, high-level injection at large voltage biases, and voltage drops across the bulk regions also lead to deviations from the ideal diode model above. For more information see reference [75].

1.1.5 Bipolar Junction Transistor

The development of the bipolar junction transistor (BJT) single-handedly changed the course of history as we know it. Created in 1948 by John Bardeen, Walter Brattain, and Walter Hauser [6], this device replaced large vacuum tubes and gave rise to the electronics and computing industry of today. The BJT consists of two PN junctions sandwiched together such that central region is smaller than the minority carrier diffusion length (usually <1 μm, but down to tens of nm today). The stack can be NPN or PNP where the letters refer to the type of doped semiconductor materials. For our discussion, we refer to the NPN BJT, but the same theory holds true for the PNP by swapping the charge carriers and reversing the junction names. This device has three contacts, the base, the emitter, and the collector. Conventionally, the doping of the emitter is larger than the base, and the base larger than the collector. The junctions are formed between the collector and base (CB junction) and the base and emitter (BE junction). The device has four possible modes of operation based on the voltage biasing of each junction: forward-active mode, saturation, inverse mode, and cut-off, only the forward-active mode will be discussed below.

In equilibrium (no voltage bias on either junction), no current flows within the device. Similar to the diode, in each junction, the diffusion and drift currents completely cancel each other out and create depletion regions at each junction. Due to the higher base and

emitter doping, the depletion region of the CB junction will be larger than that of the BE junction. (Refer to reference [75] for the relation between depletion region width and doping concentrations.)

In the forward-active region of operation, the BE junction is forward biased and the CB junction is reverse biased. The forward bias on the BE junction, similar to the diode, causes a shift in the electronic bands of the base and emitter allowing electrons(holes) to diffuse from the emitter(base) into the base(emitter). The reverse biased CB junction creates more band bending at the junction which serves to lower the CB equilibrium diffusion current, but the small, equilibrium drift current of holes(electrons) from the collector(base) to the base(collector) still exists. Due to the small size of the base, most of the electrons injected by the emitter into the base can diffuse straight through base and into the collector instead of recombining in the base. Also, due to the higher emitter doping, the electron diffusion current from the emitter will be larger than the hole diffusion current from the base. Comparing the base current contributions to that of the collector and/or emitter current gives a useful current gain. See reference [76] for more details, derivations, and non-ideal effects.

An important parameter for the current gain in BJTs is the emitter injection efficiency which is the ratio of the electron diffusion current from the emitter to the base (for NPN) and the total emitter current. Increasing the doping of the emitter with respect to the base helps to increase the efficiency by making more electrons diffuse from the emitter than the holes from the base, but a semiconductor can only be doped so much (about 10^{18} cm^{-3} in silicon) before the the doping causes significant changes in the carrier statistics, mobilities, and band gap [32, 69, 85, 86]. Another approach is to use a larger band gap material for the emitter than the base [119]. This effectively makes a larger barrier for the holes from the base than the electrons from the emitter increasing the latter by an exponential dependence on the difference in band gap of the two materials [57]. The exponent is also inversely dependent on temperature, so lowering temperature will exponentially increase the injection efficiency as well. Although different approaches exist, only the approach

applicable to this thesis will be presented below.

Silicon-Germanium Heterojunction Bipolar Transistors

Silicon and germanium are both semiconductors, have the same number of valence electrons and both crystallize into the diamond lattice, making these two elements obvious choices for band gap engineering. By creating a silicon-germanium (SiGe) alloy, tuning the band gap between 0.66 eV (pure Ge) and 1.12 eV (pure Si) becomes possible. Putting this new semiconductor as the base in between a silicon emitter and collector gives a controllable, smaller band gap in the base in comparison to the emitter. The addition of this alloy creates two heterojunctions, one between the base and emitter and another between the base and collector, because two different semiconductor materials are used to form each junction (Si/SiGe). The result is a double heterojunction BJT, or simply a heterojunction BJT (HBT). This technological advancement leads to several performance benefits over a classic silicon BJT, but for the interest of this thesis the low temperature gain is the most important [20].

1.2 Micromagnetics Theory

It would be an injustice to the giants who came before me to not discuss the evolution of the field of micromagnetics applicable to this thesis. This short discussion is in no way complete, but should give some of the relevant players and physics necessary to form a picture of where this work fits into the field.

1.2.1 Quasi-Static Micromagnetic Reversal

The Stoner-Wohlfarth model covers the quasi-static magnetic reversal process for single domain particles [103]. Ultimately the model finds the total magnetic energy of the particle as a function of the magnetization and applied magnetic field. The energy can be split into two main contributions, the Zeeman energy and the anisotropy energy. The Zeeman energy

depends only on the magnetization and the applied magnetic field, but the anisotropy energy takes into account the lattice structure, shape, size, and other material parameters of the particle. The minima of the total magnetic energy at a constant applied field and constant magnetization magnitude correspond to stable and metastable magnetization directions of the particle. As the external field is changed, the minima change as well, and the energy barriers between them vary, and at times, approach a saddle point and disappear. This corresponds to switching the magnetization from one stable direction to another [116].

1.2.2 Micromagnetic Magnetization Dynamics

The magnetization dynamics of single domain particles are commonly modeled with the semi-classical, phenomenological Landau-Lifshitz-Gilbert (LLG) equation. The model assumes a constant magnetization magnitude, and describes the motion of the magnetization vector of the particle in an external field. The equation includes a precessional term and a damping term that is dependent on the material [36]. The LLG equation even allows for a semi-classical modeling of single (or groups of) electron spins [59].

1.2.3 Thermal Excitation of the Magnetization

The Néel-Brown model considers the effect of thermal excitation on the magnetization of a single domain particle [13]. This model adds to the Stoner-Wohlfarth model by allowing thermal excitation from the environment to cause the magnetization to move over the energy barriers between different magnetization states of the particle before the energy barrier reaches a saddle point and disappears. The thermal energy for small particles can be large enough to cause the continuous flipping of the magnetization known as superparamagnetism. The Néel relaxation time, or average time between each reversal of the magnetization, is a function of the energy barrier, temperature, and an attempt time that depends on many of the system parameters. The Néel relaxation time, attempt time, energy barrier between magnetization states, and temperature of the particle are related by what is

known as the Néel-Arrhenius Law [117].

1.3 Tunnel Junctions

The simplest form of a tunnel junction consists of a thin insulator between two metals. The Fermi level of the insulator lies within the band gap of the insulator while the Fermi level of each metal lies within the conduction band. At 0 K, the electrons in the conduction band of each metal will see a potential barrier caused by the band gap of the insulator. The barrier height comes from the difference in energy of the conduction band and Fermi level of the insulator, and the width from the physical width of the insulator. Classically, no electrons will be able to move from one metal to the other unless their energy (by applying thermal energy or a voltage), is raised up to the conduction band of the insulator where empty electron states exist. In quantum mechanics, however, particles have a non-zero probability of tunneling through the barrier [39].

For tunneling to occur, an electron from one metal must have the same energy (in general) of an unoccupied state in the other metal [65]. At 0 K, with no applied potential, and identical metals, there will be no tunneling because each metal will have the same empty and filled states. Applying a voltage potential across the junction lowers the Fermi level of the metal connected to the higher potential and shifts unoccupied states down in energy. Electrons from the other junction (lower electrical potential, but higher energy) will then be able to tunnel to the now empty states giving rise to a tunneling current. A larger potential increases the number of available states across from filled states, increasing the number of tunneling events and tunneling current. If we increase the temperature above the 0 K limit with no applied voltage tunneling can also occur due to the Fermi distribution of electrons in each metal, but, the tunneling currents from each metal will cancel each other out resulting in no net current through the junction.

1.3.1 Magnetic Tunnel Junctions

In a magnetic tunnel junction (MTJ), the two metals of the previous example are replaced by ferromagnets. In ferromagnets, the spin degeneracy of electrons is lifted due to the spontaneous magnetization of the ferromagnet caused by the exchange interaction. This causes an additional splitting in the electronic energy levels shown by a shift in the electron density of states where spin states parallel to the magnetization (spin-up) shift down in energy and those antiparallel (spin-down) shift up in energy. The density of states for electrons in a metal is proportional to $\sqrt{E}$ (where E is the energy), so this shift not only causes a higher occupation of spin-up states in comparison to spin-down states, but also the density of available spin-up states (above those occupied) will be larger than that of spin-down states at the same energy level. These effects make the tunneling process, known as spin-dependent tunneling, contingent on both the occupied and available distribution of spin-up and spin-down states [71, 110].

For simplicity we will look at only parallel and antiparallel MTJs, where each direction relates to the magnetization of the two ferromagnets. In the parallel case, the the majority spin-up electron density of states will be shifted down by the exchange energy, and the minority spin-down electrons will be shifted up by the exchange energy in both ferromagnets. We will assume no spins flip during the tunneling process, and $T = 0\ K$.

Similarly to the tunnel junction above, applying a voltage potential across the junction will shift the Fermi level (and conduction band and spin-up and spin-down density of states) of the ferromagnet connected to the higher potential down in energy. The shift opens up available electron states for both spin orientations, but due to the splitting, there will be more available states for the spin-up electrons than the spin-down electrons. Across the junction there will also be more filled spin-up states than spin-down states. The filled spin-up(spin-down) states across from unoccupied spin-up(spin-down) states will tunnel to their respective spin states. This gives two separate tunneling currents, spin-up and spin-down, going in the same direction. Also, due to the density of states and exchange splitting, the

spin-up tunneling current will be larger than the spin-down tunneling current.

For the antiparallel case, to account for the flipped magnetization of the second lead, we flip the spin-up and spin-down reference for that lead as well. For example, the exchange interaction will cause the density of states in the first lead to shift similar to above, spin-up down in energy and spin-down up in energy. The same effect happens in the second lead, but due to the opposite direction of the magnetization, the spin-up electrons in the second lead will be the same as the spin-down electrons in the first lead (the spins will point in the same direction). As a result, for tunneling purposes between leads, in the second lead, the spin-down density of states is shifted down in energy and the spin-up, up in energy. Now when we apply a voltage across the junction, both tunneling currents will be reduced from their parallel values. Specifically, if the second ferromagnet shifts down in energy (higher potential), then it will have less available spin-up states than spin-down states. The first ferromagnet will have less filled spin-down states than spin-up states. The spin-up tunneling current is limited by the lower number of empty states in the second lead, while the spin-down tunneling current is limited by the lower number of filled states in the first lead. The result is a mismatch in both tunneling cases and a lower tunneling current for each as well.

For the general case, when there is an angle, θ, between the two magnetizations, a change of quantization axis is necessary to project the spins of one lead into the $\pm S_Z$ direction of the spins in the other lead. This change in basis leads to a $\cos\theta$ dependence in the tunneling current. There also exists a caveat. When interface-barrier effects are taken into account, it is possible for the antiparallel state to have a larger current than the parallel state caused by spin-flip process at the ferromagnet-insulator barrier [24, 101].

The differences in current give rise to a resistance/conductance dependence based on the magnetization configuration of each ferromagnet. We express the conductance of the junction, G_{MTJ}, using:

$$G_{MTJ} = G_{avg}\left(1 + \cos\theta\right), \tag{1.11}$$

where G_{avg} is the average of the conductance of the parallel and antiparallel configurations. The tunnel magnetoresistance (TMR) of a junction provides a figure-of-merit for MTJs by comparing the change in resistance of the antiparrallel ($R_{\uparrow\downarrow}$) and parallel ($R_{\uparrow\uparrow}$) magnetization configurations with that of the parallel state as in the following:

$$TMR = \frac{R_{\uparrow\downarrow} - R_{\uparrow\uparrow}}{R_{\uparrow\uparrow}}. \tag{1.12}$$

More commonly, the TMR is positive, with room temperature records now up to 604% [46].

Julliere found the first experimental evidence of TMR in Fe-Ge-Co junctions at 4.2 K in 1975, but only accounted for the change in conductance of the MTJ between the parallel and anti-parallel states [51]. Maekawa and Gafvert showed the directional dependence of the magnetization in 1982 [67]. Slonczewski published the complete theory of TMR 7 years later in 1989 [101].

1.3.2 Double Magnetic Tunnel Junctions

Double magnetic tunnel junctions (DMTJs) add another insulator and ferromagnet layer to the MTJ structure described above. Loosely speaking, the first multi-barrier junctions of magnetic particles date back to 1972, where scientists created insulating films with varying amounts of ferromagnet concentrations [37]. At low enough ferromagnet concentration, the transport in these films at low temperatures became dominated by tunneling between the ferromagnetic particles and even showed signs of spin-dependent tunneling. Later, in 1996, Ono *et al.*, formed an array of MTJs and noticed an enhancement in TMR at 4.2K and 20 mK which they attributed to Coulomb blockade in the small size (<1 μm) of each junction [82]. They continued in this direction, fabricated a ferromagnetic single electron tranistor (SET), and proceeded to find oscillations in the TMR with increasing voltage bias across the whole junction [81]. Although this device is close to a true DMTJ, the SET

includes a capacitively-coupled, gated center electrode. Subsequent theory of these devices was published a few years later [7, 114].

Starting in 1997, other groups took the approach of creating small films of many nanoscale particles inside a regular MTJ, also known as discontinuous film MTJs [30, 74, 92, 95]. These devices showed varying results due to the lack of consistent control of the insulator barrier thickness on each side of the many particles and/or number and size of particles in each film. The first, true DMTJ was fabricated in 1998 by Montaigne *et al.* and showed an increase in TMR at low temperatures greater than two MTJs in series. The device also had a better voltage bias dependence on TMR than that of a single MTJ (TMR decreases with increasing voltage bias). The authors specifically noted that consistent fabrication of such devices were difficult due to pin-holes developing in the insulating barrier [72]. Other fabrication difficulties of DMTJs were noted by other groups stemming from inconsistent film growth on the layered structures, but the successful devices also showed a better low temperature TMR [60] and TMR dependence on voltage bias [18].

Multiple theory papers either specifically about or incorporating DMTJs have been published over the years. When the central ferromagnet is significantly small (nanoscopic) and the device is cooled such that the thermal energy (kT) is smaller than the capacitive charging energy of the central particle, charge quantization leads to Coulomb blockade where the particle's energy can only be increased in discrete amounts dependent on the charge of an electron [38]. In normal metals, this leads to sequential electron tunneling. In DMTJs, the presence of the ferromagnets (leads and particle) increases the contribution of a fourth order effect (normally ignored) known as cotunneling. Cotunneling depends on the relative magnetization of the leads and particles, can supercede that of sequential electron tunneling, and can greatly increase the TMR of a DMTJ in the Coulomb blockade regime as compared to a normal MTJ [73, 105, 118]. For a larger system (no Coulomb blockade), the TMR was also shown to increase in the DMTJ as compared to a normal MTJ using Landauer-Büttiker scattering theory, but the analysis ignored inelastic scattering which would cause the TMR

to drop with increasing temperature. This analysis also showed an oscillating TMR with bias voltage, and a better voltage dependence of the TMR in a DMTJ than a MTJ [97].

With the rise of spin-transfer torque (STT) devices, more interest in DMTJs developed. Spin-transfer torque occurs when a spin current caused by spin-dependent tunneling induces magnetization motion in one of the ferromagnets in a MTJ or DMTJ. The effect can lead to magnetic switching or magnetization precession useful for non-volatile, low-powered memory or microwave oscillators, respectively [88]. In 2003, Berger published a theory paper suggesting that a properly configured DMTJ could drive more spin-torque in the central ferromagnet than regular MTJs [9]. Later, in 2005, Huai *et al.* showed experimentally that the DMTJ structure used a smaller current (therefore less power) for switching [44]. Worledge later explained this result showing that the switching current could be reduced by an order of magnitude using DMTJs as opposed to MTJs [121].

The usefulness of DMTJs does not stop with the industrial promise of low-power, small-size, non-volatile memory. Study of nanodots of different sizes embedded inside the insulating barrier of a MTJ has shown a size-dependent cross-over between tunneling dominated by the Kondo effect and cotunneling. The former suppresses TMR, while the latter enhances TMR, but both cases fall within the Coulomb blockade threshold of particle charging energy and temperature[124]. Another study of DMTJs with a single, nanoscopic particle in the center of the junction showing TMR showed that asymmetrical insulating barriers are necessary to show charging effects and TMR oscillations with applied bias in these junctions. The experiment also showed a shift in the phase of the TMR oscillations in comparison to the Coulomb staircase suggesting this shift was due to spin accumulation in the particle[64]. A closer look into the spin accumulation in the central nanoparticle of a DMTJ revealed the spin-relaxation time for a MnAs naoparticle embedded in GaAs can reach up to 10 μs at 2 K, seven orders of magnitude greater than that of bulk systems[42]. These experiments show how the DMTJ structure can be used to probe the underlying physical properties of the incorporated nanoparticle in the junction.

1.4 Bandwidth Limitations of Croygenic Systems

The use of a cryostat or dilution fridge includes long signal wires connecting the room temperature electronics to the sample under test. These long signal wires give rise to a parasitic capacitance in the measurement system. High resistance samples, such as tunnel junctions with embedded nanoparticles and the MTJs used in this thesis, couple with the parasitic capacitance of the long signal wires resulting in a measurement circuit with a large RC time constant. The large RC time constant limits the bandwidth of the measurement circuit. The resulting bandwidth limits the speed of any electron transport measurements which, in turn, limits the time-resolution of any magnetization dynamics observed through the TMR.

The bandwidth limitation of cryogenic systems is a well-known problem for cryogenic electron transport measurements. Different groups have implemented solutions for similar problems involving qubit readout[108], quantum point contacts[112], and single-electron transistor operation[21, 84, 113]. None of these solutions involve measuring magnetization dynamics with electron transport, but they all involve some form of cryogenic preamplification technique used to improve electron transport measurements in their specfic systems.

1.4.1 Cryogenic Premplification

In Chapter 4 of this thesis, we use a silicon-germanium heterojunction bipolar transistor (SiGe HBT) as a cryogenic preamplifier to increase the bandwidth and signal-to-noise ratio of a TMR measurement. Both improvements come from the transconductance of the transistor where a change in the base-emitter voltage leads to a change in the collector current[43]. The transistor effectively "hides" the high impedance of the junction and the parasitic capacitance of the long signal wires from each other. At the input, or base, of the transistor, the high impedance junction only sees the low base-emitter capacitance of the SiGe HBT resulting in a larger input bandwidth in comparison to the initial measure-

ment system. At the output, or collector, the current is sent to a low input impedance, transimpedance amplifier (TIA) external to the cryostat. The transistor only allows the parasitic capacitance of the signal wires to see the low input impedance of the TIA resulting in a larger output bandwidth in comparison to the initial measurement system. Overall, the new measurement system will have a net increase in bandwidth in comparison to the initial measurement system. Furthermore, the low temperature environment allows the SiGe HBT to introduce less noise during the first stage amplification process of the signal giving rise to an overall greater SNR. These results will be discussed in greater detail in Chapter 4.

CHAPTER 2

SAMPLE FABRICATION

This section includes the use of chemicals that can potentially cause various levels of harm if used, stored, or disposed of improperly. Remember to refer to the Safety Data Sheet of each chemical before attempting any part of the following procedures.

In our lab, we use electron beam lithography and shadow evaporation deposition to fabricate nanoscale devices. Although the overall process is pretty easy there exist nuances that are important in creating a more consistent end product. Various issues can plague the fabrication process outside of our control including deviations in the electron beam during lithography, or problems with the development or lift-off processes. Due to this fact, it is very important to keep a tight control over every adjustable parameter in the process to minimize variances in fabrication.

The sample fabrication process can be summarized in the following steps. First, a 100 mm silicon wafer is spin coated with a bilayer electron beam resist stack. Next, we use a scanning electron microscope (SEM) to write patterns into the resist in a process known as electron beam lithography. Then, the pattern is developed in a chemical bath. After developing the pattern, materials are deposited into the pattern. Finally, the sample is put into a solvent bath to remove the unwanted material leaving behind only the the desired structure.

Normally, we spin coat an entire wafer, then we break off smaller, 1 cm X 1 cm chips as needed. The overall process (excluding the spin coating) takes about a day to complete; however, we tend to fabricate multiple samples at one time on a single chip. Also, once a fabrication recipe has been perfected, it is possible to have multiple chips at different stages of the process. For example, while one sample is pumping down in the evaporator chamber, we can perform lithography on a different chip. Staggering the process in this

way allows for about 2 chips to be processed each day. Each part of the fabrication process will be described in more detail in the following subsections.

2.1 Wafer Preparation

2.1.1 Wafer Cleaning

As stated previously, we use 100 mm silicon wafers in our fabrication process. The wafers are coated with a dry oxide giving the surface a purple tint as shown in Figure 2.1 (a). At the time of writing this thesis, there are plenty of wafers left; however, in the future, if any pure silicon wafers need to be coated, Georgia Tech has these capabilities.

Before spin coating, the wafer needs to be cleaned. There could be a lengthy debate on the proper way to clean wafers, but we will stick with the simple approach and briefly mention another, lengthier process. Regardless of which cleaning process, it is important to set the stage for success. We always begin by putting on a new, clean pair of gloves to avoid any possible contamination of the wafer surface. After this, we clean a wafer holder by spraying it first with acetone and then isopropyl alcohol (IPA). After blowing the holder dry with compressed air, the holder is closed and placed in the same vent hood the wafer cleaning will take place. Ultimately, the goal is to minimize any chance of contamination after the wafer is cleaned. Figure 2.1 (c) shows the wafer cleaning work space.

In most cases, the wafer will only have small amounts of dust on it. In such a case, simply spraying it with acetone for 10-20 seconds followed by IPA for another 10-20 seconds will suffice for cleaning. Immediately following the spraying of the IPA, the wafer should be blown off until it is dry with compressed air, preferably dry air or nitrogen. The acetone will leave behind a residue if allowed to dry on the surface of the wafer ultimately ruining the final spin coat, so it is important that the IPA is sprayed immediately after the acetone. If it appears anything dried, repeat the process again. Although IPA should not leave any residue, we have noticed a ”gunk” that appears if it is left to dry on the wafer as well. Because of this, the dry air or nitrogen should be blown across the wafer immediately

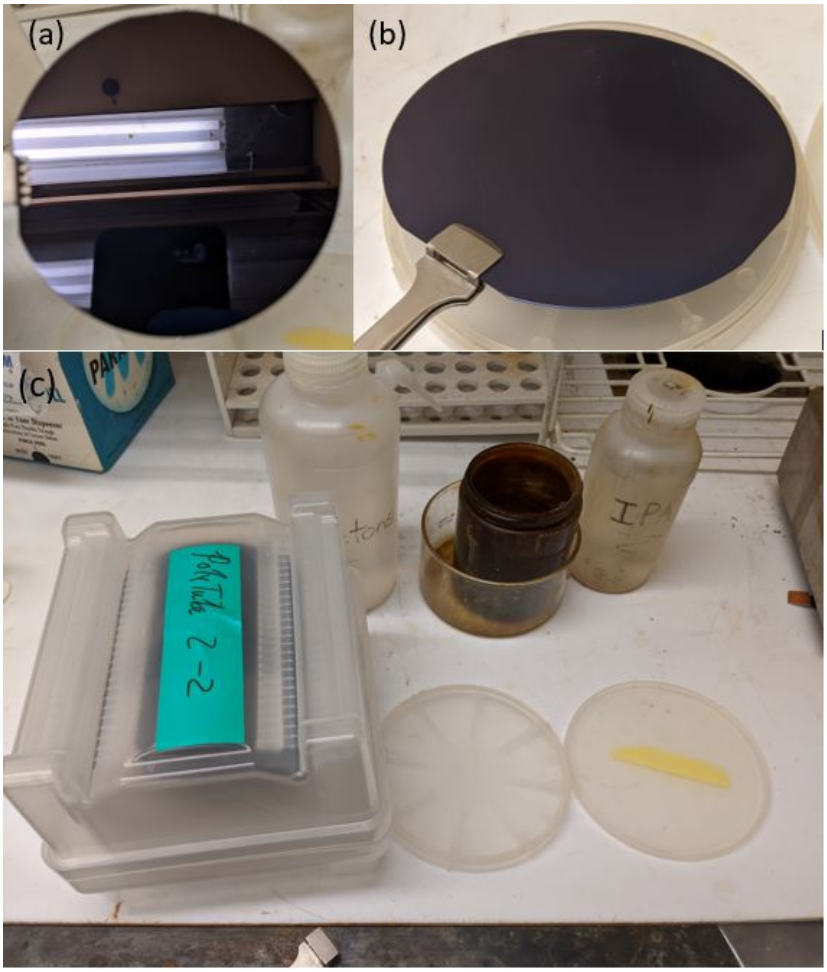

Figure 2.1: Preparation of wafer before spin coating. (a) The reflective side of an uncoated wafer. (b) The nonreflective side of an uncoated, cleaned wafer as it is placed into a wafer holder. (c) Vent hood work area for wafer cleaning.

following the spraying of the IPA. After cleaning, we visually inspect the top, reflective side of the wafer for any blemishes. If the surface looks clean, we place the wafer into the holder so that reflective side is face down on the curved side of the wafer holder as shown in Figure 2.1 (b). The placement is important because any dust or contaminants will only be able to touch the outside edges and not the majority of the wafer which will be naturally suspended over the rest of the wafer holder.

If the wafer still appears to have blemishes on the surface after the simple cleaning process, it is possible that grease or oil contaminated the surface. In this case a more thorough cleaning process will be needed. After re-gloving and preparing the wafer holder,

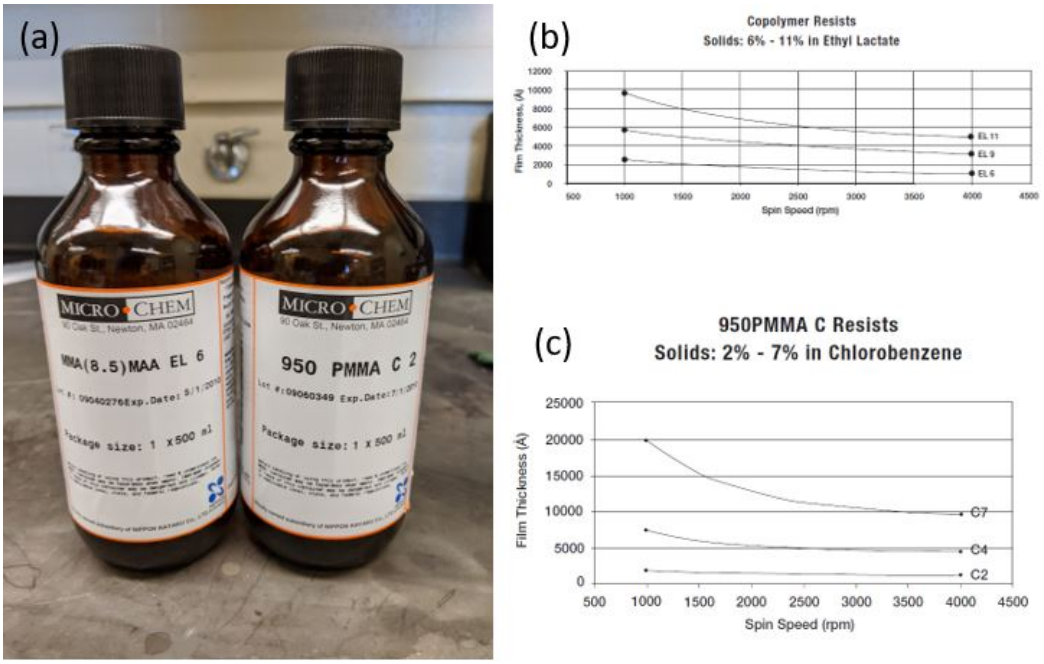

Figure 2.2: Spin coating necessities. (a) Electron beam resist. The copolymer is on the left. (b) Spin curves for the copolymer. (c) Spin curves for the PMMA.

we sonicate the wafer in trichloroethylene, then acetone, and finally IPA for 10 minutes each. Immediately after removing the wafer from the IPA, we blow the wafer off with compressed air until it is dry. At this point, we examine the wafer to verify there are no blemishes on the reflective surface and store it in the wafer holder as previously described.

2.1.2 Wafer Spin Coating

After cleaning, we spin coat the wafer with a Copolymer/PMMA (polymethyl methycrylate) bylayer resist stack. In our lab, we use a 6% mixture of MMA(8.5)MAA in ethyl lactate to make our standard copolymer layer. The PMMA layer uses a 2% mixture of a 950,000 molecular weight PMMA in chlorobenzene. We acquire both solutions and their respective spin curves from MicroChem. Each solution is applied to the surface of the wafer, and the wafer is spun at a predetermined speed given by the spin curves to create a uniform layer of the resist across the wafer surface.

We begin the spin coat process by selecting the proper spinner chuck for the wafer/chip.

In most cases, our lab will spin coat an entire wafer at once, but in the case that a single chip needs to be spin coated, it is important to choose the largest chuck that the wafer can completely cover. The spinner uses a vacuum to hold the wafer while spinning. Using too small of a chuck may not provide enough suction across the wafer to hold it throughout the entire spinning process. On the other hand, using too large of a chuck for a wafer chip may lead to a vacuum leak that will prevent the spinner from operating. In a worse case scenario, the vacuum leak will be small enough to allow the spin process to continue and resist will leak into the vacuum lines and clog them inhibiting proper functionality in the future.

After choosing the appropriate chuck, we load the wafer onto the chuck by centering the wafer on the chuck with the reflective side facing up as shown in Figure 2.3 (b). Next, we turn on the vacuum system and verify the suction by lightly pressing on the edges of the wafer with tweezers. Then, we run the wafer through a test spin sequence to further verify integrity of the system. The spin sequence includes an initial ramp to a desired spinning speed, maintaining the spin speed for some amount of time, and another ramp back down to rest. We have found it best to use the most aggressive ramp rate and spinning speed of the planned process for the test spin sequence.

During the test spin sequence, we perform a quick cleaning process on the wafer to remove any residual dust that may have collected while preparing the spinner. Once the wafer is up to speed, we spray acetone at the center of the wafer to completely cover the wafer as it spins. It is crucial that no section of the wafer dries while spraying the acetone, so it helps to provide a slight oscillation of the contact point of the spray about the center of the wafer. After 10 seconds, we begin spraying IPA in a similar way at the same time as the acetone to ensure no acetone can dry on the surface. After another 10 seconds, we stop spraying the acetone and continue with the IPA for an additional 10 seconds. We then allow the wafer to completely dry with the remaining spinning time.

While the wafer is drying, we fill a glass pipette halfway (about 5 mL) with the copoly-

mer solution. As soon as the wafer returns to rest, we apply the copolymer solution to the surface and wait for 10 seconds before starting the spin sequence. The solution must be applied as a single uniform puddle in the center of the wafer. Any splatter or drops on the wafer surface tend to cause blemishes in the final spin coat. To help with this, we apply a small pressure to the pipette just before putting the solution on the wafer to remove any air bubbles at the tip of the pipette. We ramp the spin speed from rest to 2000 RPM at a rate of 1000 RPM/s. This speed is held for 60 seconds, then, the speed is decreased to rest at a rate of 1000 RPM/s. According to the spin curves, this spin sequence should produce a copolymer layer about 1800 Å thick. After the spinning is complete, the wafer is baked on a pre-heated hot plate for 10 minutes at 150 °C with the freshly coated surface facing up to remove any left over solvent and harden the resist at the desired thickness. Generally, we begin pre-heating the hot plate as a first step in the entire process to minimize wait time and, subsequently, chances of contamination throughout the process.

Next, we return the wafer to the spinner and run the test spin sequence again to cool the wafer. It is important to NOT try to clean the wafer at this point, for any cleaning will remove the freshly cured resist layer. During the spin sequence, we fill a new glass pipette halfway with PMMA. Similar to before, we apply the PMMA solution to the surface of the wafer and wait for 10 seconds before starting the spin sequence. For this spin sequence, we ramp the spin speed from rest to 5500 RPM at a rate of 1000 RPM/s. This speed is also maintained for 60 seconds, then, the speed is reduced back to rest at a rate of 1000 RPM/s. According to the spin curves, this spin sequence should produce a PMMA layer about 1200 Å thick on top of the copolymer layer. After the spinning is complete, the wafer is baked on a pre-heated hot plate for 10 minutes at 180°C. We adjust the hot plate temperature during the previous cool down spin which usually gives it enough time to sufficiently pre-heat. After the wafer is baked, it is spun again to cool it down. Finally, the wafer is placed back in the wafer holder with the freshly coated surface towards the curved part of the wafer holder. We also wrap the entire holder in aluminum foil to minimize any light exposure to

Figure 2.3: Spin coating equipment. (a) Motor controller for the spinner located next to the spin coating station (b) Wafer loaded on the largest spinner chuck. A smaller spinner chuck is located at the top left of the photo (c) Hot plate set for baking the PMMA layer.

the spin coat. We break off 1 cm X 1 cm small chips as needed and return larger portions to the covered holder.

For breaking the chips, we first score the wafer with a diamond blade along one of the crystal axes (as shown by the flat potions of the wafer). Then, we move the wafer onto a clean microscope slide aligning the scored line with the edge of the slide. A slight pressure on either side of the score line breaks the wafer along the crystal axis. We must maintain the axis symmetry of each chip to ensure future samples dice apart properly without damage. On each small chip, we also mark the corners with a diamond blade (see the corners of the chips in Figure 2.4). This helps to set up the SEM later, and allows us to keep track of the

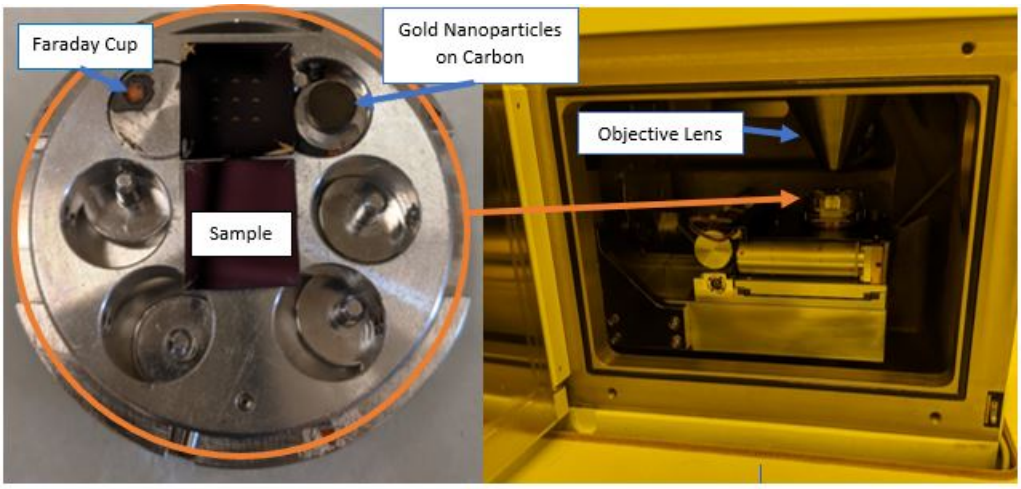

Figure 2.4: Left: Sample mounting chuck for the scanning electron microscope. The previously fabricated sample on the top needs to be imaged before lithography on the bottom sample. The faraday cup at the top left of the chuck and the gold nanoparticles at the top right of the chuck are both used for setting up the electron beam. Right: The specimen chamber of the SEM. the orange arrow points to the sample mounting chuck loaded into the specimen chamber. The blue arrow points to the cone-shaped objective lens housing.

sample orientation if necessary.

2.2 Electron Beam Lithography

After spin coating and separating the wafer into smaller chips, we mount the small chips onto another chuck specifically designed for the SEM using copper tape. At times it may be necessary to image previously fabricated samples prior to performing lithography on a new sample, so both samples can be loaded at once as shown in Figure 2.4. We then load the chuck into the SEM and pump the sample chamber down first with a mechanical roughing pump followed by a high vacuum diffusion pump. The chamber takes about 10 minutes reach the target pressure setting; however, we wait an additional 20 minutes before turning the beam on to ensure the sample chamber reaches base pressure. The base pressure of the system should be on the order of 10^{-5} to 10^{-6} torr (aproximately 0.001 to 0.01 Pa), but this can only be checked by connecting an external vacuum gauge to the system.

2.2.1 SEM calibration

Once base pressure is reached, the SEM must be calibrated for operation. A general idea of the basic operation of the SEM may help to better understand the calibration procedure. Figure 2.5 shows an image of the SEM system with major parts of operation labeled for reference. This SEM produces electrons by thermionic emission of a tungsten filament. We pass electric current through the filament (located in the top of the beam column) until the ohmic heating is large enough to thermally excite electrons above the work function of the tungsten. These emitted electrons are then accelerated down the beam column by an external voltage. The beam column includes magnetic "lenses" that give real-time control of the "optics" of the system. The "optics" of the SEM include a two-stage lens system to control both the beam current and final diameter of the electron beam. The lenses of the system are made from magnetic coils arranged in a way with permeable materials such that a large magnetic field is produced right at the beam in the direction of its propagation. The focal length of the magnetic lens is adjusted by changing the applied field which directly affects the diameter of the beam. The beam first enters the "condenser lens" where the beam diameter is first adjusted. The beam then goes through a small hole in a piece of metal known as the aperture. Increasing the power of the condenser lens broadens the beam at the aperture which allows for less of the total electrons in the beam to pass through the aperture (because electrons that fall outside of the aperture hit the metal surface instead of passing through). This gives a control over the total beam current passed through to the objective lens. The alignment of the aperture and the center of the objective lens is paramount for proper operation. Finally, the objective lens sets the final diameter of the beam. The focal length of the objective lens is set to the sample surface to provide the best image as well. Once the beam hits the sample surface, various processes produce both electrons and photons that can be collected and analyzed to provide useful information about specimen. The beam also passes through "scanning coils" inside the beam column in between the condenser and objective lenses. These coils apply magnetic fields to bend the

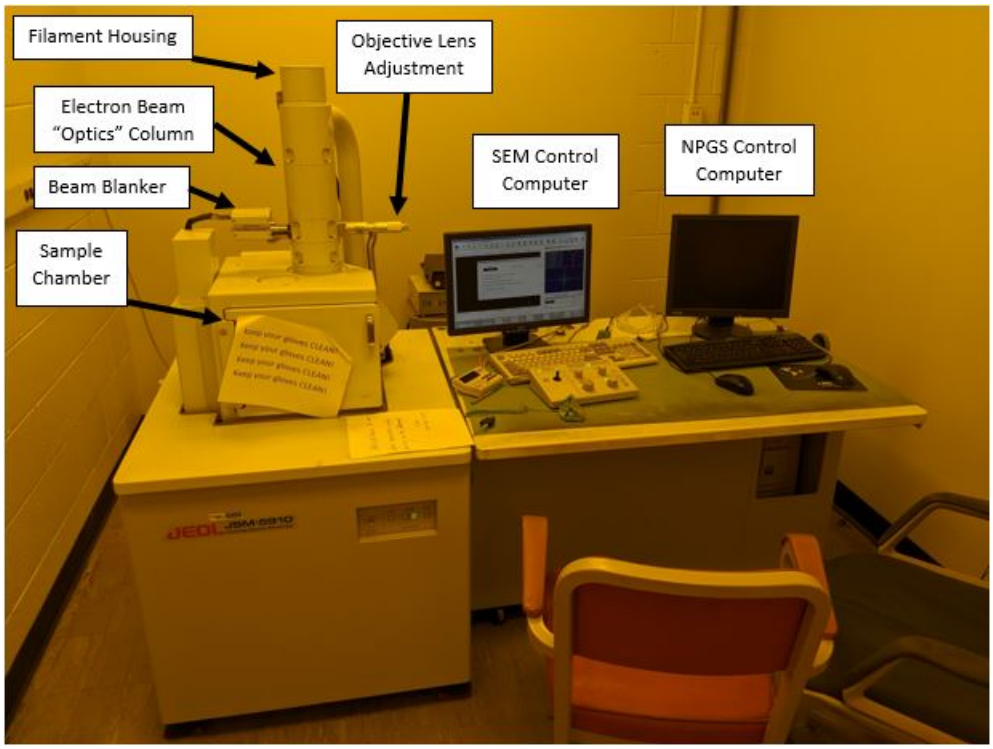

Figure 2.5: Photo of the scanning electron microscope with major parts of operation labeled.

beam and raster it across a sample surface to produce a 2D image of the surface. Although the scanning coils can move the beam, the rastering is limited by the magnification setting, so the entire sample stage is equipped with motors to allow for motion along all three axes (X,Y,Z) as well as in-plane rotation (X and Y axes) and out-of-plane rotation (tilt through Z-axis).

Operation of the SEM for both imaging and lithography both require an initial calibration of the system. The ultimate goal of calibration is to produce a high resolution image of a known standard (usually gold nanoparticles) which ensures proper operation of the system. The standard we use is gold nanoparticles deposited on a piece of carbon as shown in Figure 2.4. The carbon piece in the image is less than 1 cm in diameter. There are two computers near the SEM that both control its operation. For imaging and calibration we use the left computer, and for lithography we use the computer on the right side of Figure 2.5.

After loading the sample and evacuating the specimen chamber, we first move the beam

off of our sample to somewhere else on the SEM chuck. For imaging, this is not as crucial, but for lithography, not moving the beam can place spots on the sample when the beam is turned on (anywhere the beam hits writes a lithography pattern). The beam current tends to drift for a few minutes after turning on the SEM as the filament and coils heat up, so it helps to let the beam remain on for about 5-10 minutes before starting calibration. Before starting any calibration, we set the working distance and acceleration voltage of the SEM. The working distance is the physical distance of the objective lens from the sample stage and sets a limit on the smallest magnification window and overall resolution of the SEM. The acceleration voltage also affects the resolution of the SEM and the penetration depth into the sample. For most of our work, we use a working distance of 10 mm which gives a minimum magnification of 90X. We also normally use the maximum acceleration voltage of 30 kV for lithography, and 5-15 kV for imaging. More information of how these two parameters affect the operation can be found in the equipment manual.

Anytime the filament is changed, gun alignment needs to be completed. The gun alignment allows the user to adjust the heating of the filament as well as its tilt and position in the X and Y axes (assuming Z axis is going up through the beam column). The goal of the gun alignment is to align the thermionic emission of electrons directly along the center of the beam column which produces the largest beam current for a given ”spot size,“ the effective diameter of the final beam, within a specific filament heating range. More information on the gun alignment process can be found in the equipment manual. The beam current during gun alignment is measured by placing the beam on the faraday cup located on the SEM chuck in Figure 2.4. The faraday cup is simply a copper connection to an external ammeter. We have found that gun alignment helps with the overall calibration even if the filament has not been recently changed due to small changes in the filament alignment after heating and cooling.

After alignment, we set the beam current to 10 pA for further calibration (usually a spot size of 20 per the SEM software). Then, we move the beam to the carbon piece

containing our gold standard and begin the process of focusing the beam at the highest possible resolution. When moving the beam, it is extremely important to adjust the Z-axis distance before shifting the stage. For example, the faraday cup lies on the surface of the SEM chuck, but the gold nanoparticles are a few mm above the chuck. The safest approach is to return the beam to the initial height of 20 mm and return the stage to a 0° tilt before shifting the stage. This approach will keep the user from crashing the objective lens shown in Figure 2.4 into the SEM chuck.

Once the beam is centered on the carbon piece, we adjust the z-axis until the sharpest image is produced. After adjusting the z-axis, we perform a finer adjustment using the "Focus" adjustment of the SEM software. The top right pane of Figure 2.6 shows the result of these first steps. We continue increasing the magnification and adjusting the fine focus until we reach around 80,000X magnification. At this point, we should be able to find nanoparticles tucked away in some of the structures on the carbon (such as the pocket shown in the bottom right pane of Figure 2.6). To produce the image shown in the bottom left pane of Figure 2.6, we must adjust both the objective lens position and the astigmatism of the SEM.

The objective lens position can be adjusted using the knobs shown in Figure 2.5 and ensures that the beam is perfectly aligned with the aperture. The astigmatism is the result of uneven focus across the beam diameter and causes blurring of images at high resolution and may turn circular spots into ovals when writing lithography patterns. For both the objective lens and the astigmatism the x and y axes are tuned separately. We have found that iterative adjustments of the astigmatism and the objective lens position produces the best results.

For the objective lens position, the SEM software is set to "OL Wobbler" which shifts the focus up and down continually. If the image shifts in the X direction, the objective lens position knob for the x direction should be adjusted until movement stops. The same approach is taken for the y-axis. After both have been adjusted, the image should go in and

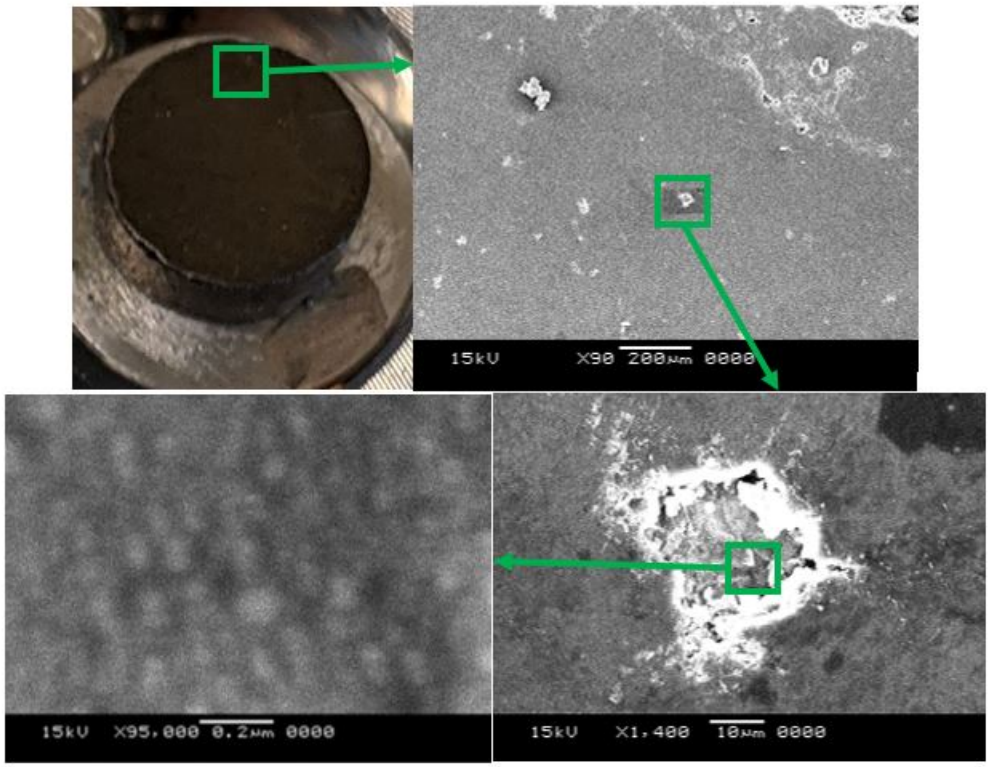

Figure 2.6: Images taken during calibration of the SEM. Each image shows the approximate window of each magnification stage. Top Left: The carbon piece that includes our gold standard. Top Right: Image after setting the z-axis and adjusting the focus. Bottom Right: Further magnification searching for nanoparticles. Bottom Left: Resolved gold nanoparticles.

out of focus but not shift in any direction. After completing the position adjustments, the OL wobbler fucntion is turned off, and the lenses are reset (using the "Lens Reset" option in the SEM software).

The best way to adjust the astigmatism is a topic of debate. The following process is my approach, but others may disagree. Once the sharpest focus has been reached around a magnification of 80,000X, we shift the image slightly out of focus until there appears to be no smearing caused by the astigmatism. If nanoparticles are in view, this just means that we shift the focus until the particles look circular. At this point, each astigmatism direction is adjusted until the best image is found. Then the focus is corrected back to the sharpest image. If particles are not visible, or if a good image cannot be produced

at 80,000X magnification, it is possible to adjust the astigmatism iteratively. Each step requires moving the image in and out of focus using the focus adjustment and watching the smear of the image. If it does not evenly smear in all directions, the astigmatism needs to be adjusted (only one axis at a time in between focus smears) to equalize the smearing of the image. This process is continued until the image sharpens enough to increase the magnetization and/or nanoparticles can be seen.

After these calibration procedures, the SEM is ready for imaging. For the best results, we have found that verifying the gun alignment after calibrating, then repeating the calibration procedure again (if the alignment changes) improves the overall results of both imaging and lithography for nanoscale operation. For microscale operation, repeating the procedure is unnecessary, and even skipping the objective lens position adjustment and astigmatism adjustment may be acceptable. As a general rule, if the beam can reach good resolution at the size scale needed, the calibration should be sufficient.

2.2.2 Nanometer Pattern Generation System

For lithography, we use the Nanometer Pattern Generation System (NPGS) produced by JC Nabity Lithography Systems. The software runs on the computer in the left of the image in Figure 2.5, so control of the SEM must be switched (literally, by a physical switch) to the NPGS computer to perform lithography.

NPGS uses "Run Files" to execute lithography. The run files reference CAD drawings created with DesignCAD LT for each pattern. Although different CAD software can be used, NPGS is specifically designed to work with DesignCAD LT and includes a modified version of the program better suited for creating lithography patterns. More information on how to use DesignCAD LT and how to setup the the patterns and layers can be found in the NPGS manual.

Figure 2.7 shows an example of a lithography run file in NPGS. The entities are used to separate the SEM tasks during lithography. Different tasks may include writing patterns,

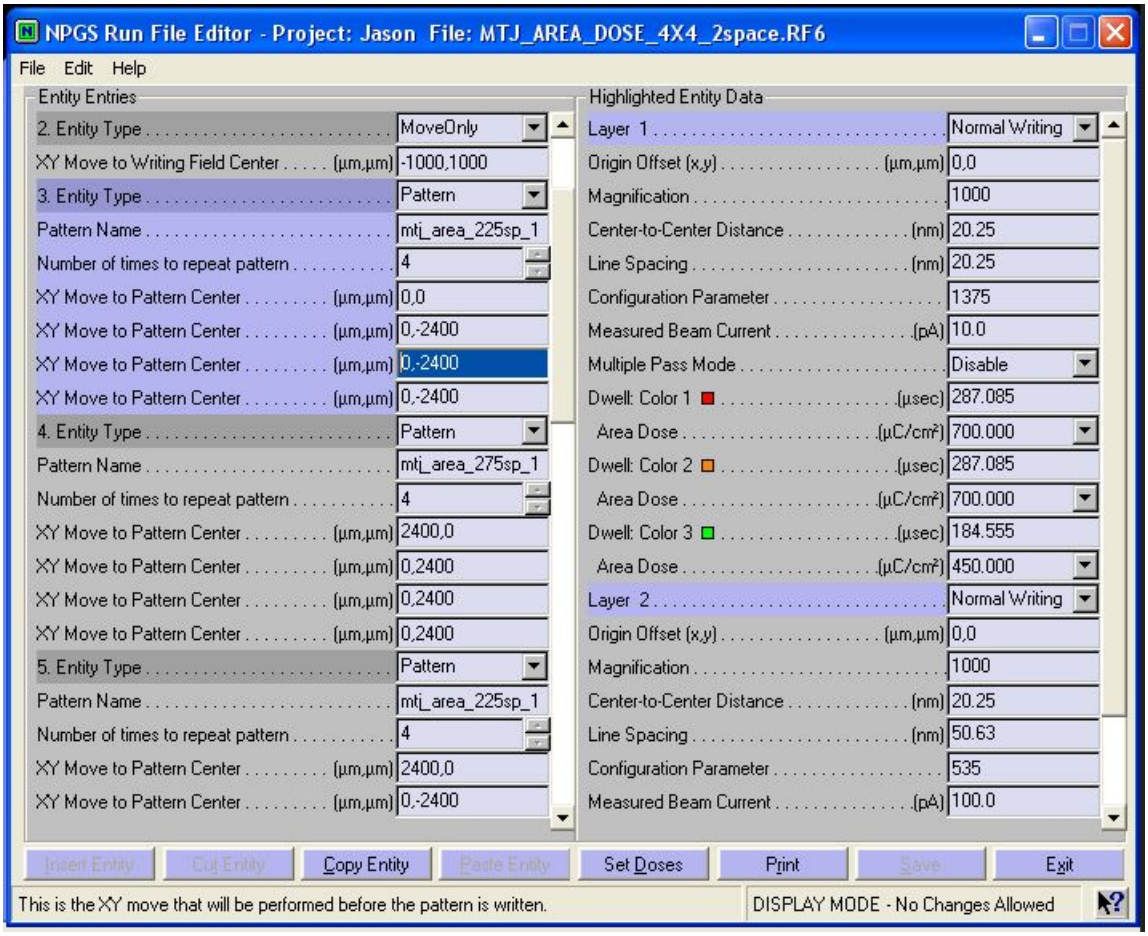

Figure 2.7: Example of a NPGS Run File showing the configuration parameters necessary to setup a lithography pattern.

wiritng arrays of patterns, or simply moving the stage. It is important to note that when switching between the SEM software and NPGS, the reference for the sample stage motion changes as well. In the SEM software, moving ”up” causes the actual stage to move up (in the +Y-direction) which moves the beam down across the sample. In NPGS, moving in the +Y-direction actually causes the stage to move down which shifts the beam in the +Y-direction across the sample.

For writing a single pattern using NPGS, certain information must be passed to NPGS. Starting from the top of the right side of Figure 2.7 and working down the list:

“Origin Offset” specifies any necessary shift for writing a pattern. This parameter is usually only necessary if the beam current or the magnification changes during the writing

process. Both of these changes causes a deterministic (mostly) shift in the beam position.

"Magnification" sets the magnification level and ultimately controls the size of the writing window. For most of our patterns, we use 1000X magnification for features that fit in a 90 μm X 90 μm window around the pattern center, and 90X magnification for features that extend beyond this window but within a 1 mm X 1 mm window. For even larger patterns, increasing the working distance allows for lower magnification extending the writing window up to 1.5 mm X 1.5 mm. Patterns larger than this require "stitching" between different parts of the design each fit to the writing window. Additionally, the "stitching" requires an alignment procedure to make sure everything lines up properly between writing sections. Although possible, these additions greatly increase the complexity of the fabrication process.

"Center-to-Center distance" and "Line Spacing" determine the spacing between individual points during writing. The SEM writes each pattern as an array of discrete points, so the center-to-center distance gives the distance between each discrete point. The line spacing gives the spacing between each finished line of discrete points. The NPGS manual gives more details regarding the proper setting of these parameters based on the size of the pattern and beam current, but we have found that around 20 nm serves well for pattern dimensions greater than a few 100 nm at 10 pA beam current. Patterns smaller than this benefit from smaller spacing, but with a trade-off for overall write speed. For 100 pA beam current, we increase the line spacing to around 50 nm, and for 6 nA to around 300 nm.

"Configuration Parameter" allows the user to calibrate the NPGS software size to ensure the actual beam current matches that used for the pattern exposure calculations.

"Measured Beam Current" lets the NPGS software know which beam current to use for calculating the pattern exposure. We use 10 pA for our smallest features with dimensions of about 5 μm and below, 100 pA for larger patterns that still fit within the 1000X magnification window, and 6 nA for patterns that extend into the 90X window. The smallest beam current gives the best resolution, but larger beam currents decrease the writing time.

A proper balance between write-time and resolution must be found for each sample design.

"Multiple Pass Mode" specifies how the beam should repeat the exact pattern or entity. Instead of using this feature, we write the same pattern twice if necessary.

"Dwell" decides the overall exposure for a particular pattern. The "Color" refers to specific colors within a single layer of the CAD file, because different features may need more or less beam exposure even at the same beam current. The NPGS software calculates the overall exposure from the beam current, center-to-center spacing, line spacing, and either dwell time or dose. Adjusting the dose or dwell time automatically adjusts the other parameter based on the total exposure. Instead of area dose, either line dose or point dose may be used, but I have never had much success using any other type of dose other than the area dose.

"Layer" refers to a layer within the CAD file. We generally use different layers for each level of beam current within our design.

To summarize the NPGS run file setup, each feature of a lithography pattern may need a different dose of total charge to properly write the feature into the electron beam resist. The run file allows us to set the necessary parameters to control this dose for each part of our overall sample design. Although in theory, the exposure is calculable, in most cases experience based estimates and experimentation are necessary to come up with a proper writing formula.

In our lab, we normally write arrays of samples across a single chip and dice the samples later as needed. As a result, the beam must move across the majority of the chip surface while writing patterns. To account for any small tilt of the chip, the NPGS software includes a function called "Direct Stage Control" that calculates the necessary change in focus across the chip surface. Before starting the function, we rotate the stage (if necessary) to align the sample array along the crystal axis.[1] Next, we focus the beam on one of the scratches in the corner of the chip to the highest magnification adjusting the z-axis

[1]This helps minimize damage to the samples when dicing them apart later.

as needed. Then, we start the "Direct Stage Control" function. After starting the function, we shift the stage slightly to a blank spot near the scratches and switch the SEM control to the NPGS computer. Flipping the control switch with no pattern writing stops the raster of the beam and keeps the beam in a single spot in the center of the writing window. Due to the imperfect vacuum and impurities in the system (like carbon from the oil in the diffusion pump), a contamination spot forms on the surface of the chip as electrons interact with impurities on the surface of the chip. After 20-30 seconds, we return the control to the SEM computer and fix the focus (if necessary) using the contamination spot. Using the "Direct Stage Control" window, we save these focus parameters and repeat the focus and contamination spot process at each corner of the chip. The NPGS software calculates the necessary focus adjustments and applies them when writing the patterns. After starting the "Direct Stage Control" function only the SEM software "Focus" adjustment, not the z-axis, should be used.

The contamination spot also serves as a good reference for the beam astigmatism and focus. The contamination spot should appear as a small circle or donut-shaped bright spot. Any deviation from this identifies poor calibration of the beam. Occasionally, the beam may drift while creating the contamination spot giving the appearance of poor calibration. We distinguish between poor calibration and beam drift by adjusting the wait time of multiple contamination spots. If changing the time only changes the brightness of the spot, the beam needs better calibration. In the event that beam drift causes a significant issue with the contamination spot, returning to the gun alignment and adjusting the heating, realigning the gun, and waiting a few minutes may fix the problem.

While writing/using the SEM, the beam tends to drift out of focus. Because of this drift, when we write an array of samples, we first write all of the features needing a 10 pA beam current throughout the entire array. We then go back through the array and write the remaining features. This allows us to write the parts of the pattern needing the highest resolution before the beam drifts too far out of calibration.

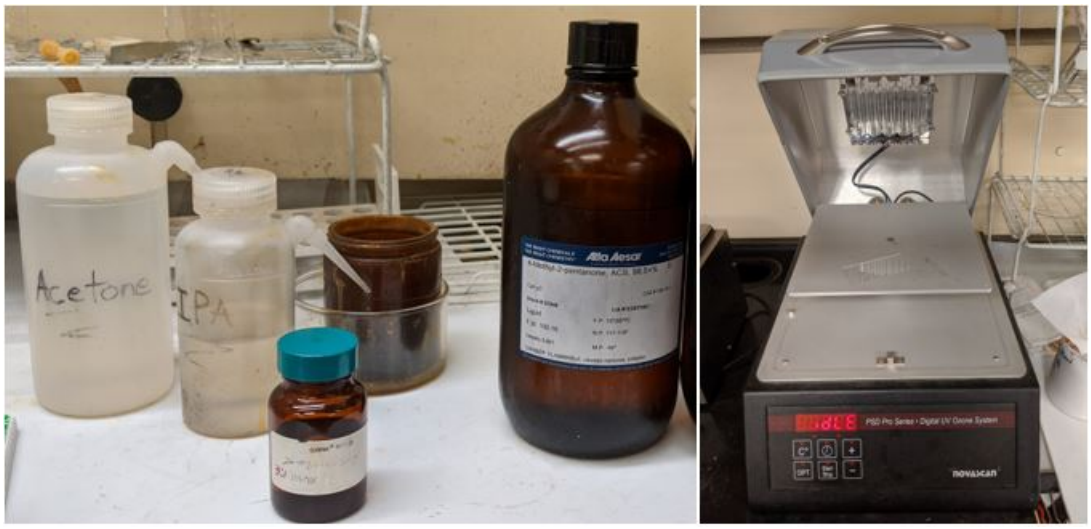

Figure 2.8: Left: Vent hood work area in preparation for development procedure. Right: Ozone cleaner for after development process.

2.3 Developing the Lithography Pattern

When the electrons from the SEM impact the PMMA and copolymer, they weaken the bonds in the vicinity of their impact. Using a chemical wash, we remove these pieces leaving behind a mask on the surface of the chip. The chemical wash consists of a 3:1 mixture of isopropyl alcohol and MIBK (methyl isobutyl ketone, shown on the right side of the left pane in Figure 2.8). Different procedures exist for development, but in our lab, we have found the following process suitable. After filling a small container with the developing mixture shown in the center of the left pane in Figure 2.8, we hold the chip tightly on one corner with tweezers and vigorously shake it in the solution for 60 seconds. Immediately following the 60 seconds in the developing solution, we remove the chip and rinse it in a constant spray of IPA for 10 seconds. Immediately after the rinse, we blow the chip dry with dry air. Although not completely necessary, I have found that following the development process with 5 minutes of ozone cleaning helps to ensure a better deposition and lift-off process. The ozone cleaner we use in our lab is shown in the right side pane of Figure 2.8.

After developing the mask, it is good practice to verify the design with an optical micro-

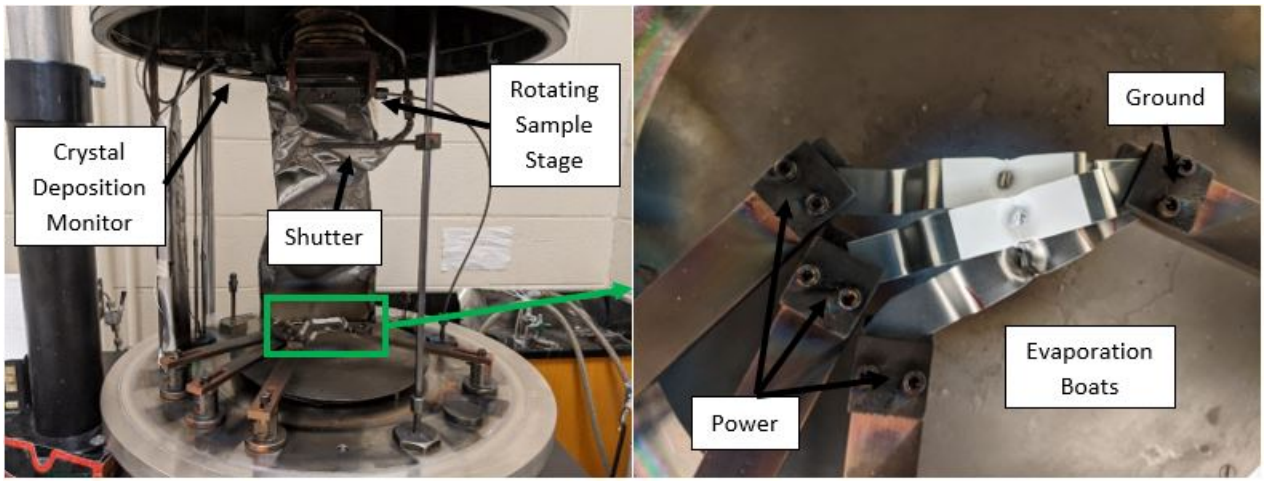

Figure 2.9: Left: Inside deposition chamber showing the crystal monitor, manual shutter, rotating sample stage, and evaporation boats. Right: Close up of 3 evaporation boats mounted and ready for use.

scope. Features below micron-scale cannot be resolved, but major errors in the lithography process will show up and save time from an unnecessary deposition and lift-off. If the pattern appears to be under-developed, going through the development process again may fix the issue; however, keeping a consistent development process and instead adjusting the exposure during lithography has proven to create a more consistent product in my own experience.

2.4 Shadow Evaporation Deposition

Once the mask has been completed, we proceed to deposition. In our lab we make use of a technique known as shadow evaporation deposition. Originally pioneered by Dolan for use in photolithography [26], this process allows for stacking of materials to form tunnel junctions in a single deposition process without breaking the vacuum of the system. This process allows our lab to produce our samples without the need for a clean room. We will tackle the process in two parts. First, we discuss how we deposit materials. Then, we cover the intricacies of the bilayer electron beam resist development and the necessary sample stage rotation during deposition.

We mount the developed samples onto a rotating sample stage inside our deposition chamber shown in the right pane of Figure 2.9. We fill evaporation boats below the sample stage with materials for deposition. The alignment of the evaporation boats and the chip is incredibly important. Due to the stationary nature of the evaporation sources, it is necessary to partially overlap the evaporation boats to minimize the distance between each source, but care must be taken to not block the direct line-of-sight from each source to the sample or to the deposition monitor. The right pane of Figure 2.9 shows two types of deposition boats. Those with white on them are molybdenum coated with alumina while the other is a pure tungsten boat. We generally use the alumina coated molybdenum boats for most metals. We use tungsten boats for gold, silver, copper, and in the rare case that a material interacts with the alumina coated boats (such as the terbium-doped permalloy discussed in Section 5.2.1). When evaporating new materials it may be necessary to try multiple types of boats to find which works best. The evaporation boats are all connected to a single ground and one of three different power rails. This allows for separate evaporation of up to three (or four if aluminum and alumina are both used) different materials by passing electric current through the respective evaporation boat. The electric current heats the material through ohmic heating of the boats.

Once the sample and boats are loaded, we close the chamber and first pump it down to approximately 50-100 mTorr (6-13 Pa) using a roughing pump. A cryopump below the chamber takes the pressure the rest of the way down to 10^{-7} Torr (10^{-5} Pa) for deposition. Once the system reaches base pressure, we preheat each material. When depositing aluminum or precious metals we melt the source material during the preheat. With other materials, we heat them up just before melting because other materials (such as nickel and cobalt) tend to have difficulty remelting. After preheating we deposit the necessary amount of each material.

The crystal deposition monitor shown in Figure 2.9 measures the amount and deposition rate of each material by monitoring the resonant frequency of the crystal as material

deposits to its surface. The crystal is mounted at a similar distance from the source as the sample, but off to the side allowing us to set the deposition rate while the manual shutter covers the sample from any evaporated material. The deposition monitor requires information about each material including the Z-ratio and density for proper accuracy, but also adds an additional "Tooling" parameter to tune the output for each material. Our lab has this information already available for many materials.

After determining the correct parameters for the deposition monitor, the deposition process for most materials is straightforward. We move a switch to choose which evaporation boat to use, increase the current through the boat to melt and evaporate the material, and open the shutter when we reach our target deposition rate (usually between 2-4 Å/s). Once we reach our target thickness of each material, we close the shutter and slowly reduce the current back to zero. Although most materials evaporate at a manageable temperature in the 10^{-6} Torr range, we aim for pressures below 5x10^{-7} Torr for best results (ie. stable deposition rates at lower temperatures).

Most of the samples produced in our lab (including both the MTJs and DMTJs discussed in this thesis) contain one or more tunnel junctions. We make an amorphous aluminum oxide, or alumina, for our insulating barrier. Many researchers use a natural oxidation process by depositing aluminum and exposing it to oxygen; however, we have found success directly depositing alumina by introducing oxygen to the system during the deposition of aluminum. Depositing alumina takes a few more steps than other materials, but our recipe returns consistent results. The recipe starts by setting the deposition rate of aluminum to 2.5 Å/s. At this point, we introduce oxygen gas into the system near the sample at a flow rate of 200 cm^3/min. Shortly after introducing the oxygen, the deposition rate spikes indicating proper formation of alumina. Next, we monitor the pressure of the system until it reaches 10^{-5} Torr. Finally, we slowly adjust the current to the aluminum evaporation boat to set the deposition rate between 3-4 Å/min and open the shutter once the deposition rate stabilizes. Once we reach the desired thickness, we close the shutter,

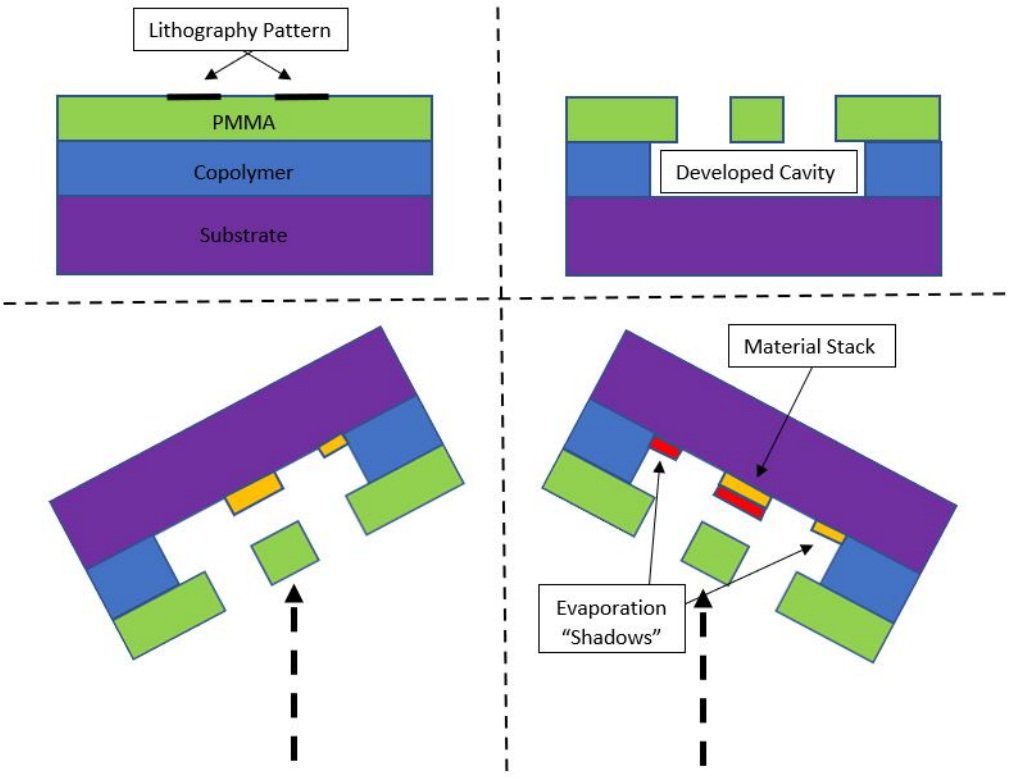

Figure 2.10: Steps showing how the shadow evaporation deposition process allows stacking materials to create tunnel junctions. Note that distances are NOT to scale. Top Left: Side view of bilayer electron beam resist stack with a lithography pattern overlaid on top. Top Right: Side view of cavity formed under the PMMA layer after lithography and development. Bottom Left: The result of tilting the sample stage for deposition. The yellow material is deposited after the tilt from a source directly below the dotted black arrow. Bottom Right: After deposition following the second tilt of the sample stage. The stacked material in the center forms the tunnel junction. The evaporation shadows form as a result of the process, but are not used in the final product. The yellow material was deposited after the first tilt, and the red material after the second tilt.

shut off the oxygen flow, and slowly reduce the current to the aluminum evaporation boat back to zero. After depositing alumina, the pressure of the system may take a few minutes to drop back down low enough to deposit the next material.

The other piece of shadow evaporation deposition involves rotating the sample stage at certain points in the overall process. As stated previously, we use a bilayer stack of the copolymer MMA(8.5)MAA and PMMA prior to lithography. The electron beam resists allow us to design custom masks directly on our substrate. Additionally, when the electrons impact the electron beam resists, the copolymer bonds suffer more degradation than that of

the PMMA bonds. During development, more MMA washes out around the sample design than PMMA causing cavities to form under the PMMA around each design. By placing patterns in close proximity to each other (within a few 100 nm), the cavities below the PMMA will connect creating PMMA "bridges" above empty space above the substrate as shown in the top panes of Figure 2.10. By rotating the sample stage prior to deposition as shown in the bottom panes of Figure 2.10, we deposit stacks of materials while still maintaining electrical connectivity to the bottom material.

2.5 Lift-off Process

After deposition, we remove the remaining electron beam resist and unwanted material through a process known as "lift-off." The electron beam resist dissolves in acetone, so placing the entire chip in acetone removes the left over electron beam resist and any material on the resist surface. Applying a moderate amount of heat to the system aids in the process of dissolving the resist, and spraying the surface of the chip with acetone helps to remove any stubborn, unwanted material stuck to the chip. The acetone level must stay above the surface of the chip throughout the entire process. If at any point too much acetone evaporates out of the container, previously removed material may deposit back onto the surface of the chip becoming almost impossible to remove without damaging the samples.

We place the chip in a small beaker (50 mL is usually sufficient) and cover it with approximately 20-30 mL of acetone. We put the beaker on a hot plate set to 40°C and cover the top of the beaker with aluminum foil. After 20 minutes, we remove the foil and carefully tilt the beaker over a waste container while spraying the chip surface with fresh acetone. This step serves two purposes. First, it allows dissolved resist and removed material to exit the beaker. Second, it aids in the removal of material stuck to the chip surface. Care must be taken to keep the hot chip surface wet with acetone if the acetone level drops below any part of the chip with the beaker tilted. Also, the tilt should be sufficient to allow acetone to

Figure 2.11: Sample in acetone during lift-off.

pour into the waste container, but not so much to cause the chip to flip over on top of the samples, or worse, to fall into the waste container. We keep the beaker tilted and continue spraying for 10 seconds. Then, we re-orient the beaker and continue spraying the acetone until the level returns to normal (about 20-30 mL). At this point, we visually inspect the surface of the sample to verify no excess unwanted material remains around the samples. If material appears to be stuck near the samples, we recover the beaker and return it to the hot plate for an additional 10 minutes and repeat the spraying process as needed.

After removing the unwanted material from the chip, we carefully pickup the chip with tweezers while spraying the sample surface with acetone. After 10 seconds of spraying, we quickly switch to isopropyl alcohol for another 10 seconds. Immediately following the isopropyl alcohol, we blow the chip dry with dry air. Following the lift-off process, we verify proper deposition and lift-off by viewing each sample under an optical microscope.

2.6 Adjustments for MTJs and Double MTJs

For both the MTJs and DMTJs discussed in this thesis, our normal fabrication process produced an insufficient amount of undercut in the MMA copolymer underneath the PMMA layer. For the MTJs, we fixed this issue by using a higher density MMA solution with the same spin coat recipe. Instead of the 6% mixture of MMA in ethyl lactate, we used a 9% mixture increasing the copolymer layer thickness from 1800 Å to 4500 Å. In practice, the developed cavities do not have straight edges like Figure 2.10, but instead, they broaden as they approach the wafer surface. Due to this broadening, after adjusting the exposure, a thicker copolymer layer will produce wider cavities beneath the PMMA layer. The wider cavities in turn allow for larger spacing between lithography patterns while still creating an open cavity underneath a PMMA bridge necessary for shadow evaporation deposition. The thicker layer also causes a larger shift of the deposited pattern on the wafer surface for a given sample stage angle. Putting these changes together, we made MTJs with one 150 nm wide lead and another 300 nm wide lead without overlapping either lead with its evaporation shadow. The top pane of Figure 2.12 shows the DesignCAD drawing of the MTJs used for lithography. The yellow dotted line gives the axis of rotation for deposition. Figure 4.9 in Chapter 4 shows an SEM image of a completed device without the tunneling barrier using gold for better resolution.

Proper fabrication of the DMTJs proved to be much more difficult. The bottom pane of Figure 2.12 shows the DesignCAD drawing used for lithography. The yellow dotted line shows the deposition tilt axis. Once again, we used a larger density solution of the MMA copolymer for spin coating. This time, the 9% solution did not provide a large enough shift of the leads and central particle, so we used an 11% solution increasing the copolymer thickness to 7000 Å. After adjusting the exposure, this still did not provide adequate undercut for successful device fabrication. Instead we saw a pile-up of material at the top edge of the particle evaporation shadow. when depositing Cr-Au for imaging,

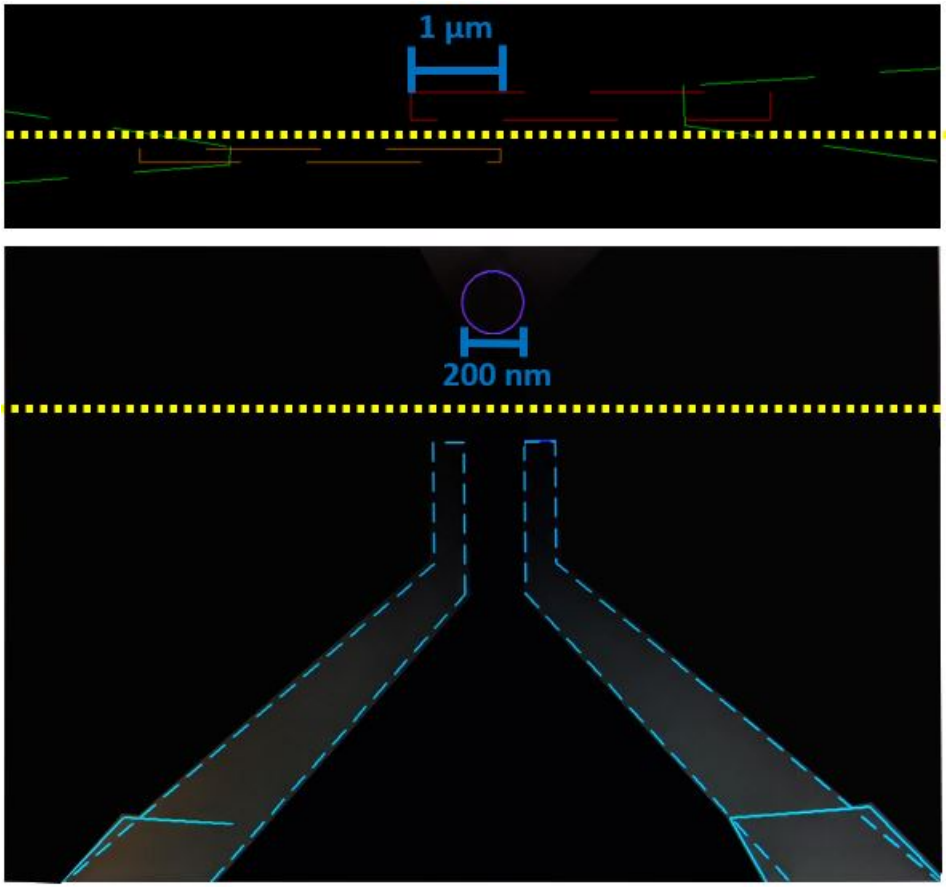

Figure 2.12: DesignCAD drawings of the MTJ(top) and DMTJ(bottom) used for electron beam lithography. The yellow dotted line shows the axis of rotation during deposition.

the extra gold lifted off without issue hiding the underlying issue. After fabricating many electrically shorted samples, we tried imaging by depositing only cobalt. The contrast of the image is much worse than Cr-Au, but we were able to see how the material pile-up from the evaporation shadow of the particle led to shorts across the leads.

Figure 2.13 shows the SEM image of the DMTJ deposited with only cobalt. The red dashed box surrounds the problem area. The brightness of the particle and the material all around it is due to the larger thickness caused by material pile-up not lifting off after deposition. This effect was completely missing with the Cr-Au deposition and many times, even the evaporation particle would be missing. It shows that the when the cobalt attaches to the edge of the resist cavity , it impedes the lift-off, while the Cr-Au, does not have any issues.

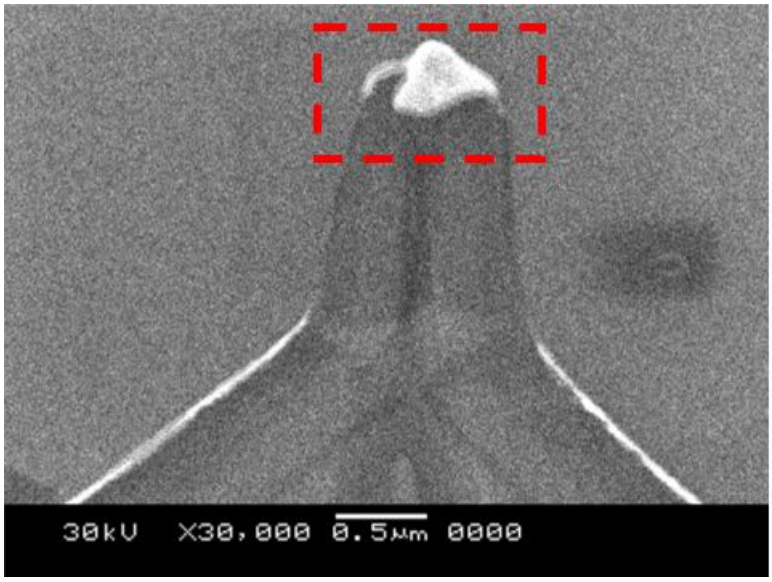

Figure 2.13: Image of DMTJ deposited with only cobalt showing the material pile-up (extra brightness) leading to an electrical short across the leads. A red dashed box surrounds the problem area.

At first we tried adding an extra small exposure dose in the vicinity of the red dashed box. This technique helped to create more undercut in the past, but, with these devices, it only showed minimal improvement. We found that reducing the accelerating voltage during lithography from 30 kV to 15 kV successfully fixed the issue more consistently. Reducing the accelerating voltage causes more back scattering of electrons, due to their lower energy, increasing the undercut of the MMA layer. The trade-off for this approach is less resolution when writing and a need to readjust all of the exposure parameters.

Although this fixed our main issue, the yield of our devices was incredibly small (usually below 10%). We found that imaging the samples after a flat deposition (no rotation), before lift-off showed issues with the lithography. It turned out that the point where the leads approached each other would occasionally over-expose causing a short across the leads. We thought this may be due to the larger dose of this region due to the leads reducing in width as they approached each other. To fix this issue, we redesigned the leads to match that of Figure 5.2 (c) and (c) in Chapter 5. We still did not have a great yield, but occasionally, it reached up to almost 50%. It turns out that most of the bad samples

at this point could be attributed to uncontrollable variations in the SEM operation during lithography (ie. random shifts while writing different parts of the pattern).

2.7 Creating a New Sample Fabrication Process

Any time a new device and/or pattern needs to be developed there are a few important steps to undertake to make sure the fabrication comes out as expected. First, the new pattern needs to be separated into pieces that fit into each beam current (ie. parts within a 5 μm window, 45 μm window, and 1 mm window). In most cases, the parts of the pattern written with the 100 pA or 6 nA beam current will use nearly the same run-file parameters as previously written patterns. The run-file parameters for the parts using 10 pA beam current tend to vary depending on the size and shape of the patterns and the resist thickness.

To find the different parameters, we make exposure arrays. NPGS has a built in function for these arrays, but building the array with each piece separately allows for more control over the exposure parameters of each part of the pattern. Initially, it helps to find the best exposure parameters of each constituent geometrical figure of the design. Specifically, if a small circle exists in the pattern as well as small rectangles (similar to the DMTJ of this thesis) a separate array should be made containing only patterns of each shape. When varying the exposure, it is important to only vary one parameter at a time. Using a matrix where the columns adjust one parameter and the the rows adjust another allows the user to vary two parameters with each lithography/deposition step. In practice, multiple copies of each set of exposure parameters (2-4) helps to account for random errors in the beam writing as well.

The parameters that need to be found include the dose type (point, line, or area), the total dose (usually set by varying the dwell time), and the spacing (both center-to-center and line spacing). After lithography, we perform deposition without any tilts using 10 Å of chromium followed by 150 Å of gold. The chromium seed layer helps the gold stick to the substrate, and the gold gives better contrast for imaging. Instead of performing lift-off,

it is much easier to validate the lithography process by imaging the samples immediately after deposition. Once the best parameters have been identified, we then put the constituent shapes of the pattern together and perform another exposure test varying only the dwell time of each piece. This step is important because the combination of the shapes near each other forming the total pattern tends to change the resulting exposure of each separate piece. Once we identify the best exposure parameters for the entire pattern, we proceed to the tilt tests.

For the initial tilt test, we use the same Cr-Au deposition, but tilt the sample stage similar to the final fabrication process. With each tilt we deposit both the chromium seed layer and the gold to ensure the gold binds properly to the substrate in both tilted configurations. After deposition, we perform the lift-off procedure then image the samples with the SEM. If the images show the expected arrangement (proper overlap and shapes), we proceed by adding in the 100 pA and 6 nA patterns and repeating the the Cr-Au tilt tests. After imaging this final step (assuming the image results are satisfactory), the pattern is ready for device fabrication. At times it may also be necessary to perform tilt tests using the metals for the actual device (with no insulating barrier) to ensure the device materials behave properly with the lift-off process.

CHAPTER 3
CRYOGENIC STUDY OF SIGE HBTS

3.1 Introduction

The charge carrier transport in DC measurements of highly scaled, 90 nm SiGe HBTs showed significant deviations below 16.7 K compared to that of room temperature [127]. The devices still behaved similar to a transistor in that there was measurable gain in the collector current with respect to the base current; however, the Gummel plots showed strange "steps" in both the base and collector currents at reproducible base-emitter voltage biases. Further analysis of these steps in the Gummel plots provides insight into the operation of these transistors at such low temperatures [23].

3.2 Experimental Setup

The measurements were performed using a Quantum Design Physical Property Measurement System (PPMS) DynaCool system with a dilution refrigerator (DR) insert for cooling the devices down to 70 mK. Voltage and current biasing as well as measurement was performed with the specialized Agilent 4156C Semiconductor Parameter Analyzer. GlobalFoundries produced the devices as part of their fourth-generation, 90 nm SiGe BiCMOS technology (GF 9HP). Figure 3.1 shows the structure of this technology. These transistors have a BV_{CEO} of 1.7 V and f_T/f_{max} of 300/360 GHz at 300 K. Samples 1 and 2 have an emitter geometry of 0.1 X 4.0μm^2 and sample 3 has an emitter geometry of 0.1 X 2.0μm^2.

The device structure as seen in Figure 3.1(a), includes ohmic contacts at the base, emitter, and collector terminals using tungsten plugs to attach the copper metalization layer at the surface to the device. The epitaxial SiGe base forms two heterojunctions, one between the heavily-doped, n-type, Si emitter and SiGe base, and another between the n-type, Si

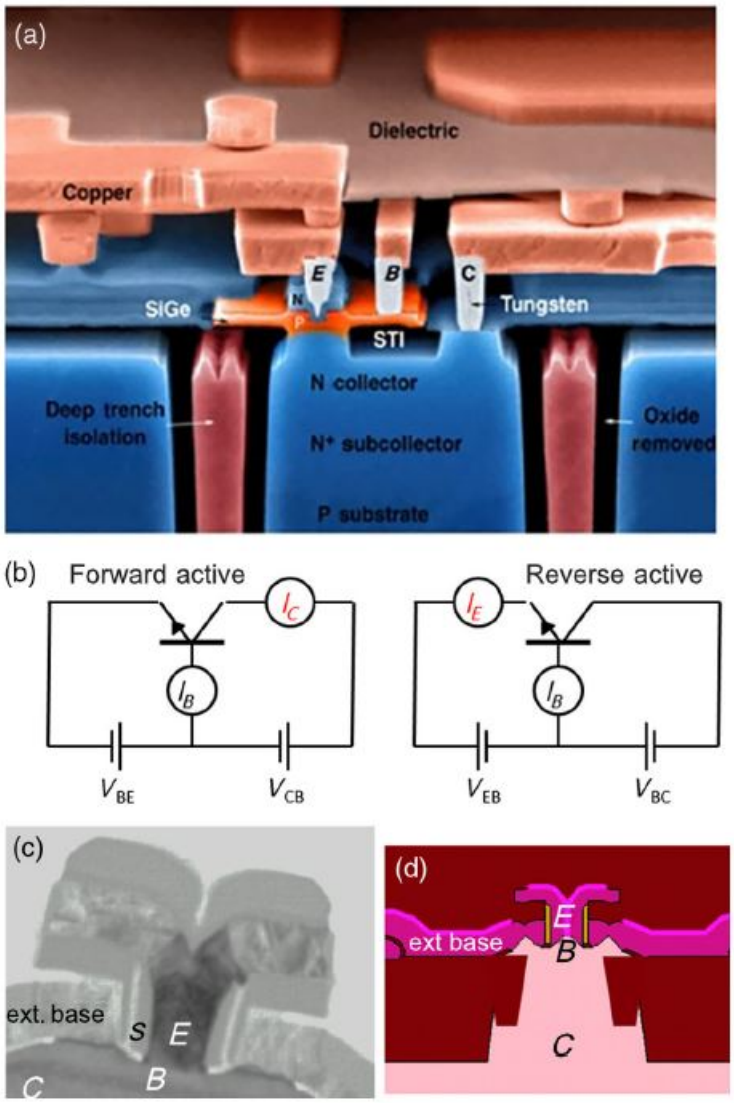

Figure 3.1: Structure of the 90 nm BiCMOS technology. (a) SEM image showing the vertical and lateral structure of an IC form of the a SiGe HBT. (b)Circuit schematics for capturing Gummel plots in both the forward active and inverse (reverse active) modes. (c) SEM image showing the emitter-base spacer (S), extrinsic base, and the emitter, base and collector of the device. (d) Drawing similar to (c) that shows the silicon-nitride (yellow) used for self-alignment. (from reference [23])

collector and SiGe base. The SiGe base extends over the shallow trench isolation region (STI, oxide removed in Figure 3.1(a)). This part of the base, known as the extrinsic base, is heavily-doped (p-type) to provide a low resistance path between the base contact and the intrinsic base, located directly below the emitter. The vertical width of the intrinsic base

is approximately 25 nm. The emitter contact extends into the heavily-doped n-type region above the intrinsic base. The emitter-base spacer, labeled "S" in Figure 3.1(c), isolates the emitter from the extrinsic base. The yellow portion in Figure 3.1(d) shows the silicon-nitride used in the self-alignment process. Traveling down through the intrinsic base, leads to the moderately-doped, n-type collector. The heavily-doped, n-type subcollector below this region reduces the resistance to the collector contact to the right of the STI. The deep trench isolation (Figure 3.1(a)) to the right and left of the device separate different devices on the same die.

3.2.1 Mounting Devices to PPMS Sample Holder

The PPMS uses a gold plated "puck" as a sample mount that connects to low-loss, aluminum, twisted pair wires leading to an external Fischer connector. In an attempt to preserve both the sample mount and the device when re-loading new devices for measurement, we came up with a mounting procedure using indium solder. The indium provides great thermal anchoring between the puck and device. It also allows for easy, non-destructive removal of samples by simply reheating the indium. Furthermore, when cooled, the indium bond is strong enough to provide mechanical stability for wire bonding to the sample surface.

The sample mounting procedure is as follows. The indium is first cleaned by spraying it with a small amount of acetone followed by isopropyl alcohol. We then dry the indium with a lint-free wipe. We cut off pieces of indium into small sections (about 1 mmXmm) and press each piece onto the grounding plane (sample mounting plane) of the puck covering the same area as the device to be mounted. The pressing action uses a small metal pick formed by breaking a set of metal tweezers in half. We use the pick to smear the indium onto the surface, similar to spreading butter on toast, so that the indium adheres to the puck surface. We then place the device on top of the indium in the orientation best for future wire bonding (ie. rotated so each pad of the device can be bonded to the pads of the puck

without shorting the wire bonds). We heat the entire puck with a hot plate to 200°C.

The leads on the puck that connect to the PPMS come out of the bottom of the puck. As a result, the heat transfer to the ground plane is poor. To overcome this problem, we drilled holes in a small piece of aluminum for the leads to sit in. This allows the underside of the puck ground plane to directly contact the aluminum, which, in turn, is in direct contact with the hot plate. The direct contact allows for much better thermal conduction from the hot plate to the puck ground plane. By placing the aluminum stand onto the hot plate first and bringing it up to temperature, the indium will melt in just a few seconds after placing the puck onto the aluminum stand.

We then use the back of a wooden applicator (a small wooden rod about 1 mm diameter) to press the device against the puck pushing excess indium out from under the device. The excess indium forms into small blobs around the device. We use wood to avoid damaging the face of the device. When pressing on the device, it is important to avoid pressing against the pads to be used for wire bonding if possible. We then remove the puck from the hot plate and allow it to cool to room temperature before proceeding. If the blobs of indium are larger than the vertical width of the device, they chance shorting future wire bonds to the ground plane. To minimize this risk, we carefully cut off the tops of any large blobs using a razor blade. The device can then be wire bonded as needed and loaded into the PPMS.

The removal process is simple. First, we remove the wire bonds by pulling the puck-side of the wires with tweezers. Then, we heat the puck to 200°C again. Once the indium melts, we remove the device with tweezers. The excess indium left behind on the puck is nearly impossible to completely remove; however, a new device can be mounted using the same procedure after adding more indium as needed. The previously left over indium re-melts to help bond the next device as well. In the end, both the device and the puck can be reused for future experiments without risk of damaging the device (compared to using silver paste) and without sacrificing thermal conductivity between the puck and device (compared to using N-Grease).

3.3 Gummel Characteristics

Gummel plots for each sample are shown in Figure 3.2. The Gummel plots were acquired using the circuits from Figure 3.1(b). The forward active mode corresponds to the normal amplifying configuration of a transistor where, for an NPN transistor, the base-emitter junction is forward biased ($V_{BE} > 0\ V$) and the base-collector junction is reverse biased ($V_{CB} > 0\ V$). The inverse mode is similar to the forward active mode; however, the entire transistor is flipped so that the collector acts as the emitter and the emitter acts as the collector. In both cases, the Gummel plots are acquired with $V_{CB} = 0\ V$ ($V_{EB} = 0\ V$ for inverse mode) in order to remove the effects of different collector (emitter) doping between different devices in the forward active (inverse) mode. The current density is calculated based on the output current and emitter geometry to better compare different devices as well. These two adjustments allow for an "apples-to-apples" comparison of the measured devices.

The insets of Figure 3.2 show the room temperature gummel plots of each device in the forward active and inverse modes. As expected, the base and collector (emitter for inverse mode) current densities are both exponential with respect to the base-emitter voltage (base-collector voltage for inverse mode) as shown by the linear region of semi-log plots. The linear region of the gummel plots suggest normal drift-diffusion transport of minority carriers within the devices [76]. The current gain, defined as

$$\beta_{DC_{forward}} = \frac{J_C}{J_B} \tag{3.1}$$

for the forward active mode, and

$$\beta_{DC_{inverse}} = \frac{J_E}{J_B} \tag{3.2}$$

for the inverse mode, of the linear regions from $0.5\ V < V_{BE} < 0.7\ V$ for the forward

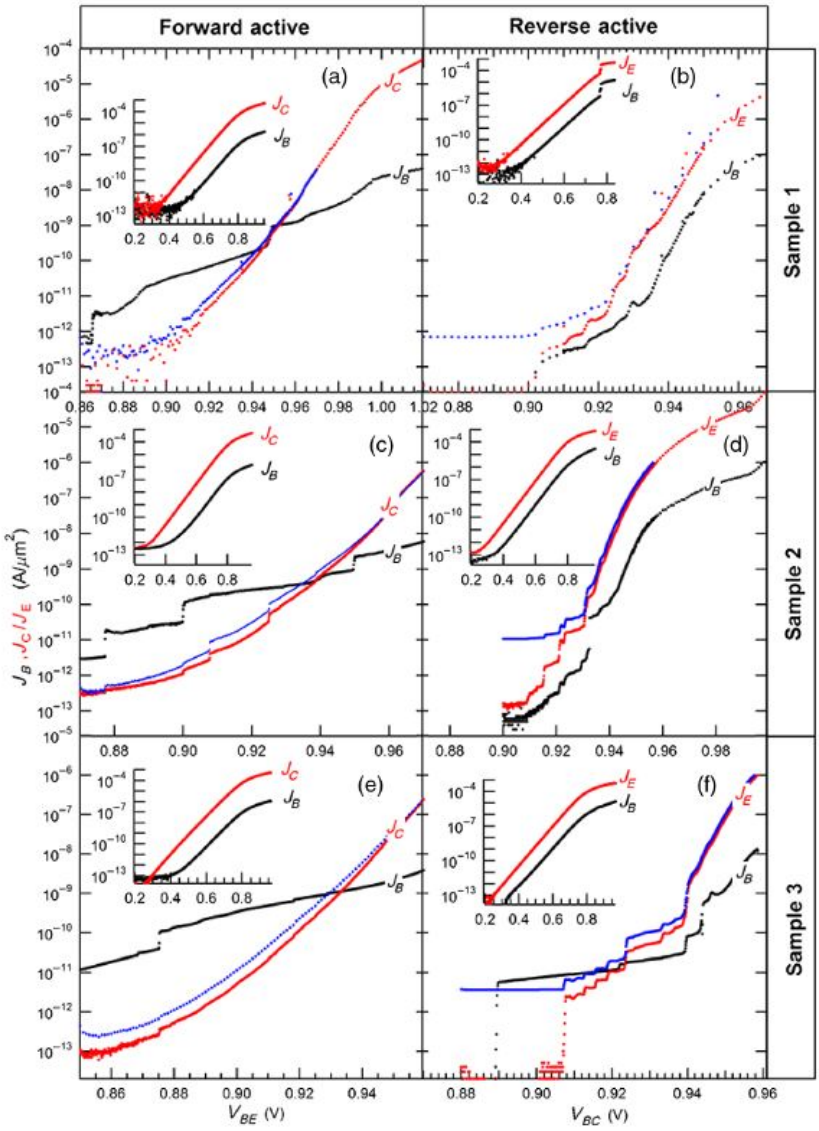

Figure 3.2: Gummel plots for Samples 1, 2 and 3 measured in forward active mode in (a), (c), and (e), and inverse (reverse active) mode in (b), (d), and (f), respectively. Figure 3.1(b) shows the circuits for measuring the forward active and inverse modes. The small insets were measured at room temperature, while the major plots were measured at T = 70 mK. The y-axis gives the current density based on the emitter geometry of each device with each current density labeled according to the terminal being measured. The x-axis corresponds to the applied base-emitter voltage (forward active) or base-collector voltage (inverse). The room temperature measurements (insets) were measured with $V_{CB} = 0\ V$ (forward active) and $V_{EB} = 0\ V$ (inverse) At T = 70 mK, the red plots correspond to $V_{CB} = 0\ V$ (forward active) and $V_{EB} = 0\ V$ (inverse), while the blue plots correspond to $V_{CB} = 0.5\ V$ (forward active) and $V_{EB} = 0.2\ V$ (inverse). The base current density is not affected by changes in V_{CB} in forward active mode or V_{EB} in inverse mode. (from reference [23])

active mode and $0.5\ V < V_{BC} < 0.7\ V$ for the inverse mode are approximately 400 and 35, respectively at room temperature. The larger gain in the forward mode is to be expected due to the significantly higher doping of the emitter compared to that of the collector.

The main plots in Figure 3.2 were acquired at 70 mK. A few observations stand out for these plots. First, there appear to be discrete steps in all of the current densities at 70 mK suggesting a break down of the normal model of drift-diffusion transport used for low injection conditions in BJTs. To further accentuate this point, there is no longer a constant current gain region in either the forward or inverse modes showing a decoupling of the base and collector (or emitter in inverse mode) currents at low temperature in comparison with room temperature. In fact, in every plot except for the inverse modes of Samples 1 and 2, there occurs a region in which the base current density is larger than the collector density (or emitter current density in inverse mode) resulting in a current "gain" less than one for low bias voltages. Furthermore, the curvature of the collector current density in the forward active mode below $V_{BE} = 0.98\ V$ is positive which indicates quantum tunneling through the base region [23]. A similar positive curvature can be seen in the emitter current density of the inverse mode below $V_{BC} = 0.94\ V$, suggesting this same transport phenomenon despite the biasing direction. For the low temperature plots, an additional Gummel plot was acquired where $V_{CB} = 0.5\ V$ in the forward active mode and $V_{EB} = 0.2\ V$ in the inverse mode. In either case, the base current density remained constant indicating a decoupling of the base current with respect to the collector-base (emitter-base) junction in the forward active (inverse) mode. Although the collector (emitter) current density in the forward active (inverse) mode shows a slight deviation by adjusting the collector-base (emitter-base) junction biasing, the effects quickly disappear as the current densities increase past the unity gain level.

In regards to cryogenic preamplification, the low temperature gain and power dissipation of the transistor are very important. For the devices in Figure 3.2, the inverse mode has unity gain at a lower power dissipation for all devices measured. If we define the power

Table 3.1: Approximate Gummel parameters for a current gain of 10 in each sample and configuration shown in the Gummel plots of Figure 3.2

Sample - Configuration	V_{BE} or V_{BC}	J_B	J_C or J_E	$P_{forward}$ or $P_{inverse}$
Sample 1 - F	0.965 V	2 nA/μm^2	20 nA/μm^2	21.2 nW/μm^2
Sample 1 - I	0.924 V	1 pA/μm^2	10 pA/μm^2	10.2 pW/μm^2
Sample 2 - F	0.96 V	3 nA/μm^2	30 nA/μm^2	31.7 nW/μm^2
Sample 2 - I	0.935 V	60 pA/μm^2	600 pA/μm^2	617 pW/μm^2
Sample 3 - F	0.945 V	3 nA/μm^2	30 nA/μm^2	31.2 nW/μm^2
Sample 3 - I	0.944 V	60 pA/μm^2	600 nA/μm^2	623 pW/μm^2

dissipation density as

$$P_{forward} = V_{BE}J_B + (V_{BE} + V_{CB})J_C \tag{3.3}$$

for forward active mode and

$$P_{inverse} = V_{BC}J_B + (V_{EB} + V_{BC})J_C \tag{3.4}$$

for inverse mode, we can compare the power dissipation for each configuration of each device. Using a current gain of approximately 10, Table 3.1 compares the power dissipation density of each sample in each configuration. At a gain of 10, there is no longer a deviation between the collector (emitter in inverse mode) current density from a change in the collector-base (emitter-base in inverse mode) voltage bias making this a good reference of comparison between samples and configurations.

In the forward active mode, all 3 samples have similar power dissipation densities in the range of tens of nW/μm^2. Recalling the emitter geometry of each device, 0.1 X 4.0μm^2 for Samples 1 and 2 and 0.1 X 2.0μm^2 for Sample 3, we find a power dissipation as low as 6.24 nW for Sample 3 up to 12.7 nW for Sample 2. Considering the PPMS has a cooling power of 250 nW at 100mK, these values of power dissipation make this generation of SiGe HBTs phenomenal candidates for deep cryogenic pre-amplification. The inverse mode has gain at even lower power dissipation, specifically, as low as 4.08 pW for Sample

1 up to 247 pW for Sample 2. This gain at a lower power dissipation could prove to be useful in specific cases; however, the high-injection roll-off of Sample 1 seen in Figure 3.2 at $V_{BE} = 1.02\ V$ occurs at a much higher gain of about 1000, than that of any of the inverse mode configurations. Additionally, the forward active base and collector currents of Samples 1 and 3 appear to be more stable, with less oscillations or steps in the positive gain region than their inverse mode counterparts (base and emitter currents). Regardless of these observations, the inverse mode still provides an option for extremely low power (<1 nW), deep cryogenic (<100 mK) operation.

3.4 Shift of Current Densities with Temperature

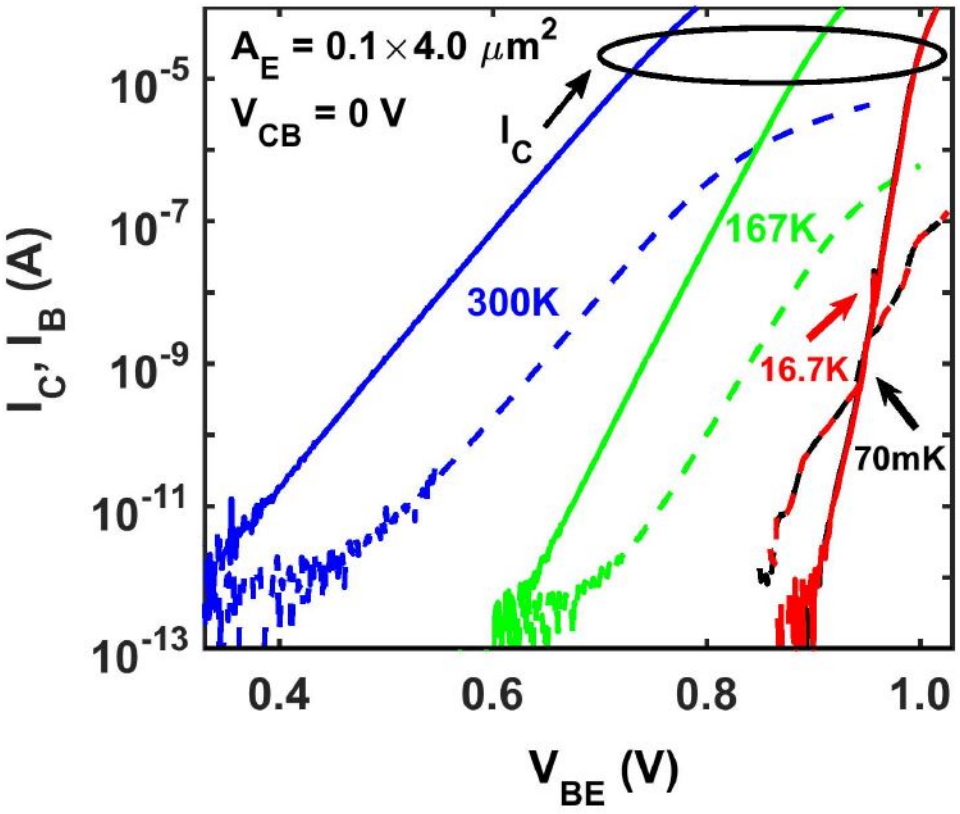

Figure 3.3: Gummel plots for Sample 1 measured in forward active mode with $V_{CB} = 0\ V$ across temperature. The solid lines are the collector current. The dashed lines are the base current. The temperature of each Gummel plot is located next to each plot. There appears to be very little difference between the plots from 16.7 K and 70 mK (from reference [127])

Figure 3.3 shows the Gummel plots of Sample 1 collected at multiple temperatures. Although noticeable by comparing each inset with its related main pane in Figure 3.2, Figure 3.3 better shows the decrease of the base current density with respect to temperature at a constant base-emitter voltage bias. This temperature dependence ultimately comes from the increased "turn-on" voltage of the base-emitter junction with decreasing temperature [20]. The turn-on voltage describes the voltage bias required to surpass a predefined amount of current through a diode leading to ambiguity in its definition. This potential inherently depends on the "built-in" voltage of the diode which describes the potential difference caused by the bending of the electronic energy bands at the PN junction. The built-in voltage of a diode is used in the boundary conditions when solving for the IV characteristics of a diode, and, ultimately, affects the saturation current. An increase in the built-in voltage leads to a decrease in the saturation current of the diode. By looking at how the built-in voltage changes with temperature, we see how the base current density of the base-emitter diode in the overall transistor is affected by a change in temperature at a constant base-emitter voltage.

The following equation defines the built-in voltage, V_{bi} of a diode [75]:

$$V_{bi} = \frac{kT}{q} \ln \left[\frac{n_n}{n_p} \right], \tag{3.5}$$

where k is the Boltzmann constant, T is the temperature, q is the elementary charge, n_n is the electron majority carrier density of the n-type part of the junction (emitter), and n_p is the electron minority carrier density of the p-type region (base) of the junction. We use a PN junction to model the base-emitter junction and assume there is a constant doping concentration of only one impurity type in each part of the junction. Using the law of mass action and charge neutrality, we find

$$n_n = N_D^+ \left(1 + \sqrt{1 + 4 \left(\frac{n_i}{N_D^+} \right)^2} \right), \tag{3.6}$$

where N_D^+ is the ionized donor concentration and n_i is the intrinsic carrier concentration, and

$$n_p = N_A^- \left(1 - \sqrt{1 + 4 \left(\frac{n_i}{N_A^-} \right)^2} \right), \tag{3.7}$$

where N_A^- is the ionized acceptor concentration. Combining Equations (3.5) to (3.7) gives

$$V_{bi} = \frac{kT}{q} \ln \left[\frac{N_D^+ \left(1 + \sqrt{1 + 4 \left(\frac{n_i}{N_D^+} \right)} \right)^2}{N_A^- \left(1 - \sqrt{1 + 4 \left(\frac{n_i}{N_A^-} \right)} \right)^2} \right]. \tag{3.8}$$

Equation (3.8) does not easily reduce to a more digestible form. In fact, even using it to calculate the built-in voltage proves difficult due to the need to find the location of the Fermi level numerically as the ionized doping concentrations and intrinsic carrier concentrations change with temperature. To make this problem tractable, we assume each part of the junction is nondegenerate, made of the same semiconductor material, that the electronic bands of the intrinsic material have a negligible dependence on temperature, and that we stay in the temperature range that allows the doping concentrations to stay significantly larger than the intrinsic carrier concentration.

Applying the law of mass action with the above assumptions, we get:

$$n_n = N_D^+ = \frac{N_D}{1 + g_D e^{(E_F - E_D)/kT}}, \tag{3.9}$$

where N_D is the donor doping concentration in the n-type material, g_D is the donor-site degeneracy factor, E_F is the Fermi level, and E_D is the donor impurity energy level. Similarly, we find for the p-type material:

$$n_p = \frac{n_i^2}{N_A^-} = \frac{n_{ip}^2 \left(1 + g_A e^{(E_A - E_F)/kT} \right)}{N_A}, \tag{3.10}$$

where N_A is the acceptor doping concentration in the p-type material, g_A is the acceptor-

site degeneracy factor, and E_A is the acceptor impurity energy level. The intrinsic carrier concentration is defined by

$$n_i^2 = N_C N_V e^{-E_G/kT}, \tag{3.11}$$

where N_C is the effective electron density of states in the conduction band, N_V is the effective electron density of states of the valence band, and E_G is the band gap. The product $N_C N_V$ also depends on temperature shown by:

$$N_C N_V = 4\left(\frac{2\pi kT}{h^2}\right)^3 (m_n^* m_p^*)^{3/2} = N_{CV}^* T^3, \tag{3.12}$$

where h is Planck's constant, $m_{n,p}^*$ are the effective masses of electrons and holes in the semiconductor, and N_{CV}^* just refers to the temperature independent portion of the the $N_C N_V$ product. Putting together Equations (3.5) and (3.9) to (3.11) gives

$$V_{bi} = \frac{kT}{q} \ln\left[\frac{N_D N_A e^{E_G/kT}}{N_{CV}^* T^3 \left(1 + g_D e^{(E_F - E_D)/kT}\right)\left(1 + g_A e^{(E_A - E_F)/kT}\right)}\right]. \tag{3.13}$$

In silicon, g_D is about 2 to account for the spin degeneracy of each donor state, and g_A is about 4 to account for the spin degeneracy of each acceptor state and the overlapping heavy hole and light hole valence bands. Above temperatures where significant freeze-out begins to occur, the exponential functions multiplied by the degeneracy factors will make those terms much less than one reducing Equation (3.13) to:

$$V_{bi} = \frac{kT}{q} \ln\left[\frac{N_D N_A}{N_{CV}^* T^3}\right] + \frac{E_G}{q}. \tag{3.14}$$

Taking the derivative of the above equation gives:

$$\frac{d(V_{bi})}{dT} = \frac{k}{q}\left(\ln\left[\frac{N_D N_A}{N_{CV}^* T^3}\right] - 3\right). \tag{3.15}$$

We find that the built-in voltage will increase with decreasing temperature when $T >$

$e(N^*_{CV})^{1/3}N_D^{-1/3}N_A^{-1/3}$, where e is Euler's number. For reference, using the effective masses in silicon at 300 K, $m^*_n = 1.18m_e$ and $m^*_p = 0.81m_e$ (m_e is the mass of a free electron) [5] and a moderate doping of 10^{16} cm^{-3} for both $N_{A,D}$, the built-in voltage should increase with decreasing temperature above 1.636 K. This value is far below the applicable temperature region (there will be significant freeze-out at this temperature), but it does show that the built-in voltage will increase with decreasing temperature in the applicable temperature range.

In the temperature range where freeze-out becomes significant but the ionized dopant concentrations remain larger than the intrinsic doping concentration, the terms including the degeneracy factors will grow much larger than one, reducing Equation (3.13) to:

$$V_{bi} = \frac{kT}{q} \ln \left[\frac{N_D N_A}{g_D g_A N^*_{CV} T^3} \right] + \frac{E_G + E_D - E_A}{q}. \tag{3.16}$$

Equation (3.16) is very similar to Equation (3.14) aside from a different constant and the degeneracy factors. Using the same parameters as above and $g_{D,A} = 2, 4$, the temperature limit increases to 3.271 K.

As temperature continues to decrease, the system will approach the intrinsic region, where the intrinsic carrier concentration is comparable to, then, surpasses the ionized dopant concentration. At this point, the model breaks down due to the initial assumptions.

This analysis does not explain why the current densities stop changing below 16.7 K as seen in Figure 3.3. Instead, as the drift-diffusion transport breaks down, or more specifically, as the tunneling transport begins to dominate the transport behavior, the current density should have less dependence on temperature than that of normal drift-diffusion transport [20].

3.5 Carrier Transport at Deep Cryogenic Temperatures

In the past, tunneling has been used to explain the temperature dependence of non-ideal base current leakage in highly-doped Si BJTs and SiGe HBTs [45]. Trap-assisted tunneling through the entire base has also been shown to attribute to collector current leakage at temperatures below 77 K in both Si BJTs and SiGe HBTs [50]. In both of these cases, tunneling is detrimental to device operation. We present a tunneling model in which the device operation at deep cryogenic temperatures is fundamentally based on electron tunneling where electrons undergo ideal tunneling through the entire base region from the emitter to the collector. The base region of the device acts as the tunneling barrier. Increasing the base-emitter voltage subsequently leads to a decrease in the tunneling barrier and an exponential increase in the collector current.

The band diagram of the GF 9HP technology platform was calculated using the Synopsys Sentaurus Technology Computer-Aided Design (TCAD) suite starting with a SiGe HBT device structure and calibrating the device doping profiles and geometries using room temperature DC and AC measurements. The current densities of the device are simulated using a hydrodynamic transport model calibrated at 300 K using the Phillips unified mobility model [54] and the Okuto-Crowell model for avalanche generation [80]. Although the calculated band diagrams are for 300 K, we expect any changes in shape across temperature to be minimal. Figure 3.4(a) shows the simulated band diagram with a base-emitter voltage of 0.8 V (black) and 0.9 V (red). The collector-base voltage is also adjusted between 0 V and 0.5 V showing a downward shift in the collector potential on the right side of the diagram when $V_{CB} = 0.5\ V$. Figure 3.4(b) gives a zoomed in view of the base portion of the band diagram showing the change of both the barrier height and width as a result of changes in V_{BE} (red and black) and V_{CB} (blue and red/black). Figure 3.4(c) shows the calibrated doping and Ge concentration profile of the device. As expected, the emitter is heavily doped n-type, the base is lower, but still heavily doped p-type, and the

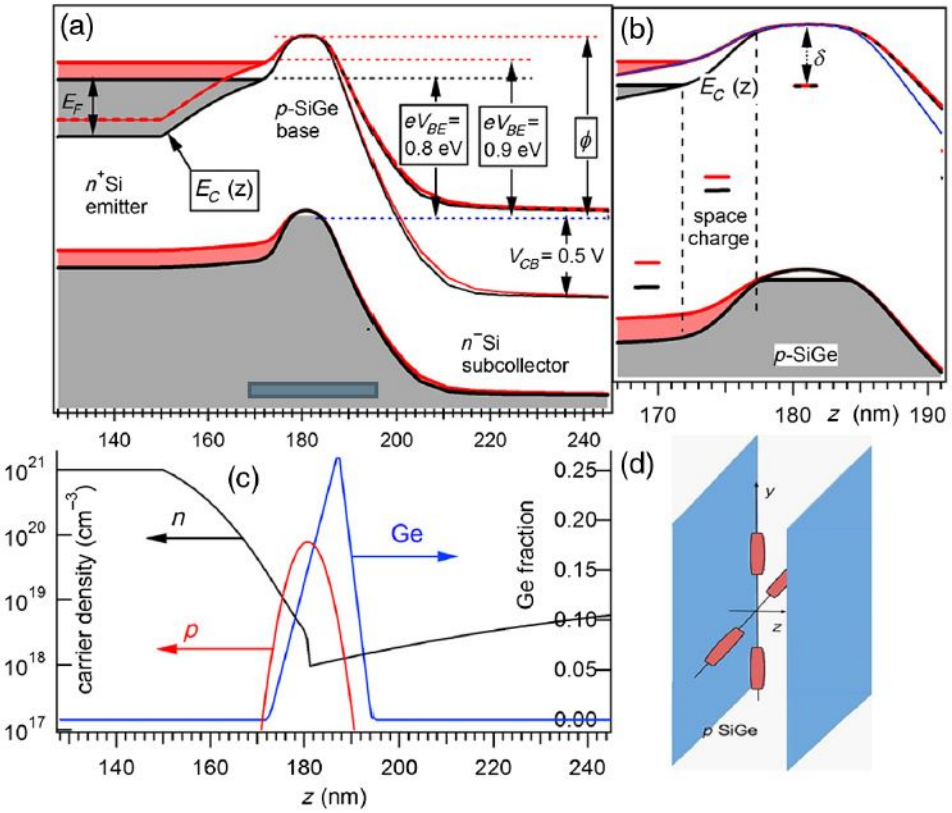

Figure 3.4: Simulated device characteristics for the GF 9HP technology platform. (a) Band diagram showing the shifting of the bands for different V_{BE} and V_{CB} values. (b) Base portion of the band diagram showing impurity traps. (c) Doping profile and Ge concentration of the device. (d) Four degenerate conduction band valleys of the SiGe base.

collector is moderately doped n-type. Defining the base region as the portion where the p-doping is larger than the n-doping, we see that the Ge concentration is graded, increasing in concentration approaching the collector, throughout the base region.

The tunneling current is based on the tunneling model by Brinkman, Dynes, and Rowell for tunneling through asymmetric tunneling barriers [12], but the specific form of the equation used is from Floyd and Walmsley in Reference [31]. The tunneling current density is given by:

$$J(V_{BE}) = \frac{4c\pi mq}{h^3} \int_0^\infty F(E_F - E_z, T) P(E_Z, V_{BE})\, dE_Z, \tag{3.17}$$

where m is the free-electron mass, c is a constant to account for the effective electron mass

of the tunneling electrons, $E_Z = \hbar^2 k_Z^2/2m$, $F(x,T) = kT\ln\left(1+e^{x/kT}\right)$, and $P(E_Z, V_{BE})$ is the tunneling probability. We find $c = 4\sqrt{ab}$, where a and b are the ratios of the longitudinal and transverse effective electron masses in the SiGe base with respect to the free-electron mass, 0.98 and 0.18, respectively. The prefactor of 4 comes from the the 4-fold degeneracy of the conduction band in the SiGe base as shown in Figure 3.4(d). k_Z is the component of the wave vector perpendicular to the tunneling barrier, ie. going from the emitter to the collector. $F(x,T)$ comes from integrating the fermi distribution about the remaining transverse wave vector components of the tunneling electrons. The tunneling probability, $P(E_Z, V_{BE})$ comes from solving the Schrodinger equation using the Wentzel-Kramers-Brillouin approximation to find the transmission coefficient of a single electron tunneling through a non-trivial potential barrier. Using the SiGe base region from Figure 3.4(a) and (b),

$$P(E_Z, V_{BE}) = e^{-2\int\sqrt{(2mb/\hbar^2)[E_C(z)-qV_{BE}+E_F-E_Z]}\,dz}, \tag{3.18}$$

where $E_C(z)$ is the bottom of the conduction band also shown in Figure 3.4(b) and Figure 3.5(a). The exponent is integrated over the region where the square root is real, and a prefactor of order unity is left out.

Figure 3.5(b) shows the current density produced from the model above at $T = 0\ K$ for the forward active mode with $V_{CB} = 0\ V$ (red), $V_{CB} = 0.5\ V$ (blue), and for the inverse mode with $V_{BE} = 0\ V$. Comparing the forward active model data to that of Figure 3.2(a), (c), and (e), we find that the current densities differ by ± 2 orders of magnitude. Although this appears large, it is to be expected considering the exponential dependence of the collector current density on the base-emitter voltage. If instead, we compare V_{BE} at different collector current densities, we find a difference of only $\pm 40\ mV$ meaning the model is within 5% of the experimental data. The inverse mode varies much more suggesting the transport is dominated by other processes. The forward active mode also has a positive

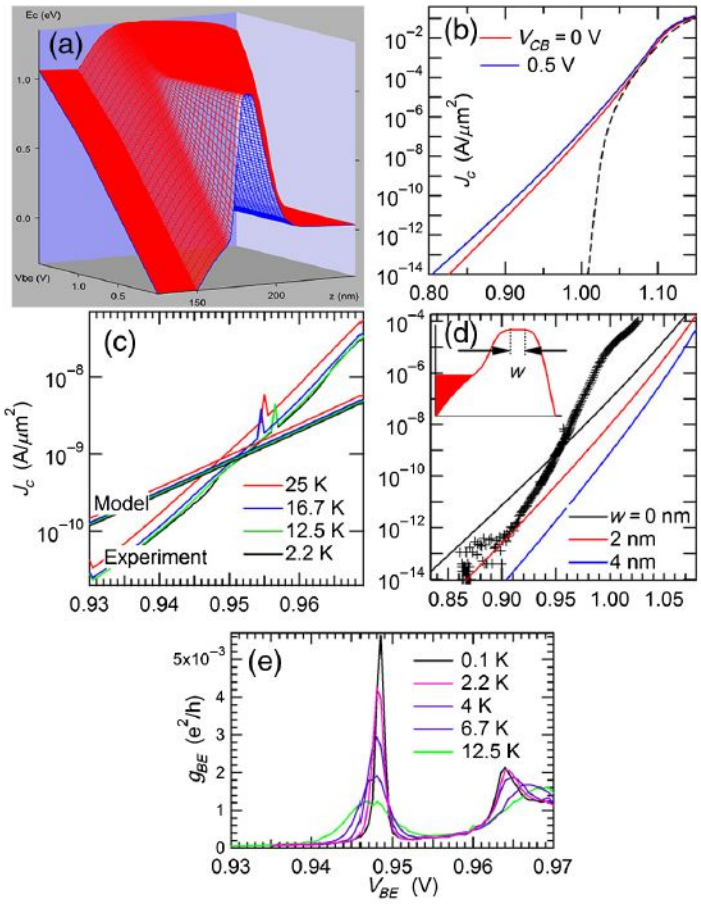

Figure 3.5: (a) Simulated bottom of the conduction band $E_C(z)$ at the tunneling barrier. (b) Current density of the ideal tunneling model at $T = 0\ K$ in the forward active mode (blue and red) and inverse mode (black). (c) Comparison of the model current density with experimental data (Sample 1) at different temperatures. (d) Changes in the current density caused by adjusting the barrier width. Black (+) are experimental data points. (e) Temperature dependence of measured base-emitter conductance density of Sample 1.

curvature below about 1 V similar to that seen in the experimental data as well. In the normal drift-diffusion transport model (as shown at 300K in Figures 3.2 and 3.3), the collector current is linear (on a semilog plot) until it reaches high-injection conditions when the curvature becomes negative.

The apparent change in temperature dependence at low temperatures seen in Figure 3.3 is also shown in Figure 3.5(c). In the tunneling model, the tunneling probability is exponentially dependent on the energy of the electrons leading to a small energy bandwidth of the tunneling electrons. The simulations show that 50% of the collector current comes from

electrons with energies just below E_F in the range of $[E_F - 10\,meV, E_F]$ in the emitter conduction band. As a result, if kT is much smaller than the energy bandwidth (corresponding to a temperature of approximately 116 K), the tunneling portion of the collector current will essentially be temperature independent. Since the transport becomes dominated by tunneling at low temperatures, this lack of temperature dependence is seen by the saturation of the collector current at 16.7 K. This saturation of the collector current could also occur from a saturation of the electron temperature leading to hot-electron transport [90].

To rule out hot-electron transport, we look at Figure 3.5(e). This figure shows the base-emitter conductance density measured in Sample 1 across temperature. The conductance peak is due to trap-assisted tunneling, but more importantly for this discussion, it shows a temperature dependence far below 16.7 K. This suggests that the electrons continue to cool far below 16.7 K even though the collector current saturates validating electron tunneling as opposed to hot-electron transport.

3.6 Conclusion

We show the operation of state-of-the-art silicon-germanium heterojunction bipolar transistors down to 70 mK. Despite the prevalence of non-ideal artifacts in the Gummel plots of each transistor, we show that the collector current of the transistors are sufficiently modeled by electron tunneling through the base of each transistor. The tunneling model gives a transconductance relationship between the base-emitter voltage and collector current and the power dissipation at measurable gain is much lower than commercial dilution refrigerators encouraging the use of this technology for cryogenic preamplification.

Above 16.7 K, we attribute the shift of the current densities in the Gummel plots to the change in the built-in voltage with respect to temperature. Below 16.7 K the current densities of the Gummel plots saturate which we attribute to the energy bandwidth of the the tunneling electrons becoming temperature independent at sufficiently low temperatures. To rule out hot electron transport as a possible cause for the current density saturation,

we compare the peaks in the base-emitter conductance density across temperature. The conductance peaks continue to increase down to 100 mK indicating that the electron temperature continues to decrease well below 16 K. The 16.7 K current density saturation also allows for researchers to prototype cryogenic premaplification circuits above dilution refrigerator temperatures with confidence of mK operation, similar to the experiment in the following chapter of this thesis.

CHAPTER 4
CRYOGENIC PREAMPLIFICATION OF MTJS

The following chapter was published in the AIP Journal of Applied Physics[22]. Slight modifications were made (grammar and word choice) to make it fit as a chapter of a thesis as opposed to a standalone article.

4.1 Introduction

Magnetic tunnel junctions (MTJs) in their simplest form consist of two ferromagnetic thin films separated by a thin insulating barrier. As electrons tunnel through the barrier, the resistance of the junction changes based on the relative angle between the magnetization of each ferromagnetic thin film [67, 101]. This effect, known as tunnel magnetoresistance (TMR) was discovered by Julliere in 1975 [51] and has found uses in data storage [68], magnetic random-access memory (MRAM) [29], and magnetic field sensors [62].

One potential issue for using MTJs for MRAM applications stems from a decrease in their signal-to-noise ratios (SNRs) as the junctions are made smaller [14]. Additionally, MRAM has been suggested as a possible solution for cryogenic memory where the low temperature allows for better thermal stability of small MTJs [2]. Even though the TMR of MTJs tends to increase with decreasing temperature, the resistance of the junctions will also increase [126] which could potentially worsen the SNR.

The noise sources in MTJs have been studied extensively over the years. The SNR of MTJs was first studied by Tondra *et al.* to optimize magnetic sensor designs [107]. More indepth studies of the low frequency noise of MTJs by Nowak *et al.* lead to evidence of two conduction channels in MTJs, spin-dependent and spin-independent currents [79]. Further studies of the low frequency noise by Ingvarsson *et al.* showed that the spin-independent noise was caused by traps in the insulating barrier while the spin-dependent noise was

caused by magnetization motion in the electrodes [47]. Doudin *et al.* had used random telegraph switching noise in Ni/NiO/Co junctions to describe the barrier traps previously but made no mention of two separate conduction currents [27]. Finally, studies by Nowak *et al.* showed that the sensitivity limit of MTJs was dependent on Johnson noise and shot noise in the junction (depending on the bias) at higher frequencies [78]. Many other researchers have looked into noise of MTJs leading up to reviews by Freitas *et al.* comparing MTJs and spin-valves for use as magnetoresistive sensors [33] and by Lei *et al.* covering the experimental evidence and theoretical backing of the noise sources in MTJs [61].

Although the technological advancement may be convincing, our motivation comes from our recent experiments [49]. In these experiments, electrons were tunneled through single Ni nanoparticles, via high resistance tunnel junctions. Signatures of magnetic dynamics within the particles were measured in real time. Improvements to the SNR in this experiment will lead to better resolution of the magnetic dynamics in nanoparticles.

Other related experiments with MTJs have focused on the switching speed [41] and switching dynamics [25]; however, in these experiments we apply cryogenic preamplification to boost the SNR of the TMR signal. Similar preamplification has been successfully implemented for qubit readout [108], charge detection with a quantum point contact [112], and single-electron transistor operation [21, 84, 113]. Multiple technologies exist that can be used for cyrogenic preamplification [87], but silicon-germanium heterojunction bipolar transitors (SiGe HBTs) have better scaling potential and process integration [19]. Furthermore, we have recently shown that SiGe HBTs operate at milliKelvin temperatures [127] and modeled their cryogenic operation [23, 128]. Even "off-the-shelf" SiGe HBTs have been used for cryogenic measurements [21] giving easy access to this advancement to any interested researchers.

The MTJ is connected directly to the base of the SiGe HBT. As the magnetization of each thin film moves, the MTJ itself changes resistance. This change in resistance is monitored at the base of the transistor and leads to a change in collector current (see Figure 4.1

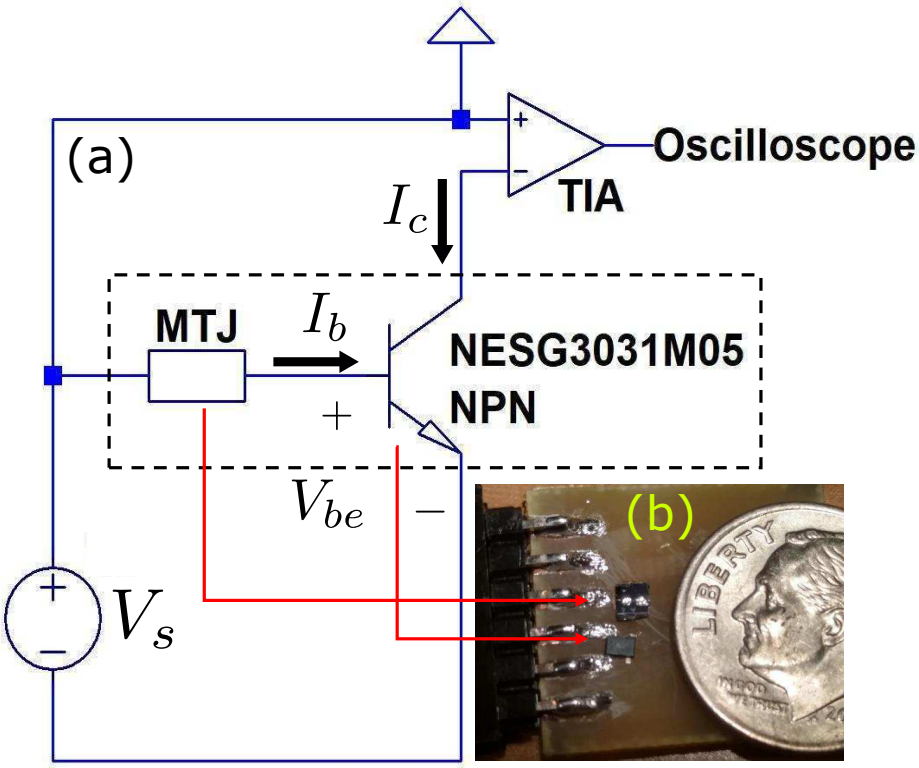

Figure 4.1: (a) The circuit used for the MTJ-SiGe HBT measurements. The dashed box is located at 8 K inside the cryostat.
(b) A picture of the MTJ and SiGe HBT mounted on the printed circuit board sample mount next to a dime for a size reference.

for details). The resulting collector current is sent to an external, room temperature transimpedance amplifier (TIA). The output of the TIA is recorded by a 1 GHz oscilloscope. The result of the experiment shows an increase in the SNR by a factor of 6.62 after adding the SiGe HBT.

The following section will describe the MTJ and SiGe HBT screening process. A noise model will be presented in Section 4.3. Finally, the results of the experiment will be presented in Section 4.4, including the increased SNR and a potential correlation between the 1/f noise and the resistance state of the MTJs. The MTJ fabrication process can be found in Section 4.7.1 and the measurement details in Section 4.7.2.

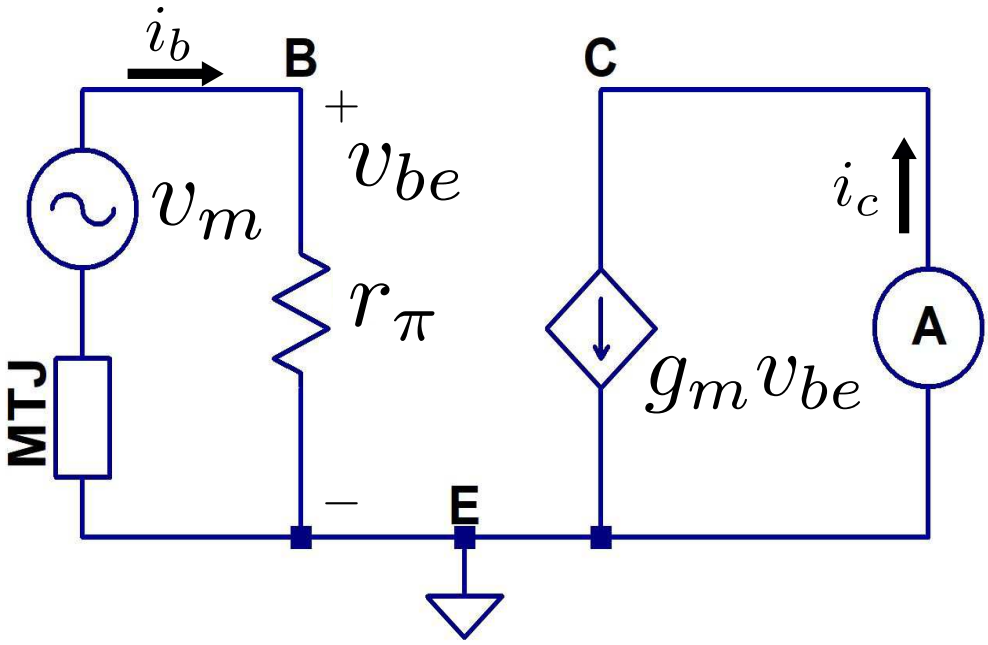

Figure 4.2: Small signal model of the transistor with the TMR modeled as a small voltage signal, V_m

4.2 Device Optimization

Optimization of the MTJs and SiGe HBTs is aimed at producing the largest output collector current signal as a response to the TMR of the MTJ at the base of the transistor. The necessary optimization parameters for both the MTJs and SiGe HBTs can be found using the small-signal, hybrid-π model. The TMR of the MTJ can be modeled as a small voltage signal, v_m, in series with the MTJ as seen in Figure 4.2. For the following analysis, the MTJ will begin in the parallel state with resistance R_{mp}.

Figure 4.1 shows that the steady state base-emitter voltage can be expressed as:

$$V_{be} = V_s - I_b R_{mp}, \tag{4.1}$$

where V_{be} is the base-emitter voltage, V_s is the source voltage, and I_b is the base current. When the MTJ changes from the parallel to antiparallel state, the resistance will increase by $\delta R_m = R_{ma} - R_{mp}$, where R_{ma} is the resistance of the MTJ in the antiparallel state.

The change in the MTJ resistance will cause the base-emitter voltage and base current to change as well leading to the expression:

$$V_{be} + \delta V_{be} = V_s - (I_b + \delta I_b)(R_{mp} + \delta R_m). \tag{4.2}$$

Equations (4.1) and (4.2) lead to an expression for the change in the base-emitter voltage:

$$v_{be} = -(I_b \delta R_m + i_b(R_{mp} + \delta R_m), \tag{4.3}$$

where the small signal parameters, $v_{be} = \delta V_{be}$ and $i_b = \delta I_b$, are used to represent the changes from the steady state. The differential base resistance is defined as $r_\pi = v_{be}/i_b$ reducing Equation (4.3) to:

$$v_{be} = \frac{v_m r_\pi}{R_{mp} + \delta R_m + r_\pi}, \tag{4.4}$$

with $v_m = -I_B \delta R_m$. The transconductance of the transistor is defined as $g_m = i_c/v_{be}$ leading to an expression for the collector current output signal:

$$i_c = g_m v_{be} = \frac{-g_m r_\pi I_b \delta R_m}{R_{mp} + \delta R_m + r_\pi}. \tag{4.5}$$

Finally, the TMR of the MTJ can be defined as:

$$TMR = \frac{R_{ma} - R_{mp}}{R_{mp}} = \frac{\delta R_m}{R_{mp}}, \tag{4.6}$$

allowing Equation (4.5) to be written as:

$$i_c = \frac{-g_m r_\pi I_b}{1 + r_\pi/R_{mp} + TMR} TMR. \tag{4.7}$$

Equation (4.7) shows that for a large output collector current signal, the transistors need

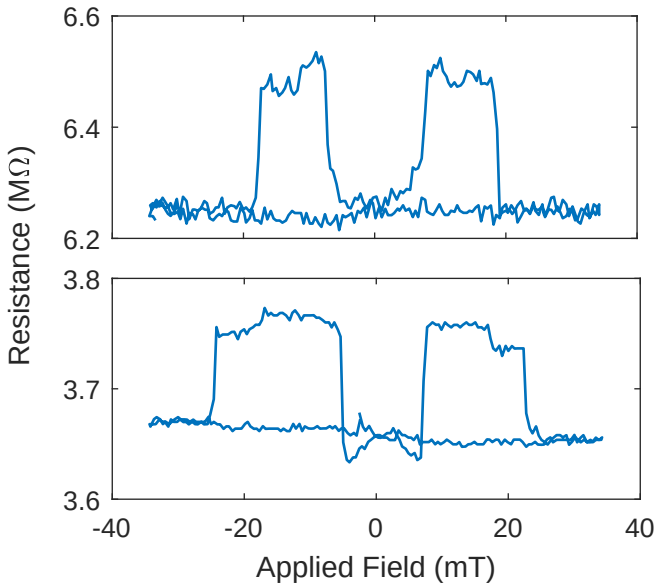

Figure 4.3: Typical field sweeps of two different MTJs. The external field was applied as a triangle wave at a frequency of 0.1 Hz. The TIA rise time was set to 30 ms, and the data was acquired at a sample rate of 30 Hz. The output of the TIA is converted back into a resistance. The top (bottom) plot corresponds to what is later labeled as Sample 2 (1).

to have a large $g_m r_\pi$ product at specific base currents, and the MTJs need to have a large resistance while still maintaining a good TMR.

The MTJs are first selected at room temperature by measuring the resistance of each junction because the TMR of these junctions is too low at room temperature to be easily resolved. Samples in the 1 MΩ range were chosen for further screening. Figure 4.3 shows the TMR at 8 K of the two MTJs discussed in this chapter.

The SiGe HBT used for this experiment is an "off-the-shelf" CEL NESG3031M05. At room temperature, these transistors are stable and show consistent operation from one device to another. When the devices are cooled to 8 K, an instability arises that has varying characteristics from device to device. The transistors are screened using their Gummel plots at 8 K as shown in Figure 4.4. The measurement details are described in Section 4.7.2.

At high bias (>1.06 V), a jump occurs in the transistor base current as seen in the top of Figure 4.4. This jump changes in height and position for each transistor. The jump is significant for two main reasons: First, due to the dimensions of the MTJs used, the

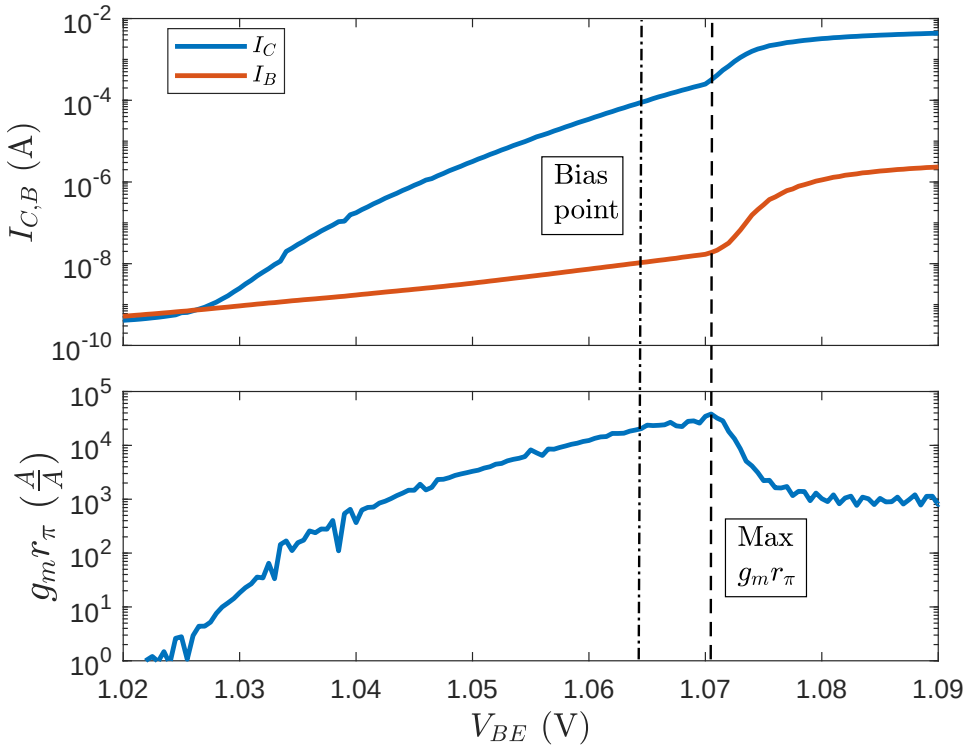

Figure 4.4: Both plots are base 10 log scale on the y-axis and linear on the x-axis.
Top: Collector and base current versus the base-emitter voltage at a constant collector-base voltage (Gummel plot with V_{CB}=0 V). A vertical dashed-dotted line shows where the transistor is biased when connected to the MTJ.
Bottom: $g_m r_\pi$ product versus the base-emitter voltage. The dashed line shows that the product falls off after the jump in the base current.

samples can only withstand about a microamp of current before breakdown. Second, the $g_m r_\pi$ product of the transistor continues to increase as the bias increases until the jump occurs. After the jump, the $g_m r_\pi$ product drops. The instability leads to the qualities of a "good" transistor as one that has the base current jump at a high bias but still has the top of the jump in the microamp range. Throughout the screening process, approximately one out of every six transistors had optimal characteristics for the experiment.

4.3 Noise Model

4.3.1 MTJ without the SiGe HBT

Before discussing the SNR in the MTJ-SiGe HBT system, we obtain the SNR of the MTJ alone to find the improvement provided by the transistor. The current spectral density of a tunnel junction, $S_{I,I}(f)$, in the low frequency approximation at low temperatures reduces to purely shot noise:

$$S_{I,I}(f) = 2qI, \tag{4.8}$$

where q is the elementary charge and I is the current through the junction [91]. The low frequency approximation is valid because qV is much larger than hf (h is the Planck constant, and f is the frequency) for the frequencies within the bandwidth of the measurement. The low temperature approximation is valid because the voltage across the junction is much larger than kT/q, where k is the Boltzmann constant and T is the temperature.

If the MTJ starts in the parallel configuration, and a constant voltage, V_{MTJ} is applied to it, an electric current of $I_m = V_{MTJ}/R_{mp}$ flows through the MTJ. The noise current spectral density in the MTJ, S_{I_m,I_m}, caused by this current flow can be calculated from Equation (4.8), while the current signal through the MTJ, i_m, due to a change in the resistance state of the junction can be expressed as:

$$i_m = \frac{-V_{MTJ}\delta R_m}{R_{mp}(R_{mp} + \delta R_m)} = -I_m\Big(\frac{TMR}{1+TMR}\Big). \tag{4.9}$$

Due to the limited bandwidth of the measurement, the observed power spectrum will roll off at high frequency. The roll off can be modeled by sending $S_{I_m,I_m}(f)$ through a parallel RC circuit and solving for the current noise variance, $(\Delta I_m)^2$, through the resistor. The result is:

$$(\Delta I_m)^2 = \frac{S_{I_m,I_m}}{4\tau_m}, \tag{4.10}$$

where τ_m is the RC time constant of the circuit. The SNR is the ratio of the signal power

and noise power. Considering both the noise current and the current signal travel through the same resistance, the SNR can be expressed as the ratio between the square of the current signal derived in Equation (4.9) and the current noise variance from Equation (4.10),

$$SNR_m = \left(\frac{2\tau_m I_m}{q}\right)\left(\frac{TMR}{1+TMR}\right)^2. \tag{4.11}$$

4.3.2 MTJ-SiGe HBT System

To derive the SNR of the MTJ-SiGe system, it is important to first establish a model to calculate the theoretical noise. Weinreb *et al.* [115] published a low frequency, low temperature noise model for SiGe HBTs, and this model will be used as a starting point for the analysis. The model includes contributions from the base and collector shot noises but ultimately disregards the base spread resistance in the transistor due to the low temperature. By assuming an optimal Johnson noise generator resistance,

$$R_{opt} = \frac{\sqrt{I_C}}{g_m\sqrt{I_B}}, \tag{4.12}$$

the noise temperature of the transistor is minimized to:

$$T_{min} = \frac{q\sqrt{I_C I_B}}{k g_m} \tag{4.13}$$

Both Equations (4.12) and (4.13) were derived by Weinreb *et al.* in the reference mentioned earlier [115].

The MTJs used in this experiment have significantly larger resistances than the calculated R_{opt} as shown in Figure 4.3 and Table 4.1, so the original model needs to be adjusted to Figure 4.5. The differential base resistance, r_π, cannot be ignored because r_π is parallel to the MTJ. As the MTJ resistance surpasses that of r_π, the noise current becomes shunted by r_π. The result is a smaller than expected noise voltage at the base leading to a smaller than expected noise current contribution at the collector output.

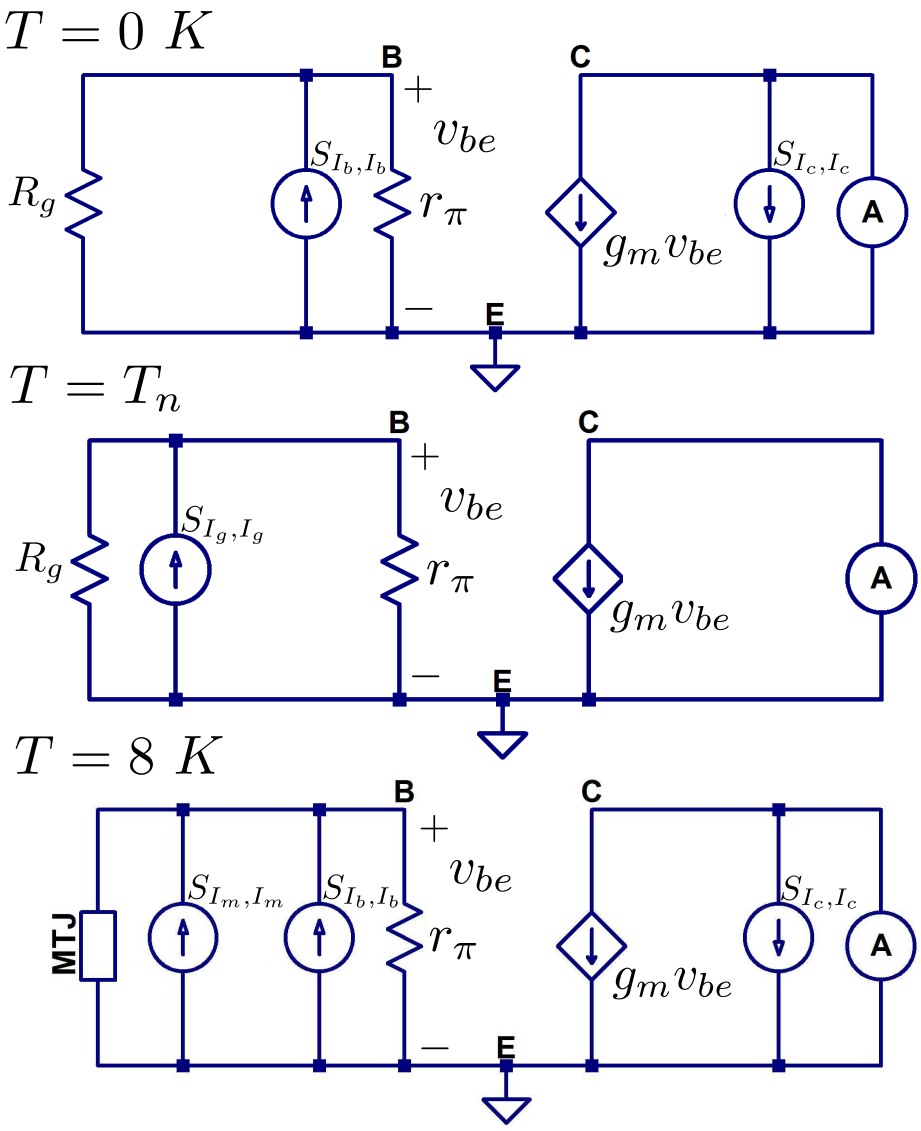

Figure 4.5: Top and Middle: Adjusted noise model to calculate the effective noise temperature of the transistor. The noise generated by the transistor connected to a noiseless ($T = 0\ K$) resistor is equated to the noise generated by a resistor ($T = T_n$) connected to a noiseless transistor to solve for the effective temperature of the transistor (T_n).
Bottom: Adjusted noise model to calculate the total noise of the system. The generator resistance is replaced by the MTJ and all of the noise sources are combined ($T = 8\ K$).

Still holding to the same assumption, that the base spread resistance is negligible at these temperatures, and, additionally, accounting for r_π, the new noise temperature can be found. The noise sources of the transistor connected to a noiseless resistor (top of Figure 4.5) are combined and equated to the noise produced by a noisy resistor connected to a noiseless transistor (middle of Figure 4.5). The temperature of the generator resistor,

R_g, is the effective noise temperature of the transistor.

Both the noise current spectral density of the base, S_{I_b,I_b}, and collector, S_{I_c,I_c}, are purely shot noise given by Equation (4.8). As seen in the top of Figure 4.5, S_{I_b,I_b} can be referred to the collector side of the transistor. The current spectral density has units of A^2/Hz, so the transfer function to refer the base current to the collector must be squared when referring the current spectral density from the base to the collector. Next, the collector noise contribution, S_{I_c,I_c}, is added to the base noise contribution. Moving to the middle of Figure 4.5, the current spectral density from the Johnson noise, $S_{I_g,I_g} = 4kT_n/R_g$, of the generator resistor, R_g, is referred to the collector side of the transistor as well. Equating the two noise contributions from the top and middle of Figure 4.5 allows us to solve for the effective noise temperature of the transistor, T_n.

The previously described process gives the equation:

$$S_{I_g,I_g}\left(\frac{g_m R_g r_\pi}{R_g + r_\pi}\right)^2 = S_{I_b,I_b}\left(\frac{g_m R_g r_\pi}{R_g + r_\pi}\right)^2 + S_{I_c,I_c}, \tag{4.14}$$

where the left and right sides of the equation come from the middle and top of Figure 4.5, respectively. Equation (4.14) can be rearranged after substituting in the formulas for the current spectral densities to solve for the effective noise temperature of the transistor using the adjusted model:

$$T_n = \frac{qR_g}{2k}\left[I_b + I_c\left(\frac{R_g + r_\pi}{R_g r_\pi g_m}\right)^2\right], \tag{4.15}$$

where R_g is equivalent to the resistance of the MTJ.

The total noise of the system, $S_{I_t I_t}(f)$, can be found using the same, adjusted model by replacing the generator resistance with the MTJ (bottom of Figure 4.5) and following a similar process. Both the noise contribution from the MTJ, S_{I_m,I_m}, and the base, S_{I_b,I_b}, need to be referred to the collector. Then, all of the noise contributions are combined

giving:

$$\begin{aligned} S_{I_t,I_t}(f) &= \Big(S_{I_m,I_m} + S_{I_b,I_b}\Big)\Big(\frac{g_m R_{mp} r_\pi}{R_{mp}+r_\pi}\Big)^2 + S_{I_c,I_c} \\ &= 2q\left[2I_b\left(\frac{g_m R_{mp} r_\pi}{R_{mp}+r_\pi}\right)^2 + I_c\right], \end{aligned} \tag{4.16}$$

where $I_m = I_B$ in this case (see Figure 4.1), and the MTJ is in the parallel state.

Similarly to Equation (4.10), the variance of the total noise current at the collector, $(\Delta I_t)^2$, can also be calculated,

$$(\Delta I_t)^2 = \frac{S_{I_t,I_t}}{4\tau_t}. \tag{4.17}$$

In the MTJ-SiGe HBT system, the hybrid-π model is only valid when δR_m is sufficiently smaller than r_π. Also, Equation (4.7) shows that a high MTJ resistance is beneficial. These two conditions and Equations (4.7) and (4.17) lead to the following SNR for the MTJ-SiGe HBT system:

$$SNR_t = \left(\frac{2\tau_t}{q}\right)\frac{(g_m r_\pi R_{mp} I_b)^2 (TMR)^2}{2I_b(g_m R_{mp} r_\pi)^2 + I_c(R_{mp}+r_\pi)^2}. \tag{4.18}$$

The following ratio of Eqs. 4.11 and 4.18 gives a good comparison between the MTJ by itself and the MTJ-SiGe HBT system:

$$\frac{SNR_t}{SNR_m} = \frac{\tau_t}{\tau_m}\left[2 + \frac{I_c}{I_b}\left(\frac{R_{mp}+r_\pi}{g_m r_\pi R_{mp}}\right)^2\right]^{-1}(1+TMR)^2, \tag{4.19}$$

where it is assumed that $I_m = I_b$. The two previous conditions also require the TMR to be less than 1. As a result Equation (4.19) shows that adding an amplifier decreases the SNR of the measurement (the ratio is less than 1), which should be expected [16]. Furthermore, if we assume a constant I_b (by adjusting V_{MTJ} to maintain a constant I_m) as the MTJ resistance decreases, the ratio does as well. On the other hand, as the MTJ resistance approaches infinity, the ratio approaches a maximum. A similar relation can be seen for Equation (4.18). This suggests a benefit for using higher resistance MTJs as long

Table 4.1: Minimum noise temperature calculated at specific Gummel points around the biasing seen in Figure 4.6 using Eqs. 4.12 and 4.13.

I_c (μA)	I_b (nA)	g_m (mS)	R_{opt} (Ω)	T_{min} (K)
72.86	9.85	14.74	5834	0.6670
80.02	10.23	16.26	5442	0.6457
89.05	10.69	17.29	5278	0.6546
97.69	11.07	20.42	4600	0.5910

as the necessary voltage bias across the MTJ can be maintained.

4.4 Results and Discussion

The results to be discussed will begin with a comparison of the noise temperature of the transistor which will lead into a verification of the adjusted model. After the verification, the SNR is presented and discrepancies with the theory are discussed. To finish, another effect seen in the noise spectrum is presented.

Table 4.1, shows specific Gummel points around the biasing from Figure 4.6 and the resulting optimal Johnson generator resistance and minimum noise temperature. Although, the model had to be adjusted for the high resistance MTJ, the table still provides good data about the transistor for other low temperature uses.

To solve for the noise temperature using the adjusted model, the MTJ resistance needs to be known. Due to the non-ohmic nature of the MTJ, its resistance is calculated at the bias conditions by comparing the applied voltage, 1.099 V, with the Gummel characteristics of the transistor. Table 4.2 shows the same Gummel points as Table 4.1, but includes the necessary MTJ resistance and r_π needed to maintain the associated bias conditions.

It can be seen from Tables 4.1 and 4.2 that the noise temperature of the transistor is highly dependent on the source resistance. The noise temperatures from Table 4.1 are all much smaller than those from Table 4.2 due to the significant difference in R_{opt} and the parallel combination of R_m and r_π. The noise temperature also decreases with higher biasing in Table 4.2 due to the decreasing differential base resistance and MTJ resistance

with increasing voltage bias.

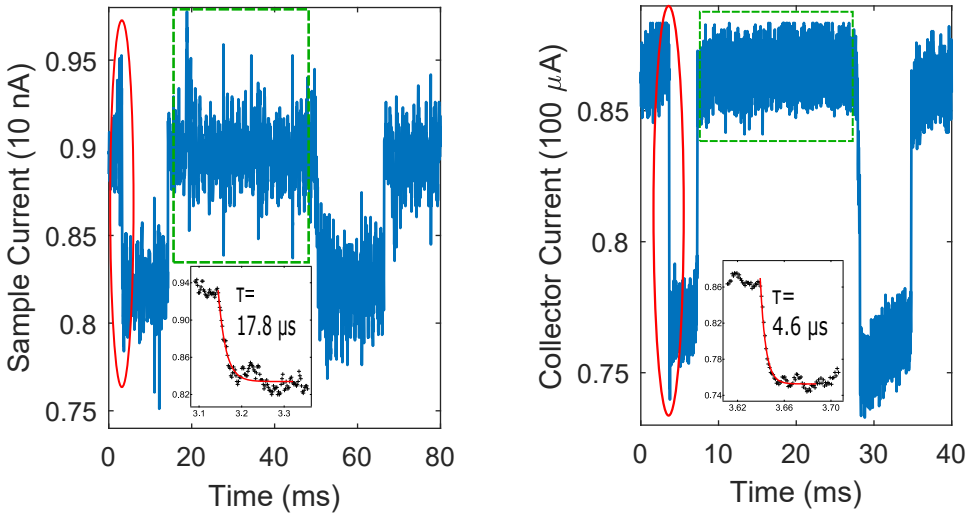

Figure 4.6: A current vs time plot of a broadband, single-shot field sweep of Sample 1 without(with) the transistor is on the left(right). The left(right) plot was taken with a field sweep rate of 10 Hz(20 Hz). The insets show data point markers and exponential fits of the first transition of each plot (in solid red ellipses) as well as the extracted time constant for each. As seen in Table 4.1, the MTJ has approximately the same bias in both situations. The inclusion of the SiGe HBT decreases the time constant of the measurement and increases the SNR

Figure 4.6 contains plots of single-shot, broadband measurements of the MTJ's magnetic field response by itself (left) and connected to the SiGe HBT (right). Since resistance is a passive parameter, the plots show the current through the MTJ with a constant voltage bias on the left, and the collector current of the SiGe HBT with the MTJ connected to its base (also with a constant voltage bias) on the right. As seen in Table 4.1, the biasing of the MTJ in both situations is approximately the same. Obtaining the broadband measure-

Table 4.2: Noise temperature calculated at specific Gummel points around the biasing seen in Figure 4.6 using Equation (4.15). The noise temperatures are much higher due to the larger source resistance.

I_c (μA)	R_m (MΩ)	r_π (MΩ)	T_n (K)
72.86	3.603	1.245	206
80.02	3.423	1.186	203
89.05	3.228	1.184	200
97.69	3.070	1.162	197

ment of the MTJ without the SiGe HBT proved difficult due to the small currents and large noise, so only Sample 1 had a large enough TMR to see a good signal. The first transition of each plot (in red ellipses) was fitted to an exponential, and the resulting time constants and zoomed in views of the transitions with the fits are shown in the insets of the figure. These time constants are equivalent to those used in Equations (4.10) and (4.17). As seen in the figure, τ_m is 17.8 μs and τ_t is 4.57 μs. The decreased time constant shows that a better measurement time resolution can be obtained by adding the cryogenic preamplification.

To verify the model used, it is best to look at the measured noise current spectral density and compare it to the calculated value. Using 70 single-shot measurements similar to Figure 4.6, the average current power spectral density was found for the regions in the green dashed box, as well as the two high resistance (low current) regions on either side of this region. The transitions are left out to get a good indicator of only the noise in each state. The average RMS of all 70 traces for the region in the green box came out to be 92.6 μA, so the calculated theoretical noise used the closest Gummel points above and below the bias point. Figure 4.7 shows the noise approaching the theoretical limit when including r_π before it rolls off. If r_π is ignored, the measured noise drops far below the theoretical noise limit before the roll off, which is a good indicator that the adjusted model is necessary. Furthermore, the roll off can be seen in the same area as predicted, $1/(4\tau_t)$, or about 55 kHz.

The SNR is calculated using the ratio of the signal variance and the noise variance from Figure 4.6. The noise standard deviation is calculated by only looking at the part of each signal in the green dashed boxes of Figure 4.6, while the signal standard deviation was taken over the entire field sweep. For the MTJ by itself, the signal standard deviation is 0.366 nA, the noise standard deviation is 0.144 nA, and SNR_m is 6.48. For the MTJ-SiGe system, the signal standard deviation is 4.10 μA, the noise standard deviation is 626 nA, and SNR_t is 42.9. Comparing the SNR from before and after cryogenic preamplification, shows an increase by a factor of 6.62. This way of calculating the SNR provides a rough

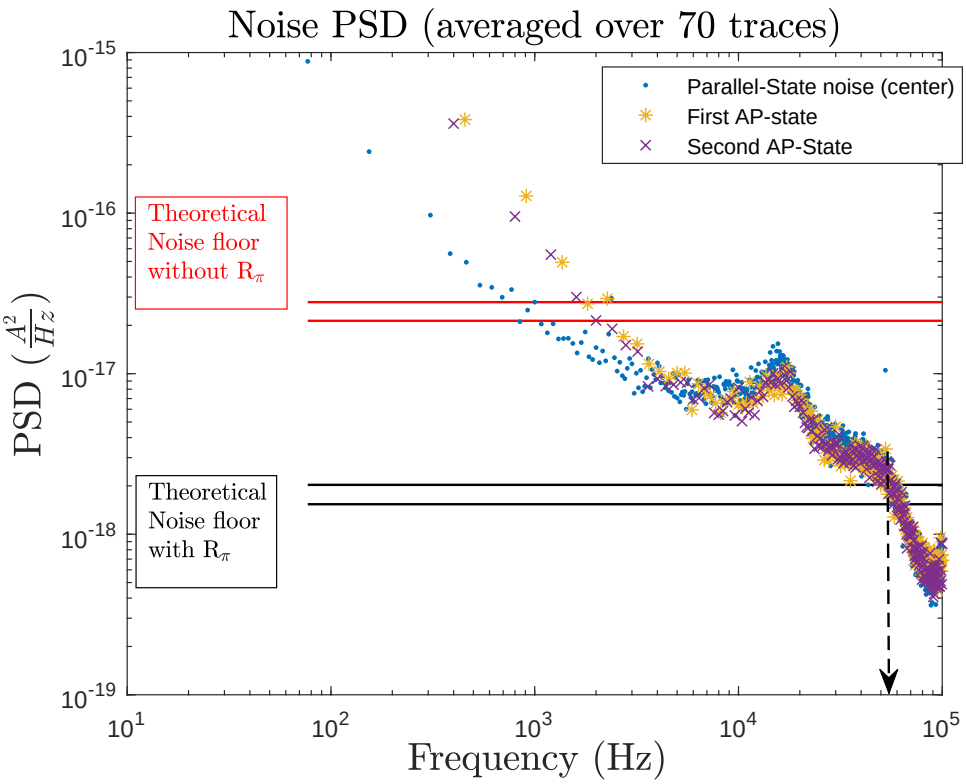

Figure 4.7: The averaged current spectral density of 70 different single-shot measurements of the MTJ-SiGe system using Sample 1 are plotted above. The calculated noise floor (horizontal lines) used the next closest (higher and lower) Gummel points to the average RMS value of all of the traces, 92.6 μA, with and without r_π to check the validity of the modified model. The arrow shows approximately where the noise spectrum rolls off. The dots are the section of the traces in the green dashed box from the left side of Figure 4.6, the * and X are the high resistance (low current) states on either side of this region. There is a significant difference between the 1/f noise contribution in the parallel and anti-parallel states of the MTJ

estimate due to the signal variance depending on the stochastic nature of the MTJ switching; however, it is a better representation than the parameter approach considering the 1/f noise was ignored in Equations (4.11) and (4.18).

As stated previously at the end of Section 4.3, the ratio of the two SNRs should be less than 1. Instead an increase in the SNR is seen. This increase in SNR shows the importance of cryogenic preamplification. By amplifying the signal before it exits the cryostat, any noise added by the room temperature electronics is added to the amplified signal instead of the much smaller source signal. The result is an increase in the SNR that could not be

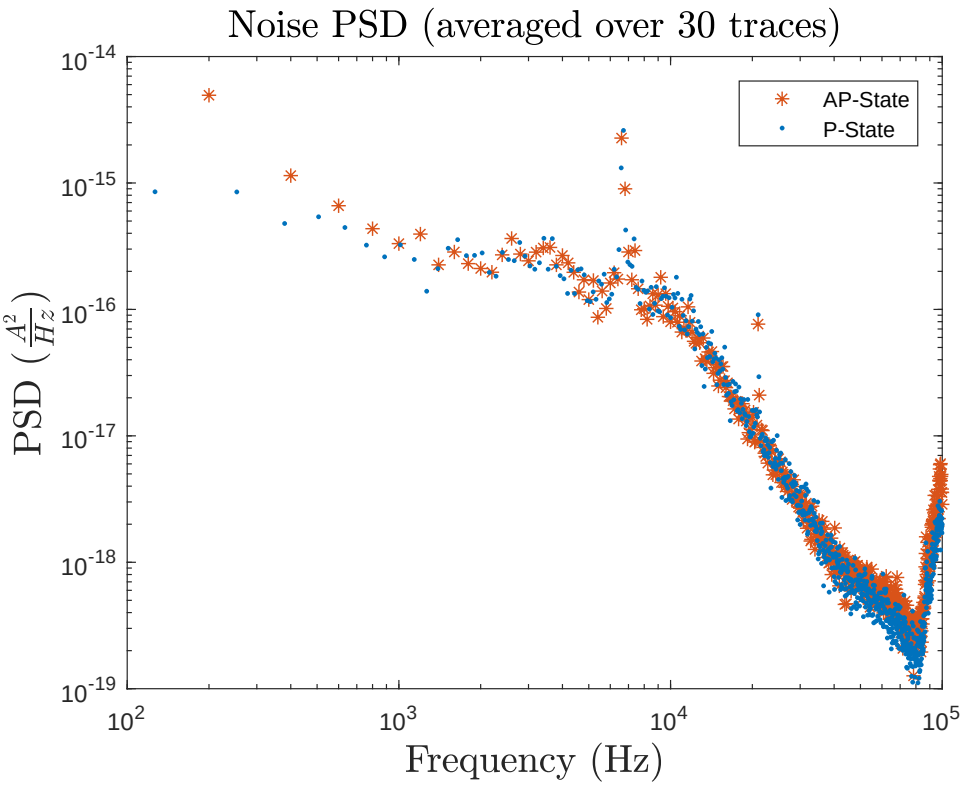

Figure 4.8: The current power spectral density of 30 different single-shot measurements of the MTJ-SiGe system using Sample 2 were averaged. The dots correspond to the noise in the parallel state (high current, low resistance), while the solid line corresponds to the noise in the antiparallel state (low current, high resistance).

acquired without the cryogenic preamplification.

Although the modified model accounts for the change in theoretical noise floor, it does not account for other effects seen in Figure 4.7. The first effect is the difference in the 1/f noise contribution for the parallel and antiparallel states of the MTJ. The second, is the peak that occurs around 20 kHz. To verify whether or not these effects are anomalies, the same average current power spectral density was calculated for a MTJ-SiGe HBT system including Sample 2.

Looking at both Figs. 4.7 and 4.8, it appears that the 1/f noise increases in the antiparallel state. It has been previously shown that increasing the base current of a SiGe HBT should lead to an increased 1/f noise[77]. Considering the antiparallel state of the MTJ relates to a high resistance state and a lower base current, the increase in 1/f noise must

be intrinsic to the MTJ state and not the SiGe HBT. A similar effect was shown using a normalized 1/f noise parameter by Nowak *et al.* [78] and further discussed using Hooge parameters in the review by Lei *et al.* [61]. The peak, however, changes shape and shifts in frequency, suggesting that it is due to an external noise source or some resonance within the system itself.

4.5 Conclusion

A solution for increasing the SNR of the TMR signal of high resistance MTJs at 8 K has been proposed and tested encouraging further research into MTJ based cryogenic memory and providing a possible advancement for other cryogenic tunneling measurements. Starting from a proposed noise model, the SNR of the MTJ and MTJ-SiGe HBT system has been derived. A previously used noise model was adjusted for this system and tested showing a vast improvement in relation to the data. The minimum noise temperature of the SiGe HBT is calculated and compared with the actual noise temperature of the SiGe HBT in the experimental setup. The SNR of the system increases asymptotically with increasing MTJ resistance while the noise temperature of the amplifier has a roughly, linear increase after the MTJ resistance surpasses the optimal resistance for minimum noise. From a noise analysis of the experimental data a relationship between the 1/f noise and the state of the MTJ has also been observed.

4.6 Acknowledgments

The work in this chapter could not have been completed without the experimental assistance provided by M. Mourigal and L. Ge in previous experiments directly related to this work.

The research in this chapter was supported in part (J. Dark, G. Nunn, and D. Davidović) by DOE contract DE-FG02-06ER46281, and (H. Ying and J. D. Cressler) by the Laboratory Directed Research and Development (LDRD) Program at Sandia National Laboratories (operated by NTES of Sandia, a wholly owned subsidiary of Honeywell International Inc.,

for DOE's NNSA under contract DE-NA-0003525).

4.7 Appendices

4.7.1 Appendix A: MTJ Fabrication

The fabrication of the MTJs begins with a 100 mm silicon wafer coated with a dry oxide. After the wafer is cleaned with acetone and isopropyl alcohol (IPA), it is then spin-coated with a layer of MMA followed by a layer of PMMA to create a bilayer electron beam resist. Pieces of the wafer are broken off for fabrication of arrays of twenty-four MTJs. Each separate chip is etched by electron beam lithography using a JEOL JSM-5910 Scanning Electron Microscope. Development is performed by vigorously stirring the sample in a 3:1 mixture of IPA and methyl isobutyl ketone (MIBK) for 60 seconds. Developing the bilayer electron beam resist forms a PMMA bridge over an empty cavity, on the silicon dioxide surface. This cavity allows for the stacking of materials by a process known as shadow evaporation deposition. The chip is then placed in a vacuum chamber and pumped down to 2.67E-5 Pa (2E-7 Torr) before deposition. Shadow evaporation deposition is performed using thermally heated materials and an Inficon Deposition Monitor to verify deposition rates with angstrom-level precision.

For shadow evaporation deposition, the stage is first tilted to form a 15° angle between the normal of the sample stage and the z-axis. The z-axis in this case extends from the evaporation source to the center of the sample stage as seen in Fig 4.9. At this angle, 100 Å of permalloy (Ni80/Fe20) is deposited. Next, the stage is tilted in the opposite direction making another 15° angle between the normal of the sample stage and the z-axis. The 35 Å insulating barrier of alumina is deposited by evaporating aluminum at a rate of 2.5 Å/s and releasing oxygen gas at the same time near the sample stage at a rate of 200 cm^3/min. This process forms alumina on the permalloy and silicon dioxide surfaces as the aluminum deposits. After the alumina, another 100 Å of permalloy is deposited to finish the MTJ fabrication.

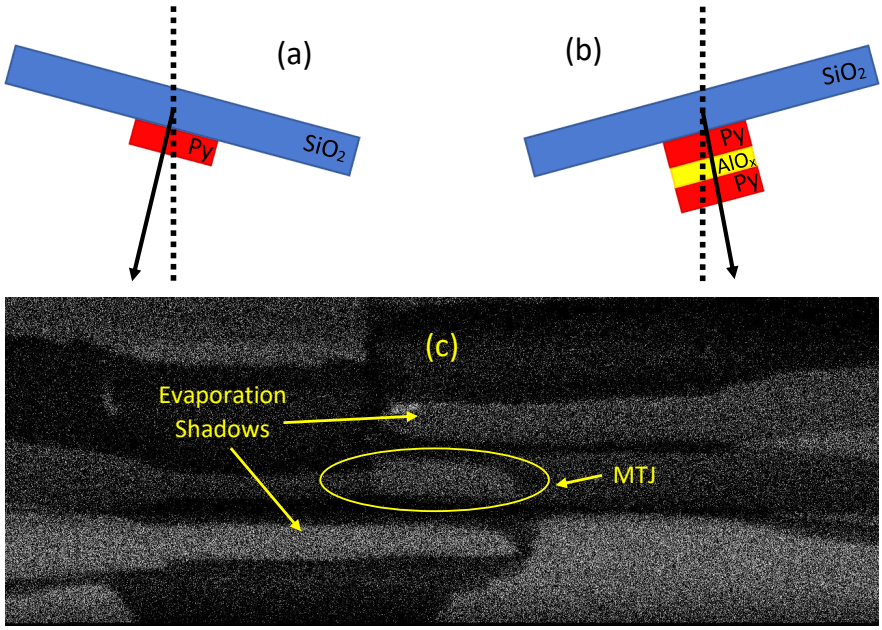

Figure 4.9: (a) and (b) show the sample fabrication process (not to scale). The dotted line is the z-axis and extends down to the evaporation source. The PMMA bridge (not shown) and rotation of the sample platform allow for stacking of the materials to form the junction while simultaneously creating leads with connections to each permalloy layer. (c) is an SEM image of a junction made with chromium and gold with no oxide for imaging purposes only. The junction is in the center, and the two evaporation shadows are results of the process.

Because the junction fabricated uses the same ferromagnetic material for each thin film, the width of each film was adjusted to ensure that the films in each junction have different switching fields. By having different switching fields, the magnetization of each film will flip at different fields giving the MTJs well-defined parallel and antiparallel states. Both layers have the same thickness as stated previously, but the bottom layer has a width of 300 nm and the top layer, 150 nm. The overlap of the two thin films forming the MTJ is 1 μm.

4.7.2 Appendix B: Experimental Setup

The MTJs are cooled in a CTI Model 22 Cryodyne Refrigerator. The external field is produced by a homemade superconducting solenoid mounted inside the cryostat. Using

the geometry and winding density of the solenoid, the applied field per ampere of sourced current was calculated to be 27.7 mT/A. A Stanford Research Systems DS335 Function Generator produces a triangle wave that is fed into a Kepco BOP 20-20M power amplifier. The amplifier powers the solenoid to produce a magnetic field along the easy axes of the MTJs. The frequency of the triangle wave is set to 0.1 Hz, and the amplitude is adjusted so that the magnetic field amplitude is between 30 mT - 50 mT depending on the field needed to change the sample from the parallel to antiparallel then back to the parallel state. A constant voltage is supplied to the MTJs, and the current through the junction is monitored with an Ithaco Model 1211 TIA. The TIA rise time is set to 30 ms to filter out high frequency noise. The voltage output of the TIA is recorded using a NI BNC-2120 Data Acquisition Board and LabView at a sample rate of 30 Hz to avoid oversampling. Typical results of a field sweep on a good sample with the voltage output converted back to a resistance can be seen in Fig 4.3.

The transistors are also cooled in the cryostat. The base and collector currents are measured with the TIA as the supply voltage is swept with a Stanford Research Systems DS345 Function Generator. The base and collector are both biased at the same voltage during the measurements allowing for the creation of a Gummel plot as seen in Fig 4.4.

Two other models of "off-the-shelf" SiGe HBT devices were also screened for possible use. These included the Infineon BFP720 and the NXP BFU710F. Both of these transistors operated at 8 K; however, both also had the same issue with the jump in the base current. In the end, the NESG was chosen for its higher $g_m r_\pi$ product right before the base current jump.

The MTJ-SiGe HBT system is formed by mounting the SiGe HBT and MTJ onto a printed circuit board (PCB) and connecting the base of the transistor directly to one of the MTJ leads. The base of the transistor is located as physically close to the MTJ as possible to reduce the input parasitic capacitance at the transistor base (see Fig. 4.1). Indium is used to bond small copper wires to connect the sample, transistor, and the PCB sample mount. The

PCB is mounted inside the crysotat and connected to phosphor-bronze wires that exit the cryostat through a Fischer Connector. The wires are about 1 m long, and twisted together to reduce the effect of externally induced electrical noise. The entire system is cooled to 8 K, and the current of the base and collector are each measured using a constant voltage bias across the collector and the MTJ-base connection. The same field sweep described previously is performed. If an appreciable signal is seen, the TIA is connected to the collector, and the rise time is set to the minimum setting. The TIA output is sent directly to a Lecroy 9370 1 GHz Oscilloscope as shown in Fig. 4.1, and the frequency of the field sweep is increased to allow for better time resolution of the measurement.

CHAPTER 5

TERBIUM-DOPED DOUBLE MAGNETIC TUNNEL JUNCTIONS

5.1 Introduction

The ability to create and stabilize measurable entangled states is critical to the development of future quantum applications. The necessity of introducing a quantum state to its environment for setting and measurement means that quantum decoherence is a major hurdle to establishing new quantum computing and quantum sensing technologies. When the quantum state interacts with its surrounding environment, it begins to decohere. The decoherence greatly reduces the available time to interact with the state for computing or sensing purposes. Counterintuitively, the intentional design of a quantum system that is strongly coupled to its environment has been proposed as a means to manage decoherence [111]. By adjusting the dissipation to the environment, a quantum system essentially relaxes into the desired quantum state as its steady-state condition. This process allows for state preparation that is inherently protected from the normal decoherence caused by the environment. Furthermore, the dissipation process can be engineered to perform quantum calculations where the solution is, once again, a steady-state condition of the system. This means that self-protecting quantum systems can be designed by controlling the coupling of a quantum system to its environment. Initial work demonstrates that this is a viable route to maintaining entangled states in trapped-ion and superconducting qubit systems [63]. The successful experimental implementations of using controlled environmental coupling opens the door to an interesting question: what other quantum systems would allow for such strong coupling and, ultimately, new state preparation and computation approaches useful to developing quantum technologies?

Recent experiments have shown that adding rare earth element (RE) doping to permal-

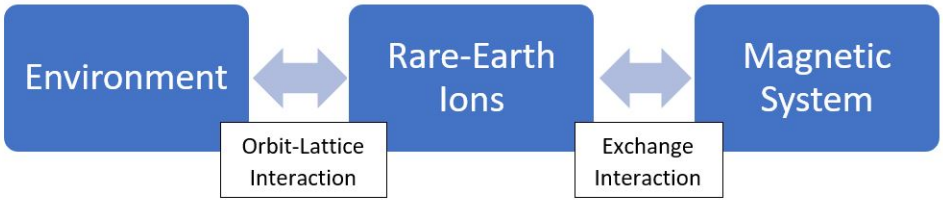

Figure 5.1: Qualitative view of the interactions that lead to stronger, adjustable coupling between the environment and the spin system.

loy ($(Ni_{0.81}Fe_{0.19})_{100-X}RE_X$) thin films tailors the magnetic properties of the films[4, 89]. Adding a terbium doping of only 2% increases the Gilbert damping parameter of the permalloy by an order of magnitude. The damping parameter also increases with decreasing temperature, which indicates a dynamical coupling between the magnetic system and its environment. Doping the permalloy films with gadolinium as opposed to terbium does not increase the magnetic damping parameter at RE concentrations below 15%[4]. The terbium magnetic moment includes both a spin and orbital contribution, while the gadolinium magnetic moment includes no orbital contribution. The increased magnetic damping with decreasing temperature in the terbium-doped permalloy films indicates a stronger environmental coupling of the orbital magnetic moment in terbium as opposed to that of the purely spin magnetic moment in gadolinium. The increased coupling of the magnetic system in the terbium-doped permalloy films can be viewed as a series of interactions within the system. Orbital-lattice interactions lead to stronger coupling of the terbium ions to the environment. The exchange interaction couples the permalloy and terbium electrons, and, as a result, increases the environemtal coupling of the entire magnetic system. Figure 5.1 gives a qualitative representation of these interactions. This controllable coupling by adjusting the terbium content in permalloy may allow for the study of quantum state dynamics using the intrinsic underlying spin system similarly to the trapped ion and superconducting systems mentioned above.

As a first step, we look to better understand the electronic coupling to the environment in the terbium-doped permalloy system. By fabricating a double magnetic tunnel junction

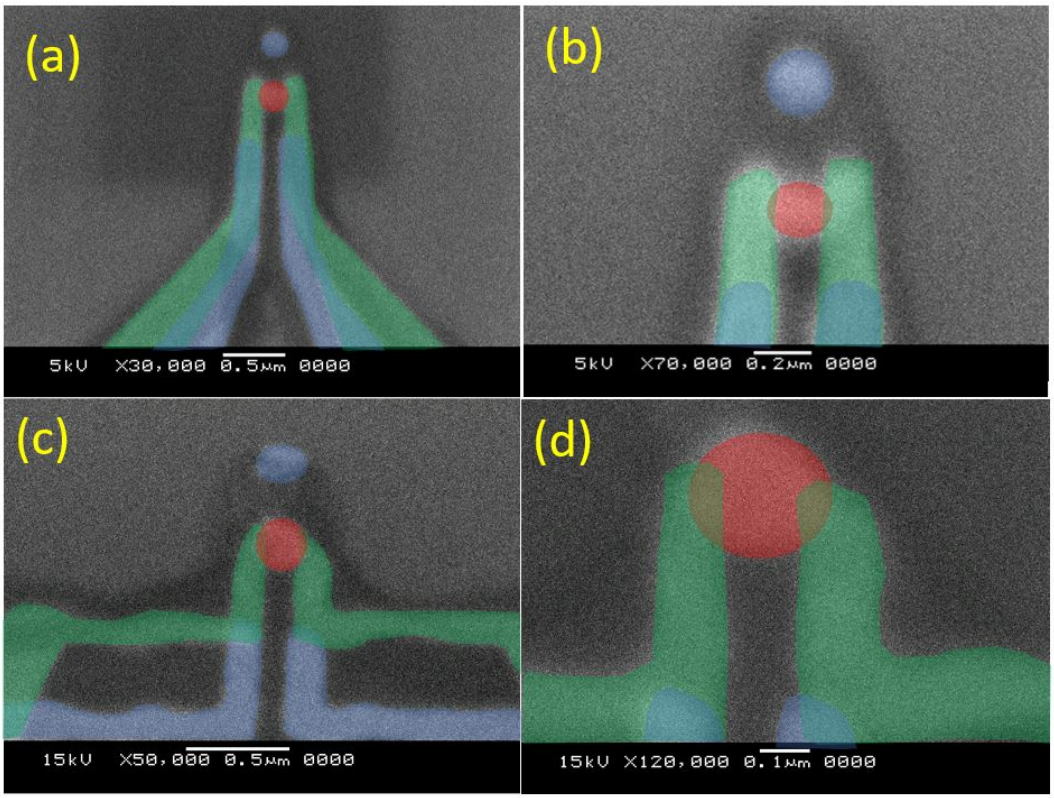

Figure 5.2: SEM images of the two different DMTJ designs using Cr-Au for better image quality. Color overlays emphasize the parts of each design, with green for the device leads, blue for the evaporation shadows, and red for the central particle. The lead widths are less than 200 nm and the particle radius is approximately 100 nm. (a)SEM image showing the leads and particle of the first device design (D1). (b)Larger magnification of D1. (c)SEM image of second device design (D2). (d)Larger magnification of D2.

(DMTJ) that includes a central nanoparticle made from the terbium-doped permalloy, we can probe the terbium-doped permalloy system by tunneling electrons through the central particle. Additionally, by fabricating an identical DMTJ with no terbium-doping in the central particle, we can gather a baseline for the undoped system. Comparing the electron transport in both devices isolates any effects directly related to the terbium-doping of the central nanoparticle. The results of these experiments helps to lay the groundwork for future studies of large spin systems with strong environmental coupling.

5.2 Sample Fabrication

Fabrication of the DMTJs follows similarly to that of the MTJs in Section 4.7.1. The main difference comes from the need for a central nanoparticle (see Figure 5.2). After adjusting the lithography pattern, we also changed the angle of rotation for the shadow evaporation. By putting the rotation axis perpendicular to the leads, the particle deposits between the leads and creates a shadow above the leads. Figure 5.2 shows SEM images of the final devices using Cr-Au for better image quality. The colored overlays show different aspects of the layering: green for the device leads, red for the device particle, and blue for the evaporation shadows. We changed the DMTJ device design (Figure 5.2 (c) and (d)) after the first measurements because we noticed the SEM would occasionally short the pattern near the center of Figure 5.2 (a). We believed this was due to the higher dose applied at the point when the leads first approach their minimum separation distance.

In both sample designs, the red particle and blue leads are deposited first with 5 nm of either permalloy ($Ni_{0.8}Fe_{0.2}$) or permalloy with 4% terbium doping ($Ni_{0.8}Fe_{0.16}Tb_{0.04}$). Next, we deposit the alumina. In the first design, we rotate the stage and deposit 4 nm of alumina at the locations of the blue particle and green leads. In the second design, we deposit 2 nm of alumina before rotating the sample stage, and another 2 nm of alumina rotating the sample stage. Following the alumina, we deposit 10 nm of cobalt.

5.2.1 Deposition of Terbium-doped Permalloy

We found using our normal evaporation boats, molybdenum coated in alumina (Mo-AlO), caused a reaction with the terbium immediately destroying the evaporation boats when the material melted. As a solution, we used tungsten evaporation boats. These boats still appear to react with both the permalloy and terbium but allow for an evaporation rate of about 3 Å/s long enough to complete the deposition process. We validated the deposition process by making 15 nm thin films of permalloy using both types of evaporation boats and

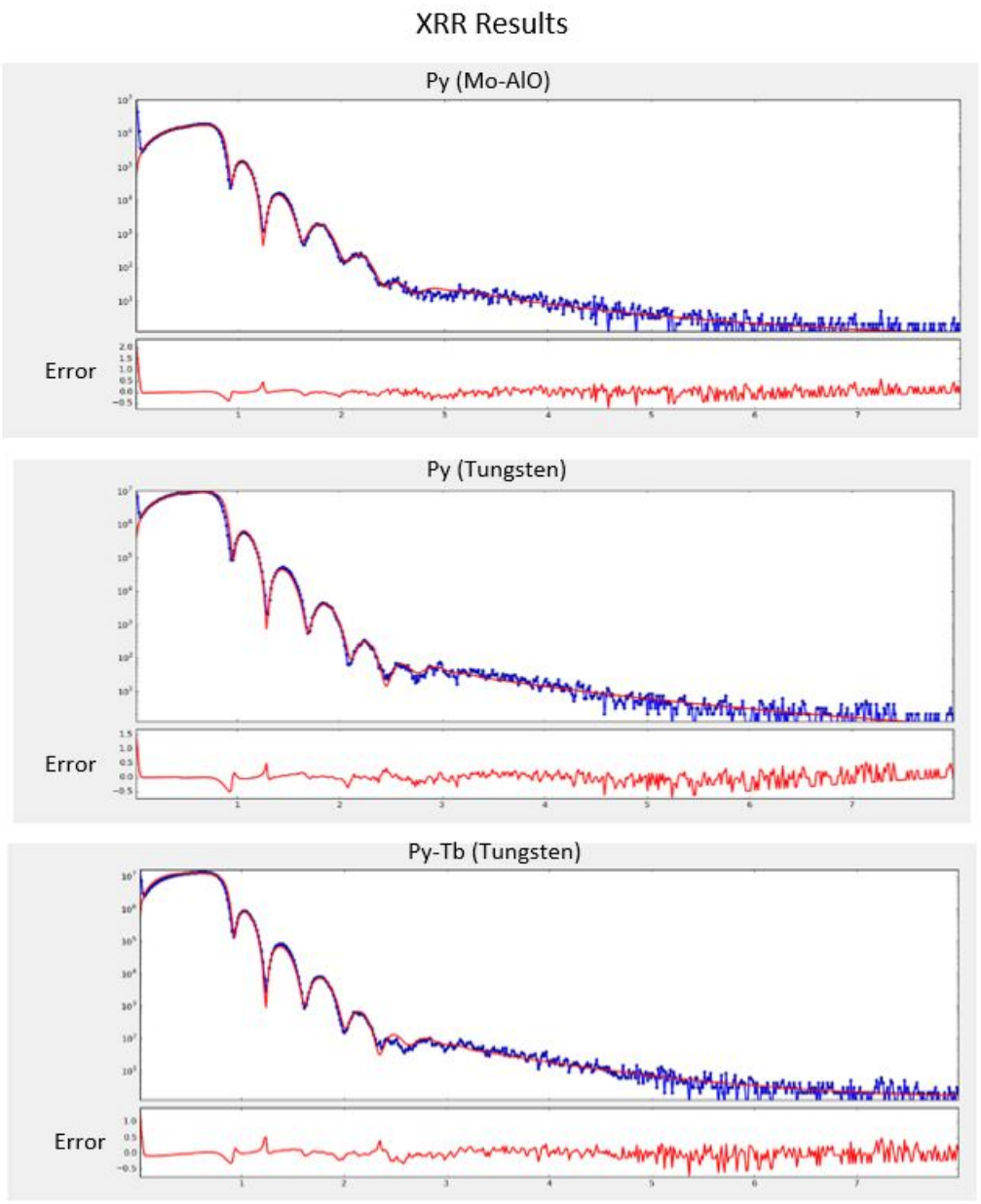

Figure 5.3: X-ray Reflectivity data for three 15 nm thin films. In each, the blue lines and markers are the recorded data, the red line is the fit, and the plot below each is the relative error between the fit and the data. The figures are labeled to show the material and the evaporation boat. Top: Permalloy film deposited using an alumina coated molybdenum boat. Middle: Permalloy film deposited using a tungsten boat. Bottom: Terbium-doped permalloy deposited using a tungsten boat.

a 15 nm thin film of the terbium-doped permalloy using a tungsten evaporation boat. Using the Quantum Heterostructures Group facilities at ORNL, we performed x-ray reflectivity (XRR) measurements on each thin film. We used the open-source software package GenX

to fit each result. The results of the measurement and fit are shown in Figure 5.3.

Looking at the three XRR results, there appears to be a slight difference in the data near the last "bump" when comparing the different evaporation boats (top vs. middle and bottom). The two sets of data for the tungsten boat (middle and bottom) appear very similar. The thicknesses of the films per the XRR fit showed an increase in the expected deposition thickness of 22.5%, 15.7%, and 22.2% for the permalloy deposited using the Mo-AlO boat, the permalloy deposited with the tungsten boat, and terbium-doped permalloy deposited with the tungsten boat, respectively.

In an attempt to verify the elemental composition of each film, we leveraged the capabilities at the Center for Nanophase Materials Sciences (CNMS) at ORNL. We used the Merlin FE-SEM with a Bruker EDS attachment to perform energy-dispersive x-ray spectroscopy on each film. The smallest analysis depth is only 2 μm, so the silicon dioxide and silicon of the substrate dominated each output. Figure 5.4 shows the EDS results from each film.

For the permalloy thin films, we can compare the ratios of nickel and iron mass percentages for the top and middle table of Figure 5.4. The top gives $Ni_{0.81}Fe_{0.19}$ and the middle, $Ni_{0.78}Fe_{0.22}$. Comparing these values to our starting source, $Ni_{0.8}Fe_{0.2}$, shows that the deposited alloys are close to what we expect. The middle table shows no tungsten although a small peak appears above 8 keV near the tungsten label. The top table shows both molybdenum and aluminum impurities. Adding these to the total permalloy (nickel and iron) gives an impurity content of 7% by mass. From these results, it appears depositing permalloy with a tungsten boat produces less impurities than that of an alumina-coated molybdenum boat.

The terbium-doped permalloy results are quite strange. The evaporation source material contains $Ni_{0.8}Fe_{0.16}Tb_{0.04}$, giving a 4% terbium content by mass. If we first look at only the nickel and iron content, the above ratio should produce an alloy containing $Ni_{0.83}Fe_{0.17}$, but the EDS result gives $Ni_{0.71}Fe_{0.29}$. Furthermore, there is a non-zero tungsten contribution

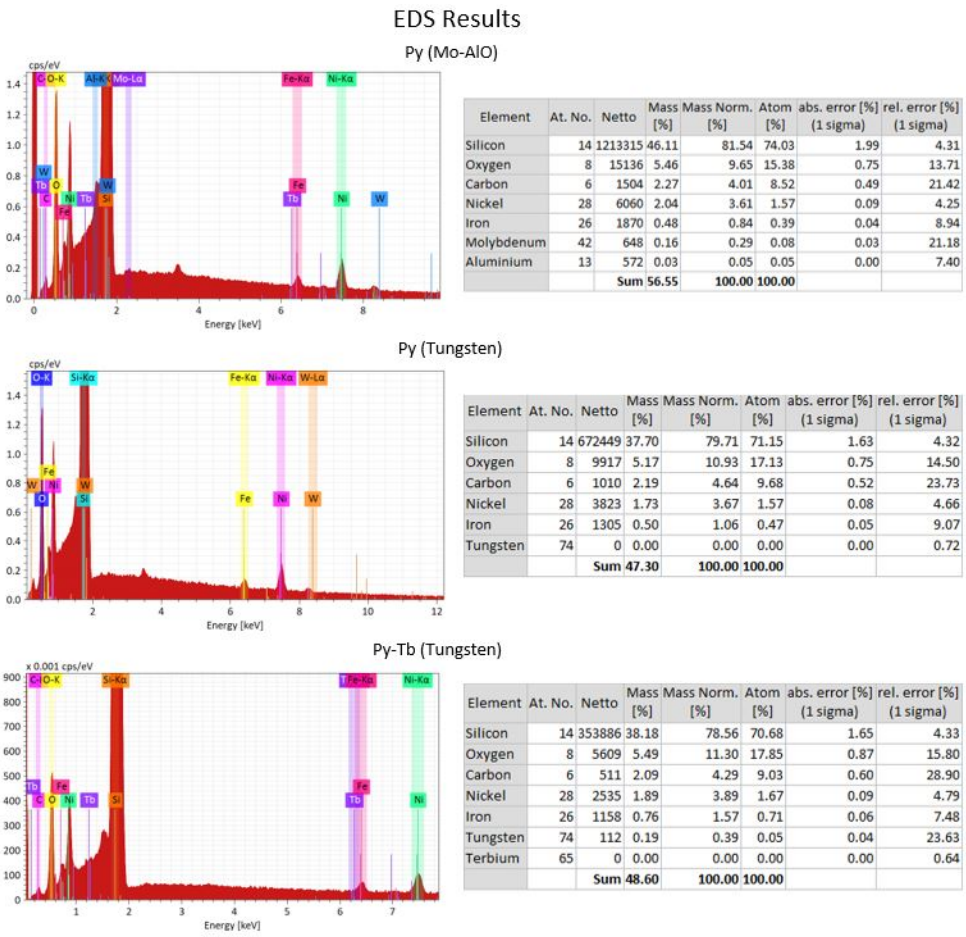

Figure 5.4: EDS results from each of the thin films. The plots on the left shows the spectrum from each film. The markers on the spectra give the expected position of peaks for each element. The tables on the right show the composition of each film.

leading to an impurity concentration of 7% by mass and no apparent terbium in the output table. The terbium peak target above 6 keV is located very close to the iron peak, and the low energy peak target around 1.2 keV is centered between two small peaks, so there may be other effects hiding the terbium content.

We proceed assuming that there is some terbium content in the terbium-doped permalloy film. The error may be caused by the small amount of terbium in the source (only 4%), the small thickness of the film (15 nm, or 18 nm from XRR, compared to the 2 μm measurement depth), or even some other interactions in the material causing an unanticipated shift in the emission spectra of the terbium.

5.3 Quasi-Static Measurments of DMTJs

We used the Quantum Isolation and Observation System of the Quantum Heterostructures Group at ORNL to perform low temperature DC voltage sweeps and hysteresis loops on terbium-doped and undoped samples of each device design. The measurement system includes a Stanford Research Systems DS335 Function Generator used as a voltage source, an Ithaco Model 1211 TIA to measure the current through each device, and a Keithley 2182A Nanovoltmeter to measure the output from the TIA. Both the nanovoltmeter and function generator connect to a measurement computer using GPIB. We use NI LabView to control the equipment and communicate with the fridge for both controlling and recording the magnetic field and temperature as needed. For each measurement, we set the TIA integration time to 30 ms, monitor the signal-to-noise ratio, and adjust the integration time and/or averaging buffer size of the nanovoltmeter as needed. We found an integration time of 33-83 ms and a buffer size of 5 sufficient for most measurements.

For figure labels throughout this chapter, we designate different device designs using D1 or D2 relating to Figure 5.2 (a) and (b) or (c) and (d), respectively. We also specify whether terbium-doping is present by referring to the material stack of the entire device, Co-Py-Co or Co-PyTb-Co. Each device is mounted on a chip holder using copper tape. The device leads make electrical contact to the chip holder through small gold wires bonded with indium to each device and the chip holder pads. The chip holder connects to a PCB which is mounted to a sample holder with copper tape aligning the magnetic field axis of the fridge with the easy-axis of the device leads. Due to the sensitivity of the samples, during the mounting process, the chip holder contacts must stay shorted to avoid any charge build up leading to a potential difference across the sample leads. Once connected to the sample holder and later to the fridge as well, each sample lead is grounded through a 1 MΩ resistor to mitigate the effects of any transient voltages produced from the system during the cool down process.

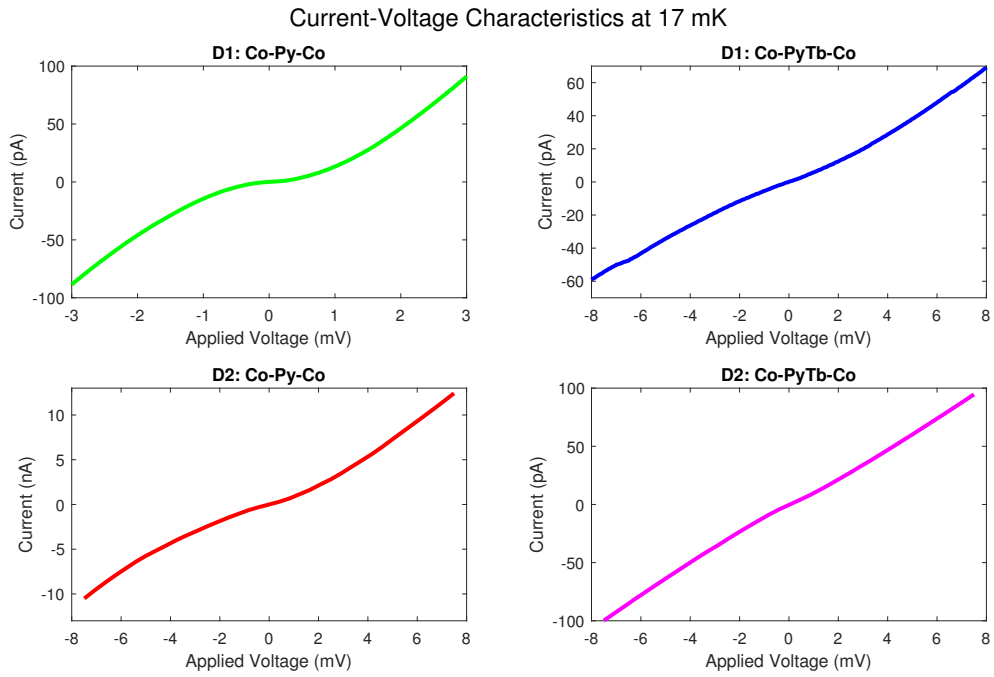

Figure 5.5: IV curves of each sample at 17 mK. The voltage range was adjusted for each sample to better see the zero bias anomaly. Note the different current scale in the D2: Co-Py-Co sample (bottom left) and the different voltage scale in the D1: Co-Py-Co sample (top left).

5.3.1 Electron Transport with no Applied Field

Figures 5.5 and 5.6 show the IV curves and differential conductance plots of each sample at 17 mK, respectively. The sample measured is labeled at the top of each pane in each figure, and the colors of each plot are used for consistency for each sample throughout this section.

We measure the IV curves through a series of discrete voltage steps. We set a voltage, allow for 100 ms of settling time, measure the current, and then set a new voltage as needed. We calculate the differential conductance from each IV curve using a ratio of the central finite differences of respective current and voltage data points.

In Figure 5.5, the current scale shifts slightly between each sample except in the bottom left pane where it changes to the nA range. The voltage scale was chosen to sufficiently capture the zero bias anomaly (ZBA) of each sample. The ZBA in magnetic tunnel junctions

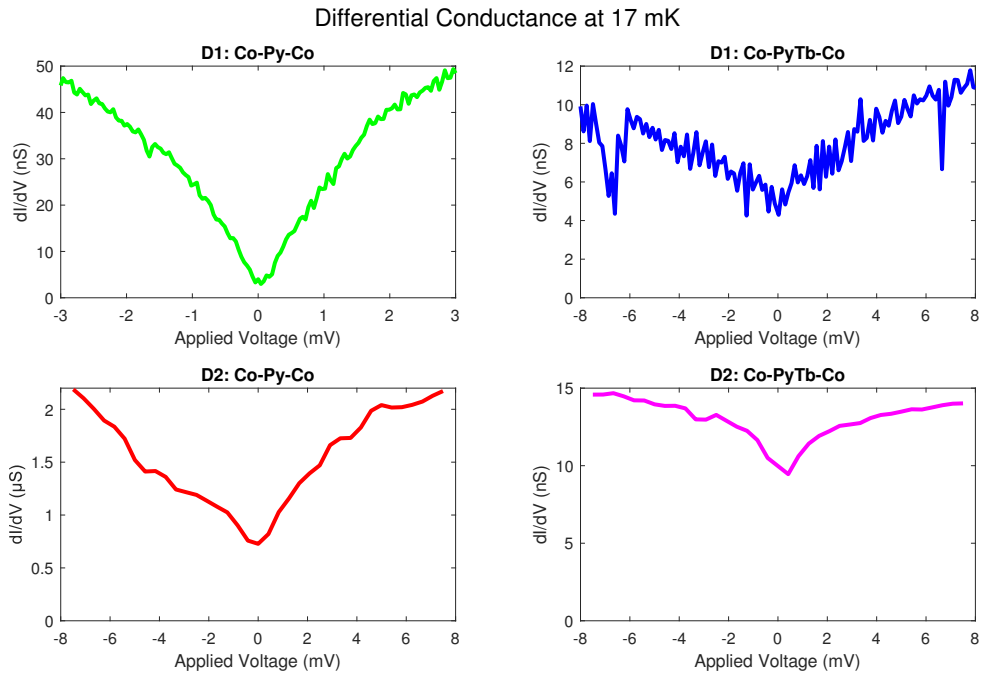

Figure 5.6: Differential conductance of each sample at 17 mK. These plots show the zero bias anomaly of each sample much better than that of the IV curves. Each plot includes the zero conductance on the y-axis causing come plots to appear more shifted than others. This allows for a better comparison between the zero bias anomalies of different samples. Note the different conductance scale in the D2: Co-Py-Co sample (bottom left) and the different voltage scale in the D1: Co-Py-Co sample (top left).

appears as a cusp-like shape in the low voltage conductance of the junction. Each sample has varying amounts of asymmetry, but two stand out above the rest. The terbium-doped sample of the first design (top right pane) has a noticeable kink around -6 mV. Another kink occurs at 6 mV, but the negative bias one is more significant. The undoped sample of the second design (bottom left pane) has an 18% increase in the current magnitude at max positive bias (12.42 nA) compared to that of the max negative bias (10.51 nA). The zero bias anomaly is better shown in the differential conductance plots of Figure 5.6, but comparison between the undoped and doped samples of each design (left vs. right panes) shows a change in linearity. Specifically, for each design, the undoped samples appear to have more non-linearity in the IV curves than the terbium-doped samples.

The differential conductance plots in Figure 5.6 give a great view of the ZBA of each

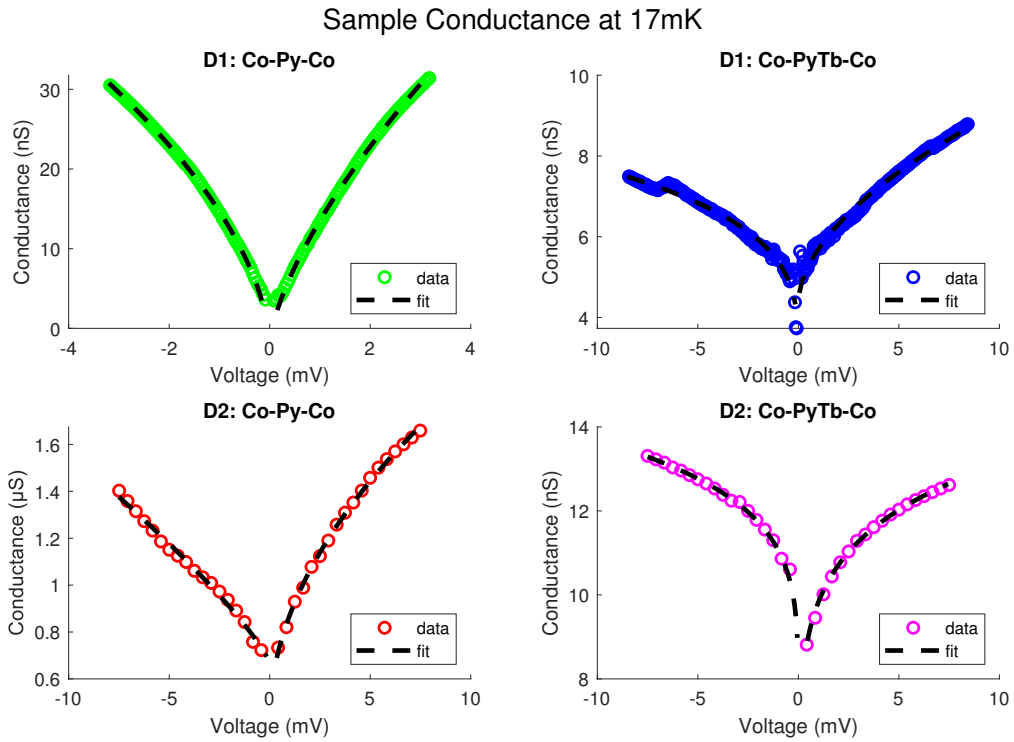

Figure 5.7: Conductance with respect to applied voltage for each sample at 17 mK and no applied field. The data is shown by colored circles and each fit is shown by a dashed black line. Due to the asymmetry of the conductance, each plot was fit separately for the positive and negative voltages (shown) as well as the entire plot (not shown).

sample. Instead of shifting the conductance (y-axis) window of each plot to the max and minimum conductance values of each plot, we extend the y-axis range to include zero conductance. This gives a much better comparison between the ZBA of each sample. The voltage range of each plot matches that of the IV curves, and similar to the IV curves, the conductance range of the bottom left pane is higher than the other plots (μS instead of nS). The difference in non-linearity mentioned previously in regards to the IV curves is more easily seen in these plots. In this case, the terbium-doped samples show a smaller percent change between their maximum and minimum differential conductance values. The differential conductance plots of each sample also have an asymmetry about the positive and negative bias as well.

Over the years, many theories have emerged regarding ZBAs in magnetic tunnel junc-

Table 5.1: Fit parameters from the conductance of each sample at 17 mK following Equation (5.1) in Figure 5.7

Sample	G_0 (nS)	a (μS/V)	b
D1: Co-Py-Co	-2.92±0.88	1.21±0.45	0.607±0.068
D1: Co-PyTb-Co	3.60±0.75	0.039±0.021	0.416±0.13
D2: Co-Py-Co	550±114	26.9±11	0.666±0.15
D2: Co-PyTb-Co	3.42±2.8	0.0204±0.0027	0.160±0.027

.

tions. Multiple theories for ZBA show a power-law dependence of the conductance of the junction on the bias voltage[40, 96, 104, 109, 129], so we fit the conductance of each junction to the following function:

$$G(V) = a|V|^b + G_0, \tag{5.1}$$

where a, b, and G_0 are fitting parameters. Due to the asymmetry in the conductance with respect to applied voltage, we first fit the conductance to the entire voltage range to obtain starting fit parameters. Then, we fit the positive and negative voltage bias separately for each sample. The results of each fit are shown in Figure 5.7 where the colored circles represent the data, and the dashed lines show the fit for positive and negative voltages separately. Table 5.1 shows the average of each of the fit parameters for the positive and negative voltages of each plot and a range between the two values.

Recalling from Figures 5.5 and 5.6 that the undoped samples have significantly different ranges of current and conductance in both their IV curves and differential conductance plots, respectively, we still see that the exponent ranges produced from the fit overlaps with each other. The exponents of the terbium-doped samples do not overlap, but in both sample designs, they are lower than their undoped counterparts. The results of the fit do not directly determine which mechanism leads to the ZBA, however, the values of the exponents can rule out magnon-induced spin-flip scattering from reference [40] and hot electron excitement of magnons from reference [129]. These theories predict an exponent of 0, 2, or 3/2 and 1, respectively.

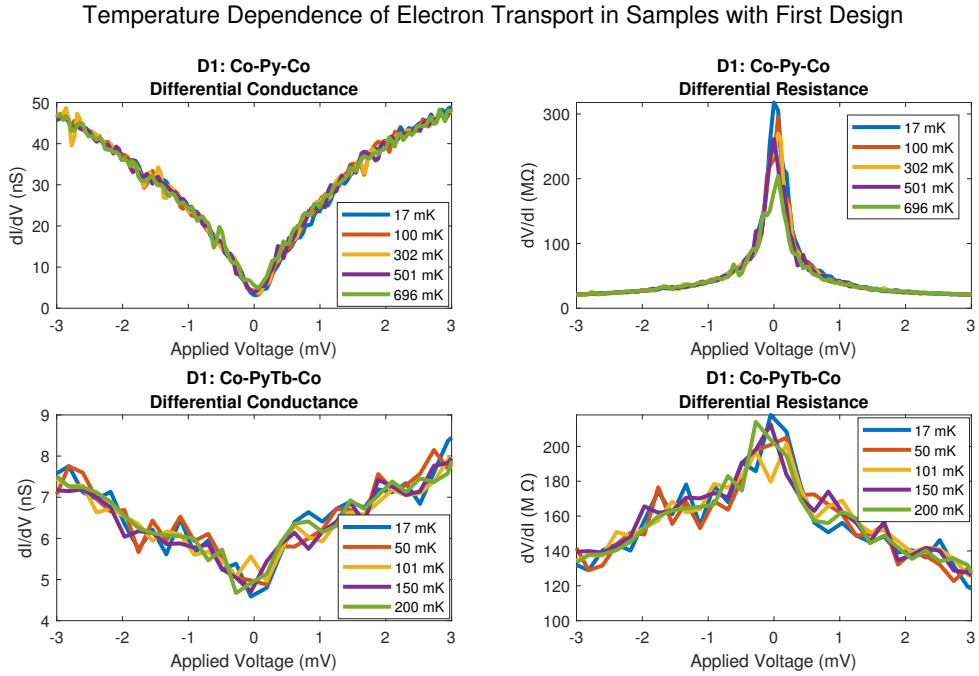

Figure 5.8: Differential conductance and differential resistance across temperature of the samples of the first design. Each pane is labeled accordingly and includes a legend for plots at each temperature. There appears to be a noticeable shift in the differential resistance peak across temperature for the undoped sample. The Tb-doped sample has a smaller temperature range, but does not appear to have any shift in peak height.

Temperature Dependence of Electron Transport

Figure 5.8 shows the temperature dependence of the electron transport in the samples of the first design. Due to the cusp-like shape of the zero bias anomaly in the differential conductance plots (left-side panes), differences near zero bias with respect to temperature are better shown using the differential resistance of each sample. In the undoped sample (top panes), a decrease in the peak height of the differential resistance appears with increasing temperature. Such a change does not appear in the Tb-doped sample. The lack of an apparent temperature dependence in the Tb-doped sample may be caused by the smaller temperature range used for this sample or the decreased zero bias anomaly discussed previously.

5.3.2 Electron Transport with an Applied Magnetic Field

Of particular importance is how the addition of terbium into the central DMTJ nanomagnet changes the magnetic properties of the entire system. To study this, we measured hysteresis loops for each sample. For each hysteresis loop, we held the sample at a constant bias voltage and swept the applied magnetic field from zero field to a positive field, then back down through zero field to a negative field, and, finally, back to zero field. Each time the field approached zero, we decreased the field ramp rate and paused the field at zero as well. The ramp rate was set to 0.02 T/min when below a field magnitude of 0.1 T, but was increased to 0.1 T/min for field magnitudes between 0.1 T and 0.5 T. Above 0.5 T, we set the ramp rate to the maximum value of 0.25 T/min. The adjusted ramp rate allows use to have a better resolution for any dynamics at low fields even when making large field sweeps. Additionally, decreasing the ramp rate near zero field and pausing the sweep at zero field for a rest time helps with magnet heating when changing field directions. The voltage bias for each sample was placed between the middle and top of the measured IV curves such that the TIA output voltage (after adjusting the range) was near 1 V. This provides both a large signal-to-noise ratio as well as plenty of output swing for the current to change due to TMR. We also captured the IV curves with respect to field. When measuring the first design, we ramped the field at a rate of 0.05 T/min and continuously swept the voltage back and forth throughout the field ramp. We adjusted the nanovoltmeter to remove the buffer and only take single measurements of the TIA output to increase the sampling rate. For the second design, in an attempt to reduce the noise in the data while still maintaining an acceptable measurement time, we paused the field at discrete field steps then captured the IV curves with the normal IV curve process instead of continuously sweeping both the field and voltage. The first approach gives a much better view of the hysteresis loops at each voltage than the second approach for a given total measurement time due to the higher density of data points collected.

It may prove useful to first discuss what we expect to see from the DMTJ. We use cobalt

leads and a central permalloy particle with/without a 4% terbium-doping. The coercive field of permalloy is lower than that of cobalt, so we expect the permalloy particle to flip its magnetization at a smaller applied field than that of the cobalt leads. A 4% concentration of terbium-doping added to permalloy thin films increased the coercive field of the film at room temperature, but only by 1-2 Oe (0.1-0.2 mT)[4]. Temperature dependence of the coercivity was not reported, so we assume the terbium-doped particle will have a lower coercive field than the cobalt leads as well. In MTJs, the different coercivities of each part of the junction manifests as a change in resistance when magnetic switching occurs. Due to the geometry of this DMTJ, when the magnetization of the leads are parallel to each other, the leads produce a nonzero magnetic field on the particle. As a result, a field shift in the hysteresis loop of the particle may be observable in the direction of the lead magnetization.

The junction should have two main resistance states and potentially a third intermediate state. One state occurs when both leads and the particle have the same magnetization direction. In most cases (positive TMR junctions), this would create a low resistance state. When the lead magnetizations are parallel and the particle magnetization is antiparallel to the leads, the junction (positive TMR) goes to a high resistance state. If the leads flip at different fields, the junction will take an intermediate resistance state at a value between the high and low resistance states. With identical leads, this intermediate state may be missing due to the magnetization of both leads flipping at the same field.

In the case that only the particle's magnetization switches, and the leads remain in a parallel magnetization direction, we expect to see the hysteresis loop of the particle by the change in resistance of the junction. If the leads are anti-parallel, we expect to see no TMR signal. If the particle hysteresis loop is shifted from zero field, we can determine the direction of the lead magnetizations with respect to the applied field. When the field is increased such that both leads flip their magnetizations as well, we expect to see a hysteresis loop similar to that of a normal MTJ such as that seen in Figure 4.3 in Chapter 4.

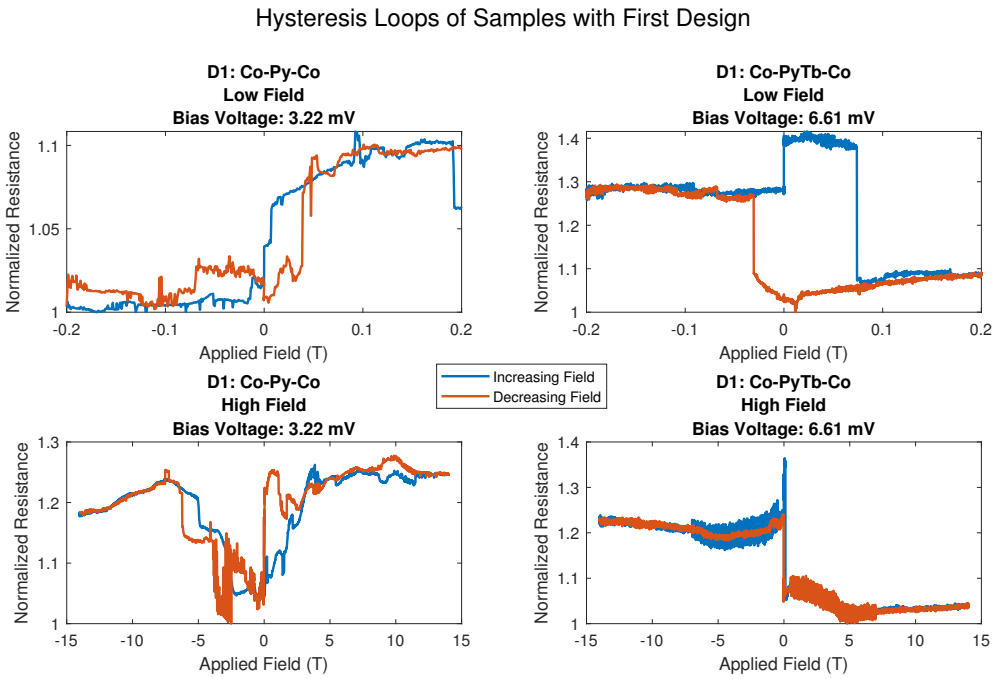

Figure 5.9: Hysteresis loops of the two samples made with the first design. The top panes show the low field (0.2 T) hysteresis and the bottom panes show the high field (14 T) hysteresis. The legend in the center of the figure gives the field direction for each plot. The normalized resistance shown is the actual resistance at each field divided by the minimum resistance of the entire sweep. Each pane is labeled by the sample, voltage bias, and high/low field. The temperature increased to almost 70 mK during the high field sweeps.

Sample Design 1

Hysteresis loops of the samples fabricated with the first design (Figure 5.2 (a) and (b)) are shown in Figure 5.9. The top two panes show the low field hysteresis (0.2 T) and the bottom panes show the high field hysteresis (14 T). The offsets at the edges of the top left pane is due to the full sweep extending to 1 T. The temperature increased to almost 70 mK during the large field sweep for each sample possibly due to the extended length of the increased ramp rate, while the temperature remained relatively constant for the low field sweeps (17-19 mK).

The top panes of Figure 5.9 appear to show a hysteresis loop shifted in the positive direction. The total width of each supposed loop being 38 mT and 104 mT for the undoped

and terbium-doped sample, respectively. The center shift of each is 19 mT for the undoped sample and 22 mT for the terbium-doped sample both in the positive field direction. Switching in the top-right pane appears discrete going from the higher resistance to lower resistance in a single step less than 0.2 mT. In the top-left pane, the right side has a similar discrete step, but the left side stops at an intermediate state with a field width of 6.7 mT.

The large field hysteresis loops do not follow our initial expectations for the DMTJ hysteresis. In the undoped particle sample (bottom-left pane), we see multiple transitions at very high fields, and overall, the hysteresis loop does not look much like a MTJ hysteresis loop. At high fields, the resistance is at high values which may be an indicator of a negative TMR, but such speculations are difficult to justify considering the complex nature of the entire hysteresis loop. The noise seen in the decreasing part of the sweep between -2 T and -3 T consistently shows up in multiple hysteresis loops. We stopped the field ramp at a few points within this region and found that after waiting only one transition (if any) would occur. This seems to suggest that the noise is dependent on the dynamic field sweep. In the high field sweep of the terbium-doped sample (bottom-right pane), we see that the resistance state does not return back to a similar value in the positive and negative high field limits. We also see an increased noise while the field increases above -7 T to -0.5 T and while it decreases below 7 T to 0.5 T. This increased noise does not occur within these regions when the field sweeps the opposite direction. This noise is also present in multiple hysteresis loops.

The continuous IV sweeps during hysteresis loops showed another characteristic of these samples. Figure 5.10 shows the hysteresis loops of each sample (top and bottom) at negative and positive voltage bias (left and right). It appears that both samples have voltage bias dependent transitions in their hysteresis loops. The dashed boxes show the transitions in each plot and the letters correlate them between the positive and negative bias plots. Transitions A, B, and D appear to be stationary in field, but transition C appears to shift in field with applied voltage bias. At smaller voltage bias, transition C appears at a smaller

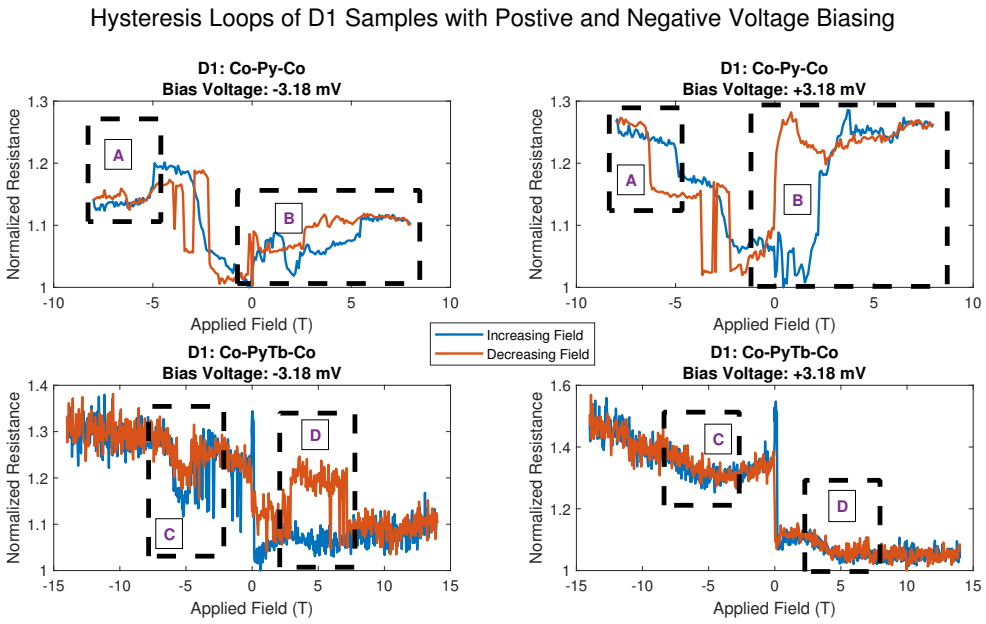

Figure 5.10: Voltage bias dependent transitions in the hysteresis loops. The top(bottom) panes show the permalloy(terbium-doped) sample where the left is at a negative voltage bias and the right is at a positive voltage bias. The dashed line boxes show each transition and the labels give a reference to where they are located in each plot.

field. At this point, we are unsure of the mechanism behind these transitions, but report them for the sake of completeness.

Sample Design 2

The second sample design had a slight change in the overlap of the leads and their evaporation shadows, plus an added alumina coating over the entire particle. It appears these changes improved the final results; however, with the limited number of samples measured (2 of each design each with different properties), such claims cannot be substantiated.

The top two panes of Figure 5.11 show 1 T hysteresis loops. In the permalloy sample (top-left pane), the field was swept further (to -1.5 T) to see if the sample would return to the low resistance state. During these low field sweeps, the temperature increased to 25 mK. The bottom panes show the high field hysteresis loops. The hysteresis loop of the undoped sample (bottom-left) extends to 8 T, while that of the terbium-doped sample extends to

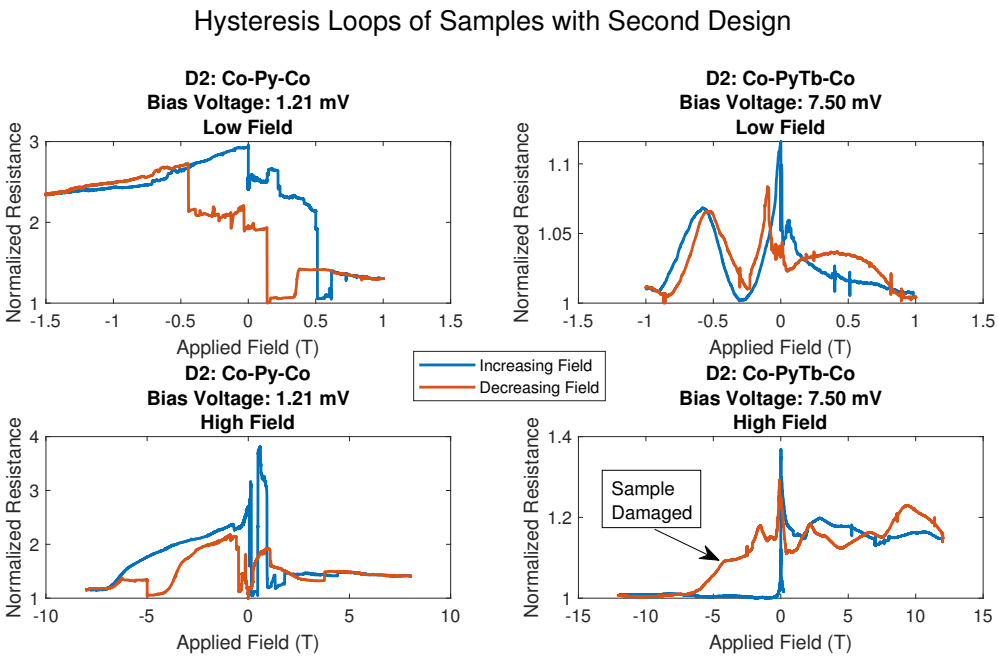

Figure 5.11: Hysteresis loops of the two samples made with the second design. Hysteresis loops at low fields of approximately 1 T (top panes) and to higher fields of 8 T and greater. The terbium-doped sample was damaged during the high field sweep causing a drop in overall resistance. Although there are other artifacts, the samples clearly have a large and small resistance state. Both samples show a directional field dependence on the TMR. The normalized resistance shown is the actual resistance at each field divided by the minimum resistance of the entire sweep. Each pane is labeled by the sample, voltage bias, and high/low field. The temperature increased to almost 60 mK in the high field sweeps and 25 mK in the low field sweeps.

14 T. The temperature of the high field sweeps increases to almost 60 mK throughout the sweep.

For the undoped sample (top-left), the width of the apparent hysteresis loop is 956 mT and shifted in the positive direction by 34 mT. The intermediate state has a field width of 500 mT when the field is increasing and 580 mT when the field is decreasing, but there is an offset between the resistance of the intermediate state of 23-27% depending on whether the field is increasing (higher) or decreasing (lower). The transitions to and from the intermediate states appear to be discrete within the sweep resolution (approximately 1 mT) except for the right side transition in the increasing field. The pane below (bottom-left) shows the large field hysteresis loop of this sample. The increasing field resistance maxi-

mum occurs at 588 mT returning to a low resistance state at 977 mT. If this relates to the parallel configuration of the leads and particle, it is strange that the low field sweep (which goes up to 1 T) only looks like a particle hysteresis loop as opposed to an MTJ switching. There also appears to be a sharp drop in resistance right before the maximum resistance peak that is 316 mT wide. The large width of this transition appears to rule out a random noise spike. This also does not show up in the low field sweep, but may be related to the underlying difference in switching between the low and high field sweeps. When the field is decreasing, there is a significant difference in the TMR of the whole junction. There is another high and low resistance transition similar to that in the increasing field sweep albeit with a much smaller change in resistance (80% change instead of 260% change).

For the terbium-doped sample (top-right), it appears the full expected switching of the junction takes place within the small field hysteresis loop. The maximum resistance states for increasing and decreasing resistance are not symmetric about zero. The maximum resistance with increasing field occurs very close to zero (0.7 mT), but this field is from the field overshoot when increasing from the negative direction, and it drops shortly after. When increasing from zero field, the resistance initially increases within 1 mT, so the actual transition to the high field state must be somewhere very near to zero field. When the field is decreasing, the maximum resistance state occurs at -98 mT. Similar to the undoped sample, the TMR of the decreasing field is smaller than that of the increasing field. This time the difference is only 8%, but this value pertains to half the measured TMR (total 16%). In both cases, the transition is fairly smooth aside from a few discrete steps very near to each maximum peak. In both field directions, there occurs a smaller peak/intermediate state at a slightly higher field (to the right) of the maximum resistance peak. This peak occurs at 62 mT and 12 mT for the increasing field sweep and decreasing field sweep, respectively. Also, we see smooth oscillations of the resistance on the outside edge of the hysteresis loop. The larger field sweep for this sample is shown in the pane below (bottom-right). During this sweep, the sample was damaged marked by a decrease in resistance and

overall drop in TMR. The cause of the damage is unknown, but was marked with a sudden increase in noise of the measurement causing the TIA input to overload. The increasing field maximum of this sweep occurs at 11 mT, and the decreasing field maximum occurs at -103 mT. Although these are shifted from the low field hysteresis values, the shift appears to be small, about 10 mT and 5 mT respectively. Before the device was damaged, we see resistance oscillation throughout the entire positive field (increasing and decreasing), but the increasing and decreasing field resistance oscillations do not appear to line-up, nor do the oscillations appear to have a common period. At this point, we are unsure of the cause of these oscillations.

Comparing the hysteresis loops of the positive and negative voltage bias for the samples of the second design do not show the same voltage-dependent transitions of the first design. It is possible that the lower field resolution masked any transitions, or that the different sample design/fabrication process "fixed" the initial cause.

Compared to the results from Figure 5.9, these samples show a significant improvement towards our initial expectation for the hysteresis loops of the DMTJ system for both sample types. Although there still exist some artifacts, we see high and low resistance states that shift with field sweep direction. Because the hysteresis looks better, we used the IV curves near the maximum and minimum resistance states (disregarding where the terbium-doped sample was damaged) to calculate a TMR with respect to applied voltage. Due to the discreteness of the field points chosen, we picked the closest points to the actual minimum and maximum resistance states. We calculated the TMR using the following modified formula:

$$TMR = \frac{R_{max} - R_{min}}{R_{min}}. \tag{5.2}$$

Figure 5.12 shows the results. We see a moderate TMR in the terbium-doped sample (12-16%), but a very large TMR in the undoped sample (197-220%).

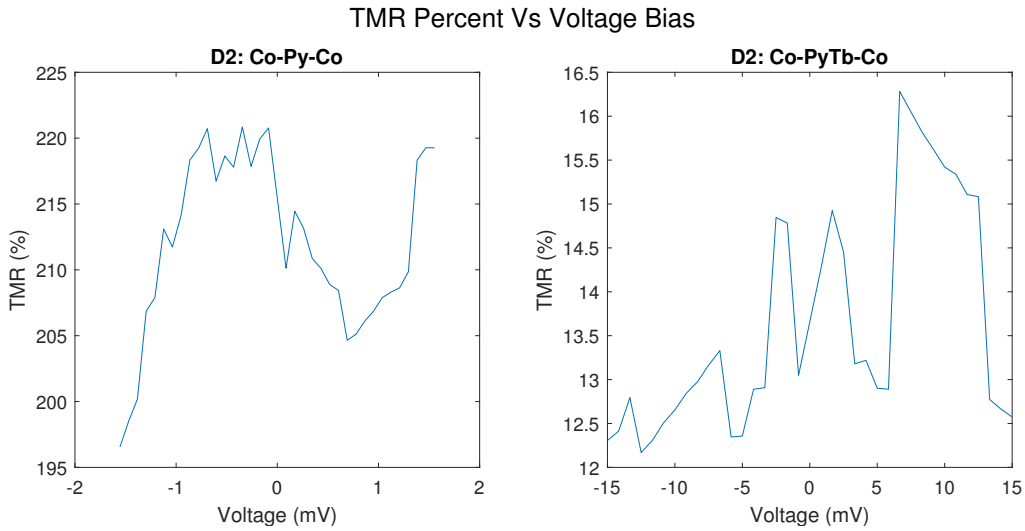

Figure 5.12: TMR percent as a function of applied voltage bias for both samples of the second design.

5.4 Conclusion

We fabricated double magnetic tunnel junctions with two slightly different designs to study the effects of terbium-doping in permalloy nanomagnets. We give details on how to fabricate similar samples using electron beam lithography and thermal evaporation deposition. From the low temperature current-voltage characteristics, we found that the addition of terbium into a permalloy nanomagnet within a DMTJ appears to decrease the ZBA of the junction. After fitting the conductance of each sample to a power-law function, we find that the exponents of the terbium-doped samples in both sample designs decreases in comparison to the undoped samples of each design. Furthermore, even with a significant difference in conductance and magnetic field response of the two junctions, the undoped samples of each design have very similar values for the exponent of the power-law fit. This seems to suggest that the addition of terbium to the permalloy magnet causes a notable difference in the electron transport of the DMTJ. The addition of terbium-doping to permalloy thin films has been shown to change the microstructure of the films from polycrystalline to amorphous with increasing doping concentration[4, 66]. This brings into question whether the

change in ZBA is caused by increased environmental coupling, increased disorder of the particle, or other processes.

From our measurements, the second sample design appears to show magnetic hysteresis closer to what we expect for DMTJs, but anomalies still exist in each sample such as extra transitions between the high and low resitance state of the undoped sample, and smooth resistance oscillations with respect to field in the terbium-doped sample. The TMR of the undoped sample is extremely high compared to previous low temperature measurements of series of nanoscale permalloy-alumina-cobalt MTJs[11]. Enhanced TMR in DMTJs is a well-known phenomenon caused by cotunneling within the Coulomb blockade regime[105]. The previous measurements by Brückl *et al.* only showed a TMR of 17% in the Coulomb blockade regime[11], but our results show an enhancment of over 10X this value. This enhancement of the TMR helps to validate the fabrication and design of these junctions; however, the existence of such a large TMR in only one junction suggests more study is needed to confirm variations between samples.

Overall, we hope that these experiments help to lay the ground work for studying the effect of different environmental coupling in large spin systems. With the current results, we cannot objectively comment on whether terbium-doping increases the environmental coupling of the permalloy system in such a way measurable by electron transport in a DMTJ; however, our results do not rule out the possibility.

We would like to thank the ORNL Quantum Heterostructures Group and the ORNL Center for Nanophase Materials Science for their help including the use of equipment, training, and data collection. This chapter is based upon work supported by the U.S. Department of Energy, Office of Science, Office of Workforce Development for Teachers and Scientists, Office of Science Graduate Student Research (SCGSR) program. The SCGSR program is administered by the Oak Ridge Institute for Science and Education for the DOE under contract number DE-SC0014664. Experiments of the second sample design were supported by the ORNL Core Liaisons Partnership.

CHAPTER 6
CONCLUSION AND FUTURE WORK

Throughout this thesis I have discussed nanoscopic fabrication techniques for magnetic tunnel junctions (MTJs) and double magnetic tunnel junctions (DMTJs), operation of silicon-germanium heterojunction bipolar transistors (SiGe HBTs) down to millikelvin temperatures, cryogenic preamplification of the tunnel mangnetoresistance (TMR) signal from high resistance MTJs, and electron transport in DMTJs incorporating nanomagnets with and without terbium-doping. At this point, I find it pertinent to point out possible directions of future research for the interested reader.

In regards to the fabrication techniques, in Chapter 2, I discussed in detail the nanofabrication process used in our lab and how it was modified to produce the DMTJs for Chapter 5. Chapter 5 also gives more information on the fabrication process regarding the types and amounts of materials used during fabrication. In the end, the yield for the DMTJs produced for this thesis never exceeded 50%. The low yield appears to be caused by random variations during the electron beam lithography, but it may be possible to design a pattern and/or process that would minimize the effect of these variations on the final product. Increasing the yield and decreasing the variations between different DMTJ samples would ultimately allow for more conclusive results on the effect of terbium-doping on the electron transport through a central nanomagnet in a DMTJ.

In Chapter 3, the collector current is modeled by electron tunneling through the base, where the base-emitter voltage changes the tunneling barrier and leads to a change in collector current. This result provides a fantastic model for developing a "simple" cryogenic preamplification circuit such as that used in Chapter 4. In the interest of completeness, further study of the base current at deep cryogenic temperatures may provide more insight into the physics of SiGe HBTs at deep cryogenic temperatures.

In Chapter 4, I used a high resistance MTJ to model a nanoparticle sample and showed that cryogenic preamplification at 8 K could increase both the signal-to-noise ratio and bandwidth of TMR measurements. Results from Chapter 3 showed that the gummel characteristics of the SiGe HBTs studied remained largely the same below 16 K; however, for verification, a similar cryogenic preamplification experiment completed at millikelvin temperatures could prove to be insightful. Also, changing the sample to a DMTJ, such as that used in Chapter 5, or to other nanoparticle-based samples would open the door to previously immeasurable, real-time dynamics within the system using electron transport. Furthermore, the "simple" circuit used in Chapter 4 was chosen as a first step. In reality, the circuit is not a classic amplifier since the changing resistance of the MTJ leads to a changing bias on the transistor. A next step may involve designing a classic common-emitter amplifier using passive components tested at cryogenic temperatures and capacitively coupling the MTJ to the resulting cryogenic common-emitter amplifier. Although such a design sounds simple in theory, every component adds an additional level of complexity and variations to account for when cooling the entire arrangement to cryogenic temperatures. Such a design may allow future researchers to push the limits on real-time, cryogenic, electron transport measurements.

In Chapter 5, I fabricated a DMTJ with a disc-shaped central nanomagnet with a radius of approximately 100 nm. Electron transport through permalloy and terbium-doped permalloy nanomagnets showed a decrease in the zero bias anomaloy of the samples with terbium-doping. One of the undoped permalloy samples also showed a large TMR enhancemant. The perceptive reader may ask why this specific DMTJ design was chosen. Before discussing the reasoning behind the design, this brings to light another possible direction of future research. Specifically, if a different DMTJ design was developed with asymmetric tunneling barriers to and from the nanoparticle, the spin relaxation time of the nanomagnet could be calculated from the resulting TMR oscillations of the sample. The results would be great for comparing the effects of terbium-doping in permalloy nanomagnets.

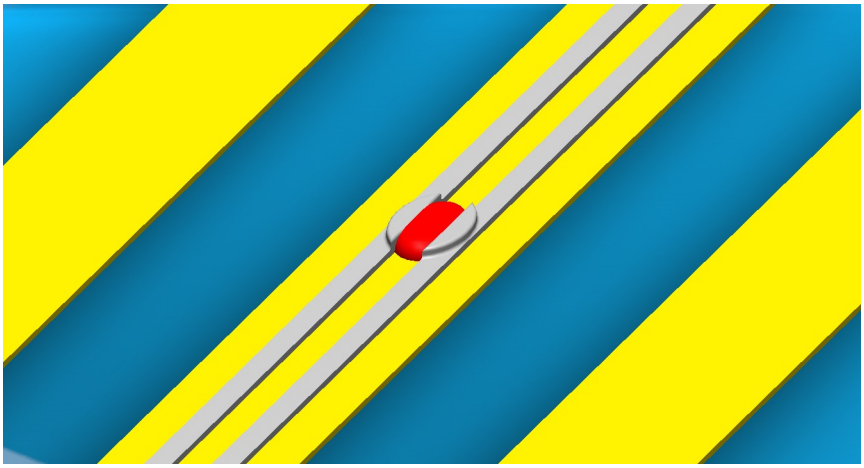

Figure 6.1: Double magnetic tunnel junction similar to those used in Chapter 5 placed on a CPW. The central nanomagnet is red, the cobalt leads are grey and the CPW is yellow. Sizes are NOT to scale. After developing the DMTJ from Chapter 5, the leads would not be able to extend past the nanomagnet, and instead, would be truncated on one side at the nanomagnet. Evaporation shadows of the DMTJ are not shown.

The DMTJ design used in Chapter 5 was chosen with a future experiment in mind. This design allows for the device to be placed on a coplanar waveguide (CPW) without extensive modifications to the fabrication process. Furthermore, as shown in Figure 6.1, this design allows for the central nanomagnet of the DMTJ to be much closer to the CPW than other DMTJ designs. The closeness of the nanomagnet to the CPW allows for the magnetic field produced by the CPW to have a larger effect on the nanomagnet than if it was further away, or worse, sandwiched between magnetic leads. The CPW makes it possible to drive the nanomagnet with microwave frequency magnetic fields by connecting the end of the CPW to a microwave generator (and any necessary impedance matching circuitry). Classically, when the nanomagnet of the DMTJ is continuously driven strongly enough by an alternating magnetic field produced by the CPW to continuously rotate the nanomagnet magnetization direction, the DMTJ should have no TMR. As a result, a simple, time-averaged TMR measurement of this system would instead probe the underlying quantum correlation of the spins of electrons tunneling on and off the nanomagnet. The key to the measurement is the need for strong environmental coupling to dissipate the magnetic energy faster than it is pumped into the nanomagnet, hence, the terbium-doping introduced

to the system in Chapter 5.

REFERENCES

[1] Aoki, T. et al. “Dynamic Magnetic Intermediate State during Nanosecond Spin Transfer Switching for MgO-Based Magnetic Tunnel Junctions”. In: *Applied Physics Express* 3.5 (2010), p. 053002.

[2] Aradhya, S. V. et al. “Nanosecond-Timescale Low Energy Switching of In-Plane Magnetic Tunnel Junctions through Dynamic Oersted-Field-Assisted Spin Hall Effect”. In: *Nano Letters* 16.10 (2016), p. 5987.

[3] Ashcroft, Neil W and Mermin, N David. *Solid state physics*. Vol. 3. Cengage Learning, 1976. ISBN: 0030839939.

[4] Bailey, W. et al. “Control of magnetization dynamics in Ni81Fe19 thin films through the use of rare-earth dopants”. In: *IEEE Transactions on Magnetics* 37.4 (2001), p. 1749.

[5] Barber, HD. “Effective mass and intrinsic concentration in silicon”. In: *Solid-State Electronics* 10.11 (1967), p. 1039.

[6] Bardeen, John and Brattain, Walter Hauser. “The transistor, a semi-conductor triode”. In: *Physical Review* 74.2 (1948), p. 230.

[7] Barnaś, J et al. “Spin effects in ferromagnetic single-electron transistors”. In: *Physical Review B* 62.18 (2000), p. 12363.

[8] Beach, G. S. D. et al. “Dynamics of field-driven domain-wall propagation in ferromagnetic nanowires”. In: *Nature Materials* 4.10 (2005), p. 741.

[9] Berger, L. “Multilayer configuration for experiments of spin precession induced by a dc current”. In: *Journal of Applied Physics* 93.10 (2003), p. 7693.

[10] Bloch, Felix. “Über die quantenmechanik der elektronen in kristallgittern”. In: *Zeitschrift für physik* 52.7 (1929), p. 555.

[11] Brückl, Hubert et al. “Enhanced magnetoresistance of permalloy/Al-oxide/cobalt tunnel junctions in the Coulomb blockade regime”. In: *Physical Review B* 58.14 (1998), R8893.

[12] Brinkman, WF, Dynes, RC, and Rowell, JM. “Tunneling conductance of asymmetrical barriers”. In: *Journal of applied physics* 41.5 (1970), p. 1915.

[13] Brown, W. F. “Thermal Fluctuations of a Single-Domain Particle”. In: *Physical Review* 130.5 (1963), p. 1677.

[14] Chappert, C., Fert, A., and Van Dau, F. N. “The emergence of spin electronics in data storage”. In: *Nature Materials* 6.11 (2007), p. 813.

[15] Christy, RW. “Charge-carrier equilibrium in semiconductors according to the mass-action law”. In: *American Journal of Physics* 40.1 (1972), p. 40.

[16] Clerk, A. A. et al. “Introduction to quantum noise, measurement, and amplification”. In: *Reviews of Modern Physics* 82.2 (2010), p. 1155.

[17] Cohen, Morrel H. “Review of the theory of amorphous semiconductors”. In: *Journal of Non-Crystalline Solids* 4 (1970), p. 391.

[18] Colis, S et al. “Low tunnel magnetoresistance dependence versus bias voltage in double barrier magnetic tunnel junction”. In: *Applied physics letters* 83.5 (2003), p. 948.

[19] Cressler, J. D. “Silicon-Germanium as an Enabling Technology for Extreme Environment Electronics”. In: *IEEE Transactions on Device and Materials Reliability* 10.4 (2010), p. 437.

[20] Cressler, J.D. and Niu, G. *Silicon-germanium Heterojunction Bipolar Transistors*. Artech House, 2003. ISBN: 9781580533614.

[21] Curry, M. J. et al. “Cryogenic preamplification of a single-electron-transistor using a silicon-germanium heterojunction-bipolar-transistor”. In: *Applied Physics Letters* 106.20 (2015), p. 203505.

[22] Dark, J. et al. “Increasing the signal-to-noise ratio of magnetic tunnel junctions by cryogenic preamplification”. In: *Journal of Applied Physics* 125.16 (2019), p. 163902.

[23] Davidovic, D. et al. “Tunneling, Current Gain, and Transconductance in Silicon-Germanium Heterojunction Bipolar Transistors Operating at Millikelvin Temperatures”. In: *Physical Review Applied* 8.2 (2017), p. 024015.

[24] De Teresa, JM et al. “Inverse tunnel magnetoresistance in Co/SrTiO 3/La 0.7 Sr 0.3 MnO 3: new ideas on spin-polarized tunneling”. In: *Physical Review Letters* 82.21 (1999), p. 4288.

[25] Devolder, T. et al. “Single-shot time-resolved measurements of nanosecond-scale spin-transfer induced switching: Stochastic versus deterministic aspects”. In: *Physical Review Letters* 100.5 (2008), p. 057206.

[26] Dolan, GJ. “Offset masks for lift-off photoprocessing”. In: *Applied Physics Letters* 31.5 (1977), p. 337.

[27] Doudin, B. et al. “Magnetoresistance governed by fluctuations in ultrasmall Ni/NiO/Co junctions”. In: *Physical Review Letters* 79.5 (1997), p. 933.

[28] Doyle, William D et al. “Magnetization reversal at high speed-an old problem in a new context”. In: *Journal of Magnetics Society of Japan* 22.3 (1998), p. 91.

[29] Engel, B. N. et al. “A 4-mb toggle MRAM based on a novel bit and switching method”. In: *IEEE Transactions on Magnetics* 41.1 (2005), p. 132.

[30] Ernult, F et al. “Spin-dependent single-electron-tunneling effects in epitaxial Fe nanoparticles”. In: *Applied physics letters* 84.16 (2004), p. 3106.

[31] Floyd, RB and Walmsley, DG. “Tunnelling conductance of clean and doped Al-I-Pb junctions”. In: *Journal of Physics C: Solid State Physics* 11.22 (1978), p. 4601.

[32] Fossum, JG. “Energy-band distortion in highly doped silicon”. In: *IEEE transactions on electron devices* 30.6 (1983), p. 626.

[33] Freitas, P. P. et al. “Magnetoresistive sensors”. In: *Journal of Physics-Condensed Matter* 19.16 (2007), p. 165221.

[34] Friedman, J. R. et al. “Macroscopic measurement of resonant magnetization tunneling in high-spin molecules”. In: *Physical Review Letters* 76.20 (1996), p. 3830.

[35] Gatteschi, D. and Sessoli, R. “Quantum tunneling of magnetization and related phenomena in molecular materials”. In: *Angewandte Chemie-International Edition* 42.3 (2003), p. 268.

[36] Gilbert, T. L. “A phenomenological theory of damping in ferromagnetic materials”. In: *IEEE Transactions on Magnetics* 40.6 (2004), p. 3443.

[37] Gittleman, JI, Goldstein, Y, and Bozowski, S. “Magnetic properties of granular nickel films”. In: *Physical Review B* 5.9 (1972), p. 3609.

[38] Grabert, Hermann and Devoret, Michel H. *Single charge tunneling: Coulomb blockade phenomena in nanostructures*. Vol. 294. Springer Science and Business Media, 2013. ISBN: 1475721668.

[39] Griffiths, David J. *Introduction to quantum mechanics*. Prentice Hall, second edi, 2010.

[40] Guinea, F. “Spin-flip scattering in magnetic junctions”. In: *Physical Review B* 58.14 (1998), p. 9212.

[41] Hahn, C. et al. “Time-resolved studies of the spin-transfer reversal mechanism in perpendicularly magnetized magnetic tunnel junctions”. In: *Physical Review B* 94.21 (2016), p. 214432.

[42] Hai, Pham Nam, Ohya, Shinobu, and Tanaka, Masaaki. “Long spin-relaxation time in a single metal nanoparticle”. In: *Nature nanotechnology* 5.8 (2010), p. 593.

[43] Horowitz, Paul and Hill, Winfield. *The Art of Electronics*. Cambridge Univ. Press, 1989. ISBN: 0521370957.

[44] Huai, Yiming et al. “Spin transfer switching current reduction in magnetic tunnel junction based dual spin filter structures”. In: *Applied Physics Letters* 87.22 (2005), p. 222510.

[45] Hurkx, GAM, Klaassen, DBM, and Knuvers, MPG. “A new recombination model for device simulation including tunneling”. In: *IEEE Transactions on electron devices* 39.2 (1992), p. 331.

[46] Ikeda, S et al. “Tunnel magnetoresistance of 604Ta diffusion in Co Fe B Mg O Co Fe B pseudo-spin-valves annealed at high temperature”. In: *Applied Physics Letters* 93.8 (2008), p. 082508.

[47] Ingvarsson, S. et al. “Electronic noise in magnetic tunnel junctions”. In: *Journal of Applied Physics* 85.8 (1999), p. 5270.

[48] Jiang, W., Birk, F. T., and Davidović, D. “Effects of confinement and electron transport on magnetic switching in single Co nanoparticles”. In: *Scientific Reports* 3 (2013), p. 1200.

[49] Jiang, W. C. et al. “Spin noise and damping in individual metallic ferromagnetic nanoparticles”. In: *Physical Review B* 96.24 (2017), p. 241402.

[50] Joseph, Alvin J, Cressler, John D, and Richey, David M. “Operation of SiGe heterojunction bipolar transistors in the liquid-helium temperature regime”. In: *IEEE Electron Device Letters* 16.6 (1995), p. 268.

[51] Julliere, M. “Tunneling between Ferromagnetic-Films”. In: *Physics Letters A* 54.3 (1975), p. 225.

[52] Kirk, K. J., Chapman, J. N., and Wilkinson, C. D. W. “Switching fields and magnetostatic interactions of thin film magnetic nanoelements”. In: *Applied Physics Letters* 71.4 (1997), p. 539.

[53] Kittel, C. *Introduction to Solid State Physics*. Wiley, 2004. ISBN: 9780471415268.

[54] Klaassen, DBM. "A unified mobility model for device simulation—I. Model equations and concentration dependence". In: *Solid-State Electronics* 35.7 (1992), p. 953.

[55] Koch, R. H. et al. "Magnetization reversal in micron-sized magnetic thin films". In: *Physical Review Letters* 81.20 (1998), p. 4512.

[56] Krivorotov, I. N. et al. "Time-domain measurements of nanomagnet dynamics driven by spin-transfer torques". In: *Science* 307.5707 (2005), p. 228.

[57] Kroemer, Herbert. "Theory of a wide-gap emitter for transistors". In: *Proceedings of the IRE* 45.11 (1957), p. 1535.

[58] Kronig, R de L and Penney, William George. "Quantum mechanics of electrons in crystal lattices". In: *Proceedings of the Royal Society of London. Series A, Containing Papers of a Mathematical and Physical Character* 130.814 (1931), p. 499.

[59] Lakshmanan, M. "The fascinating world of the Landau-Lifshitz-Gilbert equation: an overview". In: *Philosophical Transactions of the Royal Society a-Mathematical Physical and Engineering Sciences* 369.1939 (2011), p. 1280.

[60] Lee, JH et al. "TMR of double spin-valve type AF/FM/I/FM/I/FM/AF magnetic tunneling junctions". In: *Journal of magnetism and magnetic materials* 240.1-3 (2002), p. 137.

[61] Lei, Z. Q. et al. "Review of Noise Sources in Magnetic Tunnel Junction Sensors". In: *IEEE Transactions on Magnetics* 47.3 (2011), p. 602.

[62] Lenz, J. and Edelstein, A. S. "Magnetic sensors and their applications". In: *IEEE Sensors Journal* 6.3 (2006), p. 631.

[63] Lin, Y. et al. "Dissipative production of a maximally entangled steady state of two quantum bits". In: *Nature* 504.7480 (2013), p. 415.

[64] Liu, Ruisheng et al. "Tunneling magnetoresistance oscillations due to charging effects in MgO double barrier magnetic tunnel junctions". In: *Applied Physics Letters* 100.1 (2012), p. 012401.

[65] Lundqvist, Stig and Burstein, Elias. *Tunneling Phenomena in Solids: Lectures Presented at the 1967 NATO Advanced Study Institute at Riso, Denmark*. Plenum, 1969.

[66] Luo, C et al. "Investigations of magnetic properties of Tb-doped Ni78Fe22 thin films". In: *physica status solidi c* 9.1 (2012), p. 81.

[67] Maekawa, S. and Gafvert, U. “Electron-Tunneling between Ferromagnetic-Films”. In: *IEEE Transactions on Magnetics* 18.2 (1982), p. 707.

[68] Mao, S. N. et al. “Commercial TMR heads for hard disk drives: Characterization and extendibility at 300 Gbit/in(2)”. In: *IEEE Transactions on Magnetics* 42.2 (2006), p. 97.

[69] Marshak, Alan H and Van Vliet, CM. “Electrical current and carrier density in degenerate materials with nonuniform band structure”. In: *Proceedings of the IEEE* 72.2 (1984), p. 148.

[70] Meeks, T and Krieger, JB. “Temperature dependence of the resistivity of degenerately doped semiconductors at low temperatures”. In: *Physical Review* 185.3 (1969), p. 1068.

[71] Meservey, R. and Tedrow, P. M. “Spin-Polarized Electron-Tunneling”. In: *Physics Reports-Review Section of Physics Letters* 238.4 (1994), p. 173.

[72] Montaigne, F et al. “Enhanced tunnel magnetoresistance at high bias voltage in double-barrier planar junctions”. In: *Applied Physics Letters* 73.19 (1998), p. 2829.

[73] Moodera, Jagadeesh S, Nassar, Joaquim, and Mathon, George. “Spin-tunneling in ferromagnetic junctions”. In: *Annual Review of Materials Science* 29.1 (1999), p. 381.

[74] Nakajima, K et al. “Magnetoresistance oscillations in double ferromagnetic tunnel junctions with layered ferromagnetic nanoparticles”. In: *IEEE transactions on magnetics* 36.5 (2000), p. 2806.

[75] Neudeck, Gerold W. *The PN junction diode*. Addison Wesley Publishing Company, 1983. ISBN: 0201053217.

[76] Neudeck, Gerold W. *The bipolar junction transistor*. Vol. 3. Prentice Hall, 1989. ISBN: 0201122979.

[77] Niu, G. F. et al. “Transistor noise in SiGe HBT RF technology”. In: *IEEE Journal of Solid-State Circuits* 36.9 (2001), p. 1424.

[78] Nowak, E. R., Weissman, M. B., and Parkin, S. S. P. “Electrical noise in hysteretic ferromagnet-insulator-ferromagnet tunnel junctions”. In: *Applied Physics Letters* 74.4 (1999), p. 600.

[79] Nowak, E. R. et al. “Noise properties of ferromagnetic tunnel junctions”. In: *Journal of Applied Physics* 84.11 (1998), p. 6195.

[80] Okuto, Y and Crowell, CR. “Threshold energy effect on avalanche breakdown voltage in semiconductor junctions”. In: *Solid-State Electronics* 18.2 (1975), p. 161.

[81] Ono, Keiji, Shimada, Hiroshi, and Ootuka, Youiti. “Enhanced magnetic valve effect and magneto-Coulomb oscillations in ferromagnetic single electron transistor”. In: *Journal of the physical society of Japan* 66.5 (1997), p. 1261.

[82] Ono, Keiji et al. “Magnetoresistance of Ni/NiO/Co small tunnel junctions in Coulomb blockade regime”. In: *Journal of the physical society of Japan* 65.11 (1996), p. 3449.

[83] Pathria, R. K. *Statistical mechanics, by R. K. Pathria*. International series of monographs in natural philosophy, ; v. 45. Oxford, New York: Pergamon Press, 1972. ISBN: 0080167470.

[84] Pettersson, J. et al. “Extending the high-frequency limit of a single-electron transistor by on-chip impedance transformation”. In: *Physical Review B* 53.20 (1996), p. 13272.

[85] Pierret, Robert F and Neudeck, Gerold W. *Advanced semiconductor fundamentals*. Vol. 6. Addison-Wesley Reading, MA, 1987.

[86] Pierret, Robert F and Neudeck, Gerold W. *Semiconductor fundamentals*. Addison-Wesley Reading, 1988. ISBN: 0201122952.

[87] Pospieszalski, M. W. “Extremely low-noise amplification with cryogenic FETs and HFETs: 1970-2004”. In: *IEEE Microwave Magazine* 6.3 (2005), p. 62.

[88] Ralph, D. C. and Stiles, M. D. “Spin transfer torques”. In: *Journal of Magnetism and Magnetic Materials* 320.7 (2008), p. 1190.

[89] Reidy, SG, Cheng, L, and Bailey, WE. “Dopants for independent control of precessional frequency and damping in Ni 81 Fe 19 (50 nm) thin films”. In: *Applied Physics Letters* 82.8 (2003), p. 1254.

[90] Richey, David M et al. “Evidence for non-equilibrium base transport in Si and SiGe bipolar transistors at cryogenic temperatures”. In: *Solid-State Electronics* 39.6 (1996), p. 785.

[91] Rogovin, D. and Scalapino, D. J. “Fluctuation Phenomena in Tunnel-Junctions”. In: *Annals of Physics* 86.1 (1974), p. 1.

[92] Saito, Yoshiaki et al. “Spin-dependent tunneling in double tunnel junctions with a discontinuous intermediate layer”. In: *IEEE transactions on magnetics* 35.5 (1999), p. 2904.

[93] Sangregorio, C. et al. “Quantum tunneling of the magnetization in an iron cluster nanomagnet”. In: *Physical Review Letters* 78.24 (1997), p. 4645.

[94] Sapoval, B., Hermann, C., and King, A.R. *Physics of Semiconductors*. Springer-Verlag, 1995. ISBN: 9780387940243.

[95] Schelp, LF et al. “Spin-dependent tunneling with Coulomb blockade”. In: *Physical Review B* 56.10 (1997), R5747.

[96] Sheng, L, Xing, DY, and Sheng, DN. “Theory of the zero-bias anomaly in magnetic tunnel junctions: Inelastic tunneling via impurities”. In: *Physical Review B* 70.9 (2004), p. 094416.

[97] Sheng, L et al. “Nonlinear transport in tunnel magnetoresistance systems”. In: *Physical Review B* 59.1 (1999), p. 480.

[98] Sierra, J. F. et al. “Temperature dependent dynamic and static magnetic response in magnetic tunnel junctions with Permalloy layers”. In: *Applied Physics Letters* 93.17 (2008), p. 172510.

[99] Sierra, J. F. et al. “Interface and Temperature Dependent Magnetic Properties in Permalloy Thin Films and Tunnel Junction Structures”. In: *Journal of Nanoscience and Nanotechnology* 11.9 (2011), p. 7653.

[100] Simon, Steven H. *The Oxford solid state basics*. OUP Oxford, 2013. ISBN: 0191502103.

[101] Slonczewski, J. C. “Conductance and Exchange Coupling of 2 Ferromagnets Separated by a Tunneling Barrier”. In: *Physical Review B* 39.10 (1989), p. 6995.

[102] Snoke, D. *Solid State Physics: Essential Concepts*. Cambridge University Press, 2020. ISBN: 9781107191983.

[103] Stoner, E. C. and Wohlfarth, E. P. “A Mechanism of Magnetic Hysteresis in Heterogeneous Alloys”. In: *Philosophical Transactions of the Royal Society of London Series a-Mathematical and Physical Sciences* 240.826 (1948), p. 599.

[104] Sun, H, Yu, KW, and Li, ZY. “Magnetoresistance through grain boundaries in a resonant-tunneling mechanism”. In: *Physical Review B* 68.5 (2003), p. 054413.

[105] Takahashi, S and Maekawa, S. “Effect of Coulomb blockade on magnetoresistance in ferromagnetic tunnel junctions”. In: *Physical Review Letters* 80.8 (1998), p. 1758.

[106] Thomas, L. et al. “Macroscopic quantum tunnelling of magnetization in a single crystal of nanomagnets”. In: *Nature* 383.6596 (1996), p. 145.

[107] Tondra, M. et al. “Picotesla field sensor design using spin-dependent tunneling devices”. In: *Journal of Applied Physics* 83.11 (1998), p. 6688.

[108] Tracy, L. A. et al. “Single shot spin readout using a cryogenic high-electron-mobility transistor amplifier at sub-Kelvin temperatures”. In: *Applied Physics Letters* 108.6 (2016), p. 063101.

[109] Tran, TB et al. “Multiple cotunneling in large quantum dot arrays”. In: *Physical review letters* 95.7 (2005), p. 076806.

[110] Tsymbal, E. Y., Mryasov, O. N., and LeClair, P. R. “Spin-dependent tunnelling in magnetic tunnel junctions”. In: *Journal of Physics-Condensed Matter* 15.4 (2003), R109.

[111] Verstraete, F., Wolf, M. M., and Cirac, J. I. “Quantum computation and quantum-state engineering driven by dissipation”. In: *Nature Physics* 5.9 (2009), p. 633.

[112] Vink, I. T. et al. “Cryogenic amplifier for fast real-time detection of single-electron tunneling”. In: *Applied Physics Letters* 91.12 (2007), p. 123512.

[113] Visscher, E. H. et al. “Broadband single-electron tunneling transistor”. In: *Applied Physics Letters* 68.14 (1996), p. 2014.

[114] Wang, XH and Brataas, Arne. “Large magnetoresistance ratio in ferromagnetic single-electron transistors in the strong tunneling regime”. In: *Physical Review Letters* 83.24 (1999), p. 5138.

[115] Weinreb, S., Bardin, J. C., and Mani, H. “Design of cryogenic SiGe low-noise amplifiers”. In: *IEEE Transactions on Microwave Theory and Techniques* 55.11 (2007), p. 2306.

[116] Wernsdorfer, W. “Classical and quantum magnetization reversal studied in nanometer-sized particles and clusters”. In: *Advances in Chemical Physics, Vol 118* 118 (2001), p. 99.

[117] Wernsdorfer, W. et al. “Experimental evidence of the Neel-Brown model of magnetization reversal”. In: *Physical Review Letters* 78.9 (1997), p. 1791.

[118] Weymann, Ireneusz et al. “Tunnel magnetoresistance of quantum dots coupled to ferromagnetic leads in the sequential and cotunneling regimes”. In: *Physical Review B* 72.11 (2005), p. 115334.

[119] William, Shockley. *Circuit element utilizing semiconductive material*. Generic. 1951.

[120] Wolf, G. et al. “Time resolved transport studies of magnetization reversal in orthogonal spin transfer magnetic tunnel junction devices”. In: *Spintronics VII* 9167 (2014).

[121] Worledge, Daniel C. “Theory of spin torque switching current for the double magnetic tunnel junction”. In: *IEEE Magnetics Letters* 8 (2017), p. 1.

[122] Worledge, DC et al. “Spin torque switching of perpendicular Ta CoFeB MgO-based magnetic tunnel junctions”. In: *Applied Physics Letters* 98.2 (2011), p. 022501.

[123] Xiao, Q. F. et al. “Dynamics of ultrafast magnetization reversal in submicron elliptical Permalloy thin film elements”. In: *Physical Review B* 73.10 (2006), p. 104425.

[124] Yang, Hyunsoo, Yang, See-Hun, and Parkin, Stuart SP. “Crossover from Kondo-assisted suppression to co-tunneling enhancement of tunneling magnetoresistance via ferromagnetic nanodots in MgO tunnel barriers”. In: *Nano letters* 8.1 (2008), p. 340.

[125] Yang, S. Q. and Erskine, J. L. “Domain wall dynamics and Barkhausen jumps in thin-film permalloy microstructures”. In: *Physical Review B* 72.6 (2005), p. 064433.

[126] Yaoi, T, Ishio, S, and Miyazaki, T. “Dependence of magnetoresistance on temperature and applied voltage in a 82Ni-Fe/Al-Al2O3/Co tunneling junction”. In: *Journal of Magnetism and Magnetic Materials* 126.1-3 (1993), p. 430.

[127] Ying, H. B. et al. “Operation of SiGe HBTs Down to 70 mK”. In: *IEEE Electron Device Letters* 38.1 (2017), p. 12.

[128] Ying, H. B. et al. “Collector Transport in SiGe HBTs Operating at Cryogenic Temperatures”. In: *IEEE Transactions on Electron Devices* 65.9 (2018), p. 3697.

[129] Zhang, Shufeng et al. “Quenching of magnetoresistance by hot electrons in magnetic tunnel junctions”. In: *Physical Review Letters* 79.19 (1997), p. 3744.

VITA

Jason Dark was born in Beaumont, Texas on October 18, 1991. He was the youngest of six children with a pastor for a father and a stay-at-home-mom for a mother. His early life was filled with an amazement for electronics and how the "magic" inside of them worked. He also enjoyed running and wrestling as well as playing piano and gardening. Jason began attending Lamar University in the fall of 2009 studying Electrical Engineering. After taking Physics II, he was offered a scholarship to study physics as well. In October 2011, he ran into his middle school sweet heart, Danielle Carr, and they were married a year later. In May 2015, Jason received a B.S. in Electrical Engineering with a minor in Mathematics and a B.S. in Physics from Lamar University. From there, after receiving approval from his wife, he denied offers to work as an Electrical Engineer and moved to Georgia to study physics at the Georgia Institute of Technology. After a hard first year he received a M.S. in Physics, and, although he contemplated leaving early, he ultimately decided to continue in hopes to learn more about the mysteries of the world around him.